

Design and development of protein-polymer assemblies to engineer artificial organelles

Inauguraldissertation

zur Erlangung der Würde eines Doktors der Philosophie
vorgelegt der
Philosophisch-Naturwissenschaftlichen Fakultät
der Universität Basel

von

Pascal Tanner

aus Werthenstein, Luzern

Basel, 2013



Genehmigt von der Philosophisch-Naturwissenschaftlichen Fakultät
auf Antrag von

Prof. Dr. Cornelia Palivan (Universität Basel),

Prof. Dr. Wolfgang Meier (Universität Basel)

und

Prof. Dr. Marcus Textor (ETH Zürich)

Basel, den 17.09.2013

Prof. Dr. Jörg Schibler
(Dekan)

Abstract

Molecular engineering by means of the development of artificial organelles that can be implanted in cells to treat pathological conditions or to support the design of artificial cells has been regarded as a major goal in medical research. In order to achieve this goal, active compounds, such as enzymes, proteins and enzyme-mimics were encapsulated or entrapped in polymer compartments to create highly active hybrid nanoreactors. However, probably due to the early stage of research, only few of these nanoreactors were active in cells, and none was proven to mimic a specific natural organelle. In the present thesis, the engineering of polymeric vesicles for the development of artificial organelles mimicking natural peroxisomes is accomplished. In addition, a detailed study of the permeabilisation of polymeric vesicle membranes by incorporation of ion-channels is elaborated. The detailed study of metal-functionalised polymeric vesicle membranes for targeting approaches – an important factor for site specific action of e. g. artificial organelles – gives a further key aspect. These three parts of fundamental research play a key role in further development of advanced nanoreactors to be used as specific artificial organelles. In the first study, we designed systems that contained two different highly active antioxidant enzymes, which worked in tandem in polymer nanovesicles. The membrane of the nanovesicles was specifically permeabilised by the incorporation of natural channel proteins and the functional nanoreactor was optimised with regard to properties and function of natural peroxisomes. These non-toxic artificial peroxisomes combat oxidative stress in cells after cell-uptake, which prolong cell life-time and which can be regarded as the first instance of treatment of various pathologies (e.g. arthritis, Parkinson's, cancer, AIDS) effectively controlled by conditions of oxidative stress. The second study proves the successful incorporation of small ion-channels in

the vesicle membrane. These ion-channels are specifically permeable for monovalent cations, for example to design a pH-sensitive artificial organelle, where the active compound can be switched on/off respectively, depending on the conditions of the environment. The third project focussed on the decoration of metal-functionalised polymersomes with a small model peptide, a His₆-tag, in order to characterise the change of the metal coordination site upon binding of the model peptide. This provided important information about the binding behaviour of ligands in processes of molecular recognition, a key principle in nature. Understanding of specific and efficient binding will allow to further target the polymersomes to specific locations to either release their content, such as drugs, or to act as an artificial organelle.

Table of content

1. INTRODUCTION	1
1.1. CONCEPT OF MOLECULAR ENGINEERING.....	3
1.2. BUILDING BLOCKS FOR MOLECULAR ENGINEERING.....	4
1.2.1 <i>Bio-related properties of the amphiphilic di- and tri-block copolymers used in this thesis.....</i>	6
1.3. AMPHIPHILIC BLOCK COPOLYMER SUPERSTRUCTURES	7
1.3.1. <i>Principle of self-assembly</i>	9
1.3.2. <i>Polymeric vesicles (polymersomes)</i>	10
1.3.3. <i>Polymersome preparation methods.....</i>	11
1.3.4. <i>Characterisation methods of polymersomes</i>	12
1.4. CONCEPT OF NANOREACTORS BASED ON AMPHIPHILIC BLOCK COPOLYMERS ...	14
1.4.1. <i>Requirements for nanoreactors used in medical applications.....</i>	16
1.4.2. <i>Active compounds supporting nanoreactor functionality.....</i>	18
1.4.3. <i>Incorporation of membrane proteins and ion-channels in amphiphilic block copolymer polymersome membranes.....</i>	19
1.4.4. <i>Engineering artificial organelles as cell implants based on nanoreactors.....</i>	21
1.5. CONCEPT OF NANOCARRIERS FOR DRUG/PROTEIN DELIVERY BASED ON AMPHIPHILIC BLOCK COPOLYMERS.....	22
1.6. RELEVANCE OF REACTIVE OXYGEN SPECIES (ROS) IN OXIDATIVE STRESS	23
1.6.1. <i>Natural defence mechanism.....</i>	25
1.6.2. <i>Antioxidant therapy.....</i>	27
1.7. CONCEPT OF MOLECULAR RECOGNITION.....	28
1.7.1. <i>Molecular recognition strategies in nature</i>	29
1.7.2. <i>Targeting strategies.....</i>	30
1.7.3. <i>Metal-chelation: NTA and trisNTA.....</i>	30
1.7.3. <i>His-tags and His-tagged molecules.....</i>	32
2. COMBAT SUPEROXIDE ANION RADICALS BY ANTIOXIDANT NANOREACTORS	35
2.1. MOTIVATION AND CONCEPT	36
2.2. DESIGN OF AN ENZYMATIC CASCADE REACTION TO FIGHT OXIDATIVE STRESS..	38
2.3. DESIGN AND CHARACTERISATION OF ANTIOXIDANT NANOREACTORS.....	39
2.3.1. <i>Optimised encapsulation of individual enzymes in polymersomes</i>	41
2.3.2. <i>Activity assay of individual enzyme species in solution and in polymersomes.....</i>	48
2.3.3. <i>Optimised co-encapsulation of SOD and LPO in polymersomes.....</i>	52
2.3.4. <i>Multi-enzyme kinetics in a solution that simulates polymersome conditions.....</i>	55

2.3.5. <i>Multi-enzyme kinetics in situ inside polymersomes</i>	56
2.4. COMBATING SUPEROXIDE ANION RADICALS IN CELLS BY ARTIFICIAL PEROXISOMES	58
2.4.1. <i>Integration of artificial peroxisomes in cells</i>	60
2.5. CONCLUSION	69
3. DESIGN OF PH-TRIGGERED NANOREACTORS	71
3.1. MOTIVATION AND CONCEPT.....	72
3.2. EVIDENCE OF FUNCTIONAL ION-CHANNEL INCORPORATION IN LIPOSOMES.....	72
3.3. EVIDENCE OF FUNCTIONAL ION-CHANNEL INCORPORATION IN POLYMERSOMES	74
3.3.1. <i>Ion-channel formation (H^+ kinetics) as a function of gramicidin concentration in polymersome membranes</i>	78
3.4. PH-TRIGGERED NANOREACTORS.....	79
3.5. CONCLUSION	82
4. METAL-FUNCTIONALISED POLYMERSOMES FOR MOLECULAR RECOGNITION	83
4.1. MOTIVATION AND CONCEPT.....	83
4.2. FORMATION OF CU(II)-TRISNTA FUNCTIONALISED POLYMERSOMES.....	86
4.3. HIS ₆ -TAGS BINDING TO CU ^{II} -TRISNTA POLYMERSOMES	88
4.4. STRUCTURE OF THE COORDINATION SPHERE OF CU ^{II} IN HIS ₆ -TAG-CU ^{II} -TRISNTA POLYMERSOMES IN COMPARISON TO MODEL SYSTEMS.....	94
4.5. CONCLUSION	106
5. OVERALL CONCLUSION	109
6. EXPERIMENTAL SECTION	111
7. APPENDIX	129
8. REFERENCES	135
9. ACKNOWLEDGEMENTS	151
10. ABBREVIATIONS	153
11. CURRICULUM VITAE	157

1. Introduction

The design of new, functional and smart materials or assemblies is mainly driven to understand biological systems in more detail and to mimic biological structures and functions. There is a high need to obtain a profound knowledge of the working principle of biological systems in order to repair many diseases on molecular basis. Furthermore, the understanding of the complexity, specificity and accuracy of biologic pathways forms the basis of technological progress. Hence, it is a key challenge in life- and nanosciences to fuse biomolecules, such as enzymes or proteins, with synthetic materials, for example block copolymers, in order to create new, complex bio-synthetic nanodevices. The combination of the specificity and efficiency of biological molecules with the robustness and the possibility of tailoring synthetic materials allows the design of efficient systems in terms of activity, sensitivity and responsiveness.^{1,2} In addition, this strategy allows protecting sensitive compounds, for example enzymes, proteins, or nucleic acids, while providing optimal working conditions – the same principle as in the compartmentalisation strategy in nature. Successful protection was put into practice in recent years by shielding various biological compounds in nanometre-sized supramolecular assemblies. The purpose of shielding was already commercialized by using liposomes, which are bio-adapted, lipid-based supramolecular assemblies. However, limitations in the use of liposomes such as increased, intrinsic mechanical instability and low blood circulation life-time could only be partially solved through their combination with polymers such as polyethylene glycol (PEG), which has shown to have “stealth” behaviour (by means of no association with non-targeted serum and tissue proteins thus being able to evade the immune system).³

Consequentially, polymer supramolecular structures in the form of particles, micelles, vesicles and films are of particular interest, because they can adapt their properties to support combination with biological molecules while preserving material properties such as stability and mechanical robustness.^{4,5} Polymer supramolecular assemblies exhibit morphologies and properties, which can be adapted by choosing from a variety of highly diverse block copolymers. By triggering the block length of each block unit of the block copolymer, the entire molecular architecture is provided. In addition, properties such as charge, flexibility or stimuli-responsiveness can be tuned for further system integration.⁶ In conclusion, this outstanding adaptability makes these assemblies very versatile for a wider range of applications.^{7,8}

Elegant combinations of nanometre-sized, supramolecular assemblies that protect active compounds and support their *in situ* activity are polymer nanoreactors.^{9,10} Nanoreactors based on polymer vesicles encapsulating active molecules and with a membrane rendered permeable for small molecules provide fully active compounds in biologically relevant conditions inside the carrier over long time. This approach eliminates the drawbacks related to conventional drug carriers, where active compounds may act only after their release from the carrier or are released into a different biological compartment, other than desired.¹¹ When nanoreactors are used *in vitro*, sensitivity and overall activity are essential properties to be coped with, while for *in vivo* applications (therapeutics or theranostics) more complex requirements are imposed in terms of nanoreactor-assemblies properties, *in situ* functionality, and biodistribution.

Our aim here was to engineer artificial organelles focussing on three aspects: i.) design and development of a functional cascade reaction

inside polymersomes ii.) engineering triggerable nanoreactors and iii.) studying a specific molecular recognition process in detail.

i.) In a bio-inspired approach, the nanoreactor design was used to mimic a specific artificial organelle by the combination of two different antioxidant enzymes, superoxide dismutase together with lactoperoxidase or catalase. Implementation of the cascade reaction into the polymersomes enabled the use of the SOD/LPO co-encapsulated as artificial peroxisomes inside cells to repair the condition of oxidative stress.

ii.) Another approach of nanoreactor design, focussing on pH-triggered nanoreactors, was realised by incorporation of an ion-channel, gramicidin, in the membrane of pH-sensitive acid phosphatase-encapsulated polymersomes. Feasibility of pH-stimulation of the enzymes in vesicles was proven.

iii.) We used molecular recognition interactions and metal-functionalised block copolymers in order to form vesicles with specific metal points at the outer vesicle surface. Binding studies of small ligands and detailed investigation of the metal-centre coordination spheres before and after binding gave information about optimal binding conditions.

1.1. Concept of molecular engineering

Controlling the structure of materials/compounds at molecular dimensions opens the possibility to produce nanosystems or nanofactories, which do not occur in nature having for instance new functionalities or are mimics of biological systems. In general, two important strategies in molecular engineering can be followed as bottom up approaches in the design of nanofactories. One involves highly developed technologies such as a scanning tunnelling microscopy, which

enables the control of individual molecules and allows arranging them in a functional way in order to create an active nanosystem. The other strategy makes use of the self-assembly principle naturally evolved in biological systems to build more complex systems. The self-assembly principle has the advantage that molecules assemble into structures based on molecular interactions such as hydrogen bonds, Van der Waals or electrostatic interactions without the need of expensive techniques and time-consuming procedures. Complex templates can be engineered by using molecules, for example, lipids or amphiphilic block copolymers. In order to design functional nanofactories, active molecules such as enzymes, proteins or enzyme-mimics need to be combined with the self-assembled structure. Preservation of the functionality of the active molecules during this process is a key step to engineer functional nanodevices such as nanoreactors. This requires the working principle and optimised conditions of the active molecule to be studied in detail. After proof of concept, application of the engineered nanofactories either in the technological or biomedical domain has to fulfil further requirements, addressing for example maximising efficiency in sensor systems or increased efficacy and low immunotoxicity in therapeutic applications.

1.2. Building blocks for molecular engineering

Different building blocks to engineer supramolecular assemblies as template structures for medical applications can be used: Biopolymers, synthetic polymers or combinations of bio- and synthetic polymers. Biopolymers include lipids, polysaccharides, polypeptides and polynucleotides. Their inherent biocompatibility and biodegradability in

human bodies and cheap production qualify them for technological applications such as carrier systems.¹²

The category of synthetic polymers can be divided into homopolymers, polyelectrolytes and block copolymers.^{10,13-15} Homopolymers are built from covalently attached identical repeating units in linear or branched form. Polyelectrolytes have repeating polymer units with charged functional groups.

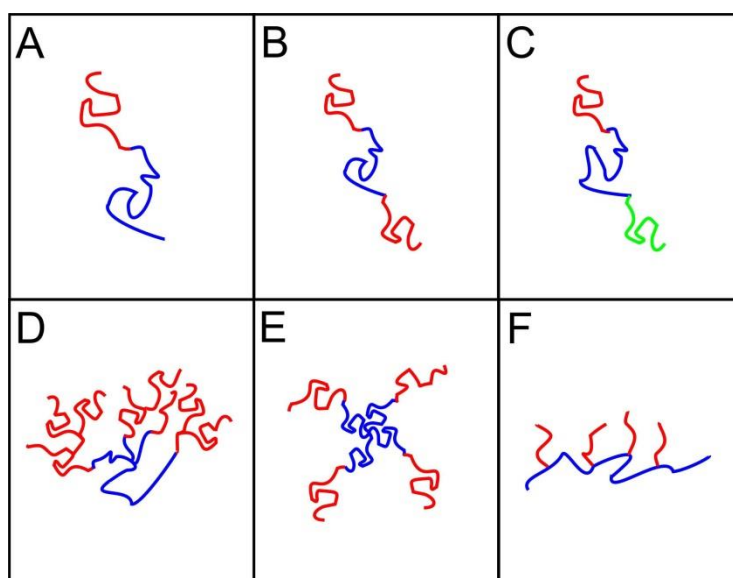


Fig. 1 Amphiphilic block copolymer architectures: A) AB-diblock; B) ABA-triblock; C) ABC-triblock; D) dendrimer; E) star-shape; F) linear grafted shape.

This thesis is mainly based on amphiphilic block copolymers. Block copolymers belong to a special class of synthetic macromolecules consisting of at least two different groups of repeating structural units called homopolymers. The different homopolymer units are either covalently linked or are linked by a junction block, which is an intermediate and non-repeating spacer.¹⁶ Amphiphilic block copolymers are composed of at least two subunits, where one homopolymer subunit

has hydrophilic (water soluble) properties while the other has hydrophobic (water insoluble) character. The homopolymer block is abbreviated for clarity as A, B, C etc., and their order in the block copolymer is directly used for its classification. According to this classification, block copolymer architectures such as AB – diblock, ABA – triblock, ABC – triblock, dendrimer shape, star-shape and grafted are shown in Fig. 1. These architectures can have either linear, cyclic, multi-arm star, comb, hyper-branched or dendritic shapes.¹⁷

1.2.1 Bio-related properties of the amphiphilic di- and tri-block copolymers used in this thesis

In this work, three different kinds of amphiphilic block copolymer were employed: A triblock copolymer consisting of an amphiphilic poly(2-methyloxazoline)-*b*-poly-(dimethylsiloxane)-*b*-poly(2-methyloxazoline) (PMOXA-PDMS-PMOXA), a diblock copolymer based on poly(2-methyloxazoline)-*b*-poly-(dimethylsiloxane) (PMOXA-PDMS) and a diblock copolymer made of poly(butadiene)-*b*-poly(ethylene oxide) (PB-*b*-PEO). The biologically relevant properties of the individual homopolymers are summarised here:

PMOXA: PMOXA is often used as the hydrophilic block in either AB diblock or ABA triblock copolymers as building block in supramolecular assemblies for biological applications.^{2,11} Recent studies on the biodistribution and excretion of well-defined radiolabelled PMOXA in mice demonstrated no accumulation in tissue and rapid clearance from the bloodstream, thus apporion a good biocompatibility of biodegradability of PMOXA.¹⁸ Cell-viability measurements of block copolymers containing PMOXA indicated low toxicity, which makes it an ideal candidate to build functional artificial organelles.

PDMS: Silicones, and in this special case, PDMS are widely used in medical applications, such as breast implants.¹⁹ As it is non-irritating and non-sensitising, it shows good biocompatibility. In block copolymers, it is widely used as the hydrophobic block. Also block copolymers containing PDMS were widely used to build supramolecular assemblies such as nanovesicles for diagnostic or therapeutic applications.

PEO: PEO is widely applied in drug delivery applications. It has a good biocompatibility, hydrophilicity, versatility and stealth behaviour.¹⁸ Studies have demonstrated a protein repellent character.²⁰ This linear polymer can be easily modified for example by covalent binding of a metal-chelating agent for targeting purpose.²¹

PB: PB has vinyl groups attached to the backbone and is soluble only in organic solvents such as acetone, but insoluble in water.²² PB is often used as the hydrophobic block in amphiphilic block copolymers.²¹⁻²³ The monomer 1, 3-butadiene is highly toxic. It is expected to be involved in cardiovascular disease, leukaemia and other cancer as described by the national pollutant inventory. Therefore its use in bio-related applications is not recommended. Because PB was used in this thesis as a part of the diblock copolymer PB-*b*-PEO, which formed nanovesicles, in order to study the geometry changes of the metal-functionalised part in the process of molecular recognition, the potential toxicity of this block copolymer was no matter of interest.

1.3. Amphiphilic block copolymer superstructures

Amphiphilic molecules, such as lipids, surfactants or amphiphilic block copolymers, possess the ability to form self-assembled superstructures in aqueous media. The hydrophilic part and the hydrophobic part thereby

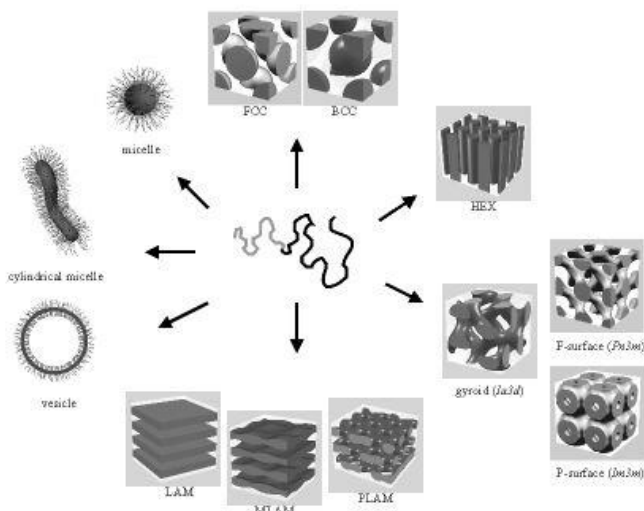


Fig. 2 Self-assembled structures based on block copolymers and surfactants: spherical micelles, cylindrical micelles, vesicles, fcc- and bcc-packed spheres (FCC, BCC), hexagonally packed cylinders (HEX), various minimal surfaces (gyroid, F surface, P surface), simple lamellae (LAM), as well as modulated and perforated lamellae (MLAM, PLAM). Reprinted with permission from Ref. 24 Copyright 2002 WILEY-VCH Verlag GmbH & Co. KGaA.

describe the overall amphiphilicity of the molecule. The two blocks were covalently linked in order to avoid macrophase separation,²⁴ which occurs for example by water and oil emulsions. At defined conditions, molecular ordered superstructures were formed via self-assembly depending on the insoluble to soluble ratio, the molecular weight and the concentration.^{25,26} In this case, different morphologies such as micelles, vesicles, tubes, lamellar structures, etc. are obtained (Fig. 2). The type of morphology can be also modulated by different solvents, where only one block of the amphiphile is soluble.²⁷

Amphiphilic block copolymer superstructures are well suited to mimic biological structures in order to engineer new functional materials for

therapeutic, diagnostic and theranostic applications due to serious advantages compared to their natural counterparts (e.g. lipids).

1.3.1. Principle of self-assembly

The self-assembly process is a fundamental principle in nature to organise molecules from a disordered system to highly organised structures or patterns without the aid of external trigger factors. Well-ordered biological assemblies can be formed spontaneously by the self-assembly process. For example lipid bilayers, the matrix of cell membranes, are formed by the self-assembly of lipids. Other self-assembled structures are proteins, nucleic acids and viruses. The self-assembly process is essential for these structures to fulfil their biological function.

The self-assembly process is based on intermolecular and/or intramolecular interactions, whereas the process is mainly driven by non-covalent hydrophobic interactions. During the self-assembly process in aqueous solution, the hydrophobic parts of amphiphiles preferentially align with each other, which is favourable compared to the interaction with water leading to an increased entropy (hydrophobic effect).²⁸ In order to predict the self-assembly behaviour of amphiphilic block copolymers containing hydrocarbons, the packing parameter P describes the shape of the molecules (equation 1).²⁹

$$P = V/a_0l \quad (1)$$

V is described as the hydrophobic chain volume, l as the preferred length and a_0 the area, which is occupied by the hydrophilic head group of the amphiphile. In the case of lipid-like molecules, a $P > 0.5$ was attributed to the favoured formation of spherical and cylindrical micelles.

The situation $0.5 < P < 1$ leads to less curved bilayers. Nevertheless it is more appropriate for amphiphilic block copolymers to use the volume or weight fraction of the hydrophilic block to describe their shape.³⁰

1.3.2. Polymeric vesicles (polymersomes)

The most important representatives among the self-assembled superstructures in this thesis are polymer vesicles, known as polymersomes, which were generated by self-assembling amphiphilic copolymers in dilute aqueous solutions, in a similar way to lipids.^{26,31} These vesicles are spherical objects with closed-block-copolymer membranes in diameters ranging from 50 nm to approximately 10 μm , depending on the chemical composition, the size as well as the hydrophobic/hydrophilic ratio^{32,33} of the polymer blocks, the preparation method and the preparation conditions. These polymer vesicles are significantly more stable to lysis by classical surfactants than liposomes, while preserving low immunogenicity.^{26,34} In addition, they are highly impermeable compared to liposomes,³⁴ can be stimuli responsive and can be functionalised for targeting approaches.^{35,36} Various techniques were used to generate polymersomes such as direct dissolution of copolymers (direct dissolution method), addition of the copolymer previously dissolved in an organic solvent to aqueous media (cosolvent method), or hydration of a copolymer film (film hydration method).³¹ Depending on the intended application, polymersomes may be adapted to specific sizes for particular routes of administration. The polymer membrane is organised in the way that the hydrophilic part is exposed to the inner and outer aqueous environments³⁴ and serves to partition aqueous volumes with different compositions and concentrations, due to a selective permeability towards hydrophobic and hydrophilic molecules.²⁴ The molecular weight of the used block copolymers directly reflects

membrane thickness, which can be up to 30 nm.³⁷ The high mechanical polymersome membrane stability leads to a long-lasting retention of payloads, ideally suited for technological applications. Beside the possibility to encapsulate hydrophilic guest molecules, polymersomes can simultaneously carry hydrophobic molecules in their membrane.³⁸ Vesicular morphologies are illustrated based on AB diblock and ABA triblock copolymer (Fig. 3).

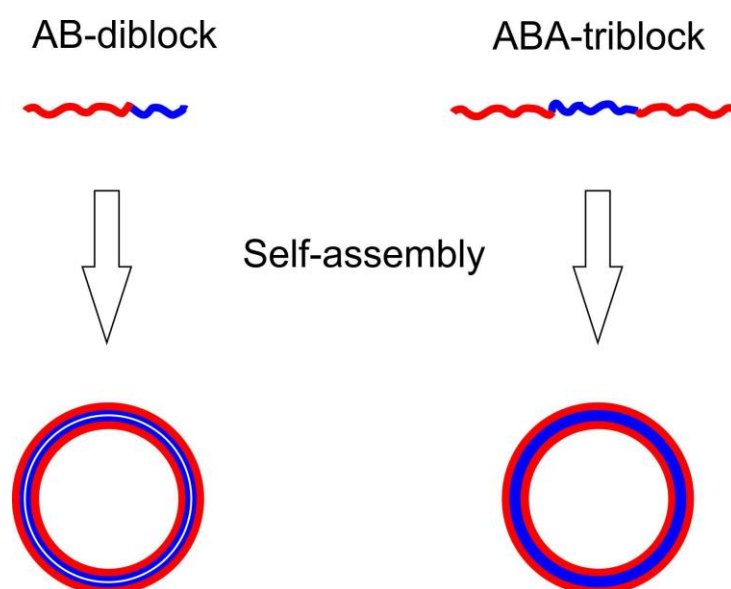


Fig. 3 Polymersome formation based on AB-diblock copolymer in comparison to ABA-triblock copolymer.

1.3.3. Polymersome preparation methods

The procedure to prepare polymersomes requires that the specificity of the building blocks, the conditions for the active compounds in case of nanoreactor (see chapter 1.4) preparation, the architecture etc. are adequate for the intended application. Especially in medical applications, when polymersomes are used in the human body, the safety issue increases considerably.

Only the relevant techniques applied in the framework of our project, the film hydration technique and the direct dissolution method will be further discussed.

The film rehydration method consists of two stages: Firstly, the amphiphiles are dissolved in an organic solvent and subsequently the solvent is evaporated to form an uniform, thin film on the surface of a glass flask.³⁹ Afterwards, the self-assembly process towards macromolecular superstructures such as vesicles is initiated by the addition of the aqueous solution, accompanied by additional forces such as stirring, vortexing or sonication. The aqueous solution may contain active compounds, which will result in their encapsulation in the aqueous cavity or their incorporation in the membrane of the supramolecular structures (e.g. vesicle membrane).

In the direct dissolution method, polymers are directly dissolved in the aqueous solution, which may contain active compounds for nanoreactor preparation, by extended agitation until the polymer is completely hydrated.²⁴

1.3.4. Characterisation methods of polymersomes

Polymersome characterisation starts with the detailed investigation of the building blocks and continues with the characterisation of the architectures with regard to their size, stability, flexibility, charge, etc. When active compounds are involved, overall nanoreactor activity needs to be determined.

Polymersome size and size distribution^{24,40} (polydispersity index), the aggregation concentration,⁴¹ morphology⁴² and change of size or shape with variation of pH, temperature or detergent addition^{43,44} can be determined by light scattering (static and dynamic light scattering) experiments. Parameters such as weight averaged molecular mass,

radius of gyration, hydrodynamic radius as well as information about particle – particle and particle – solvent interactions can be deduced.⁴²

For direct visualisation of self-assembled structures most commonly microscopy techniques, such as optical microscopy, laser-scanning microscopy, or electron microscopy are used. These techniques allow to extensively characterise structures in a broad range from a few nanometres (super resolution microscopy such as STED (Stimulated Emission Depletion) or STORM (Stochastic Optical Reconstruction Microscopy)) to a few micrometres.⁴⁵

The simplest method to visualise the assemblies under ‘physiological’ conditions is offered by optical microscopy, but the limited resolution – max resolution corresponds to the half of the used wavelength (around 200 nm) – of these devices is a disadvantage compared to electron microscopy. Therefore, only large assemblies such as giant liposomes or giant polymersomes can be observed by optical microscopy.

Electron microscopy techniques, including transmission electron microscopy (TEM), scanning electron microscopy (SEM), cryo-TEM and cryo-SEM, provide higher resolution and allow to visualise self-assembled superstructures and nanoreactors.⁴⁶⁻⁴⁸ Thickness and structure of a vesicle membrane and their phase behaviour can be observed by cryo-TEM, cryo-SEM and the freeze-fracture technique.⁴⁹

Fluorescence microscopy is established for observation of fluorescently labelled nanocompartments, which contain fluorescent dyes or fluorescent proteins. This method is used to study polymer assemblies with respect to dye encapsulation behaviour or dye binding properties,⁵⁰⁻⁵³ and to investigate cellular uptake of polymersome nanocarriers or nanoreactors. Furthermore, activity of nanoreactors after cellular uptake can be proven by visualisation of fluorescent products in real-time.

Confocal laser-scanning microscopy (CLSM) is a special kind of fluorescence microscopy, where the specimen is point-wise irradiated and its fluorescence emission is point-wise measured to create an image. The main difference is the use of a confocal aperture, the pinhole, which is adjustable and determines how fluorescence light coming from non-focused planes is detected. This allows to image small sections and to reconstruct 3D images containing different focus planes.

Fluorescence correlation spectroscopy (FCS) is used to investigate the dynamic properties of fluorescent molecules such as dyes, macromolecules and nanoparticles.⁵⁴ The experimental technique is based on monitoring fluorescence intensity fluctuations in a small observation volume – a confocal volume. A correlation analysis of the fluctuations yields information on the diffusion coefficients and times, population distributions, concentrations, etc. It is also possible to determine the size and quantify the number of encapsulated fluorescent dyes or proteins in nanocontainers.^{51,52,54} The technique is widely used for studies concerning encapsulation/entrapment/binding of fluorescent molecules in/on polymer assemblies in order to determine the sensitivity and stability of nanoreactors.^{46,51,55}

1.4. Concept of nanoreactors based on amphiphilic block copolymers

In this thesis, a nanoreactor is defined as a polymersome encapsulated with an active compound (for example enzymes, proteins, enzyme-mimics) and rendered permeable for substrates/products by the insertion of membrane proteins or ion channels in the polymersome membrane (Fig. 4).

The concept of nanoreactor originates from the compartmentalisation strategy in nature, where compartments are used to separate biological

processes. Prominent examples in cells are organelles such as the endoplasmic reticulum, the Golgi apparatus, mitochondria, peroxisomes, the nucleus, etc., where biological molecules are produced, transported, detoxified, stored or disposed of. The advantage of the compartmentalisation strategy is that different biological processes can simultaneously run without interfering each other due to portioning of biological tasks. It further allows the protection of sensitive biomolecules or provision of adapted conditions, while communication (exchange of signals) enables complex cascade reactions. Similar to cell compartments, nanoreactors are regarded as nanometre-sized reaction compartments/spaces used for chemical and biological reactions.

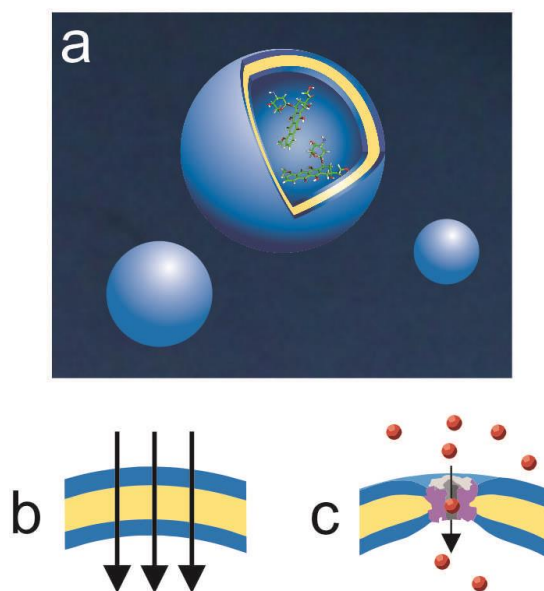


Fig. 4 a) Polymersomes containing active compounds inside their aqueous cavity. b) Polymer membrane, which is intrinsically permeable. c) A polymer membrane with an inserted channel protein. Adapted with permission from Ref. 11 Copyright 2011 American Chemical Society.

The concept of nanoreactors implies that the active compounds are kept permanently in its aqueous cavity or in its membrane. This compartmentalisation strategy has also the dual ability: the protection of the content from proteolytic attack and providing a reaction space for *in situ* activity.¹¹ Nanoreactors were used to monitor¹¹ or detoxify^{51,56} substances, to produce drugs and were applied for enzyme replacement therapy.⁵⁷

In medical applications, an increased efficacy of nanoreactors is desirable compared to unspecific drug administration, which could be realised by their site-specific action. Site-specific action can be triggered by a specific targeting, which can be put into practice by functionalisation of the nanoreactor's surface with, for example, peptides, proteins, antibodies or chelating agents to generate molecular recognition points.^{52,53,55} Based on the highly specific molecular recognition, surface-functionalised nanoreactors were able to act at specific locations.^{47,58,59} Also stimuli-responsive nanoreactors were generated, which can be predetermined on or off "on demand" by different stimuli such as physical (light, temperature, mechanical, magnetic, etc.), chemical (solvent, pH, ionic strength) and biological (receptor, enzyme) triggers.⁶⁰

1.4.1. Requirements for nanoreactors used in medical applications

In case of nanoreactor preparation, the proper combination of active compounds with the polymersome architecture is needed (in the aqueous cavity of the polymersome or in the polymersome membrane). Nanoreactor functionality depends on the activity of the active compound, which is specific and depends on the preparation method, the pH, ionic strength, temperature and traces of solvents.¹⁰ Therefore, nanoreactor preparation requires the preservation of the activity of the active compound starting with the choice of the building blocks, which are

treated with organic solvents. These solvents, even in traces, could have considerable effects on the activity of the biological compound. When using a preparation method, the use of organic solvents should be minimised or entirely organic solvent free preparation methods should be used.²⁴

Medical applications differ if nanoreactors are meant to be used inside a cell as an *in vivo* application for diagnostics or therapeutics, or as *ex vivo*, when nanoreactors are used as medical sensor for diagnostics. When a nanoreactor is used outside a body, nanoreactor performance with regard to ideal working conditions (pH, ionic strength, temperature, etc. for the encapsulated, active compound is aspired solely. On the other hand, nanoreactors applied *in vivo* have to fulfil complex requirements, which belong to the safety standards provided by the U.S Food and Drug Administration (FDA) and the European Medicines Agency (EMA). This guarantees that the *in situ* biological activity of encapsulated active molecules is ensured,^{2,61} the integrity and activity of the nanoreactor is preserved in biological conditions and that the nanoreactor and its components (nanoreactor building blocks and the active molecules) are biocompatible and biodegradable^{25,56,62} and do not accumulate in the body.

The size and morphology of a nanoreactor is crucial for its cellular interactions. In this respect, nanoreactors of around 200 nm in diameter have shown to be uptaken by cells.^{47,56} Therefore, nanoreactor preparation methods need to be aimed to this size range. Preparation methods also play an important role for preserving the biological activity of the active species. Hence, solvents, which potentially lower enzymatic activity, must be avoided.² Also the chemical constitution and properties of the nanoreactor system such as charge flexibility and density of the building blocks can influence the activity of the active compound. Stability

and integrity of the nanoreactors avoid the release of potential toxic substances in the body. Nevertheless, nanoreactor membrane permeability is desired for substrates and products. The efficacy of the nanoreactor is enhanced by nanoreactors having stealth-like characters.

1.4.2. Active compounds supporting nanoreactor functionality

Which active compounds were used for nanoreactor engineering? Most commonly, proteins, enzymes, enzyme-mimics, or photoactive dyes have been entrapped in the nanoreactor compartments.^{10,25,60}

Proteins are key molecules in cell activities. They catalyse metabolic reactions, transcribe and replicate DNA, are stimuli responsive, transport oxygen, etc. For example, haemoglobin was encapsulated in polymersomes with a dual functionality of oxygen transport and detoxification of peroxynitrite.⁶³

A special class of proteins are enzymes, which specifically and efficiently catalyse biological reactions to sustain life. They contain either ion metal groups or organic functional groups, which can accelerate metabolic reactions up to the diffusion-limit. Prominent catalytic mechanisms were transition-state binding, entropic control of reactions, acid-base catalysis, etc.

Enzyme-mimics were developed as artificial enzymes in order to understand the functionality of biological counterparts in more detail, to generate artificial enzymes with improved functionalities⁶² or to adopt functions of enzymes.⁶⁴

Also, photoactive dyes were encapsulated in nanoreactors to generate reactive oxygen species for applications in cancer therapy.⁶⁰ In this context, encapsulation is important in order to reduce toxicity of the photoactive dyes, while their efficacy can be increased due to application of a local high dosage.

1.4.3. Incorporation of membrane proteins and ion-channels in amphiphilic block copolymer polymersome membranes

The low permeability of the membrane of polymersomes towards a great variety of molecules such as substrates requires that the active compounds in the aqueous cavity of the polymersomes must be made accessible. A strategy therefore is to permeabilise the membrane either by using substrate-permeable membranes⁶⁵ or by inserting membrane proteins that serve as “gates”.⁶⁶⁻⁶⁸ Even though the dimensions of synthetic membranes (>10 nm) exceeds the dimensions of membrane proteins, functional incorporation in the membrane is feasible.

Membrane proteins, such as the aquaporin Z (AqpZ), LamB, TsX or complex 1, are specific transporters,^{66,67,69,70} while OmpF or FhuA form unspecific channels.^{68,71} The membrane proteins can tune the permeability of the membrane in a selective manner when specific transporters are inserted. In this thesis, the membrane protein OmpF and the ion-channel gramicidin were used to render the polymersome membrane permeable for substrates or trigger factors.

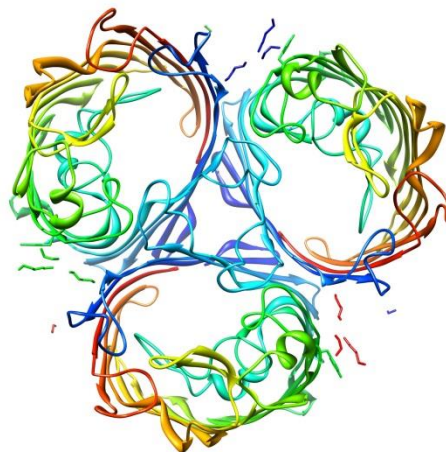


Fig. 5 Top view of OmpF. Figure generated from the protein database: <http://www.rcsb.org>.

OmpF

The outer membrane protein F (OmpF) is isolated from *E. coli* cultures in quantities of tens of mg/mL cultures⁷² and is stable in conditions of up to 70 °C in 2% sodium dodecyl sulphate.⁷³ Dissolving OmpF in ethanol, for example for membrane incorporation, has no influence on its activity or stability. OmpF (Fig. 5) allows the passage of molecules up to a molecular weight of 600 Daltons (Da).⁷⁴ It has a beta-barrel structure, as most of the channel proteins,⁷⁴ which secondary structure has increased stability compared to α -helical membrane proteins.

Functional incorporation of OmpF in PMOXA-PDMS-PMOXA copolymer membranes was realised by Meier et al.⁷⁵ As shown in Fig. 5, OmpF is composed of three identical subunits, whereby the monomers are mainly build by a 16-stranded antiparallel β -sheet barrel.⁷⁶

Gramicidin

In contrast to OmpF, which unspecifically allows the passage of molecules, gramicidin is an ion-channel, specific for monovalent cations. Gramicidin is a polypeptide antibiotic, which is produced by *Bacillus brevis*. It consists of 15 hydrophobic amino acids that are neither charged nor polar with the common following sequence: formyl-L-val-gly-L-ala-o-leu-L-ala-o-val-L-val-o-val-L-trp-o-leu-L-xxx-D-leu-L-trp-D-leu-L-trp-ethanolamine, where xxx is tryptophan in gramicidin A, phenylalanine in gramicidin B, and tyrosine in gramicidin C.⁷⁷

Consequently, gramicidin is almost insoluble in water, but is soluble in many apolar solvents, phospholipids and alcohols.

Due to its small size, gramicidin can adopt a variety of different conformations. The two main conformations were determined as a helical dimer or a double helical structure (Fig. 6).⁷⁷ The helical dimer consists of

two monomeric gramicidin helices, which are associated with each other N-terminus to N-terminus.

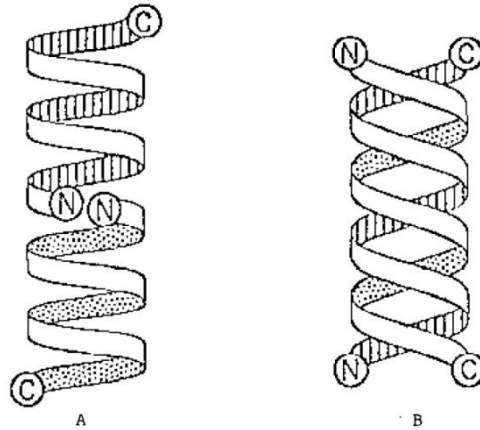


Fig. 6 Two main conformations of gramicidin pores are (A) a helical dimer (this form leads to channel formation) or (B) a double helical structure (pore formation). Reprinted with permission from Ref. 77 Copyright 1990 by Annual Reviews Inc.

The association between the two monomer- helices is stabilised by six H-bonds. The dimer formation (this conformation is around 25 Å in length) is crucial to cross a membrane (e.g. a lipid- bilayer) because one gramicidin molecule alone would be too short to span the membrane.⁷⁷ The channel, which is formed by the gramicidin helical dimer, is pervious for monovalent cations such as H⁺ and K⁺ and has a diameter of 4 Å. In nature, gramicidin serves as a defending mechanism against other microorganisms. It has the ability to incorporate into lipid membranes, rendering them permeable for ions thereby destroying the electrochemical gradient, which is necessary for ATP production.

1.4.4. Engineering artificial organelles as cell implants based on nanoreactors

Due to the inherent advantageous properties of nanoreactors, their development is highly directed towards applications inside the body. This

could be either in the blood stream or in a bio-inspired approach by mimicking cell organelles.^{2,47,61,62,78} Such an approach of developing "cell implants" has large potential in the repair of cell dysfunctions directly at the source, responsible of many disease such as Parkinson`s disease, amyotrophic lateral sclerosis (ALS), Alzheimer, cancer, etc. This new strategy will have an enormous impact on personalised medicine and in the design of artificial cells to build more complex synthetic systems. To date, only few examples of nanoreactors used as artificial organelles are known, which can be explained by the complex requirements for their design and preparation. Nevertheless, until now, the few claimed artificial organelles even do not perform a biologically relevant task. Nanoreactors must have appropriate sizes or are tagged with cell-targeting moieties for enhanced cell-uptake. In addition, the activity of entrapped/encapsulated enzymes must be maintained *in situ* and the nanoreactor must be stable in order not to break under different environmental conditions, such as low pH as present in lysosomes.

1.5. Concept of nanocarriers for drug/protein delivery based on amphiphilic block copolymers

The concept of nanocarriers based on polymersomes emerged from the desire to deliver active components such as drugs at high dosage to specific locations. This was realised by the encapsulation (in the aqueous cavity) and/or entrapment (in the membrane) of payloads (drugs,^{79,80} DNA,⁸¹ proteins,^{82,83} or RNA⁸⁴) in the compartments and its directed release.

Encapsulation efficiency plays a crucial role in the efficacy of the payloads, especially when high dosages of drugs were needed. Different attempts to increase the encapsulation efficiency, for example by complexation of the encapsulated compounds⁸⁵ or by optimisation of the

copolymer block lengths⁴⁶ were performed. In addition, it is also important that the nanocarriers can "detect" the target location for payload release. This is achieved by a targeting approach, which in combination with triggers, such as pH, temperature or light can efficiently control the release of the active components. Nevertheless it is still challenging to precisely control the release over time and it is unknown that payloads are released in the right place of action.

1.6. Relevance of reactive oxygen species (ROS) in oxidative stress

In certain pathologies, the regulation of reactive oxygen species (ROS), which include the superoxide radical anion ($O_2^{\cdot-}$), peroxynitrite ($ONOO^-$), the hydroxyl radical (OH^{\cdot}) and hydrogen peroxide (H_2O_2) is disordered. ROS are highly reactive molecules due to their unpaired electrons. They are generated during the oxygen metabolism as a by-product and play an important role in cell signalling and homeostasis.^{86,87} Oxidative stress occurs when the metabolic status of an aerobic organism is imbalanced with ROS by overwhelming the cellular antioxidant defence mechanisms to the disadvantage of the organism's antioxidant defence mechanism. Oxidative stress has been shown to contribute to aging⁸⁸ and to play a significant role in many disease including arthritis, Parkinson's disease, amyotrophic lateral sclerosis (ALS), cancer and AIDS.⁸⁹⁻⁹² There are different sources, where ROS are produced as shown in Fig. 7.

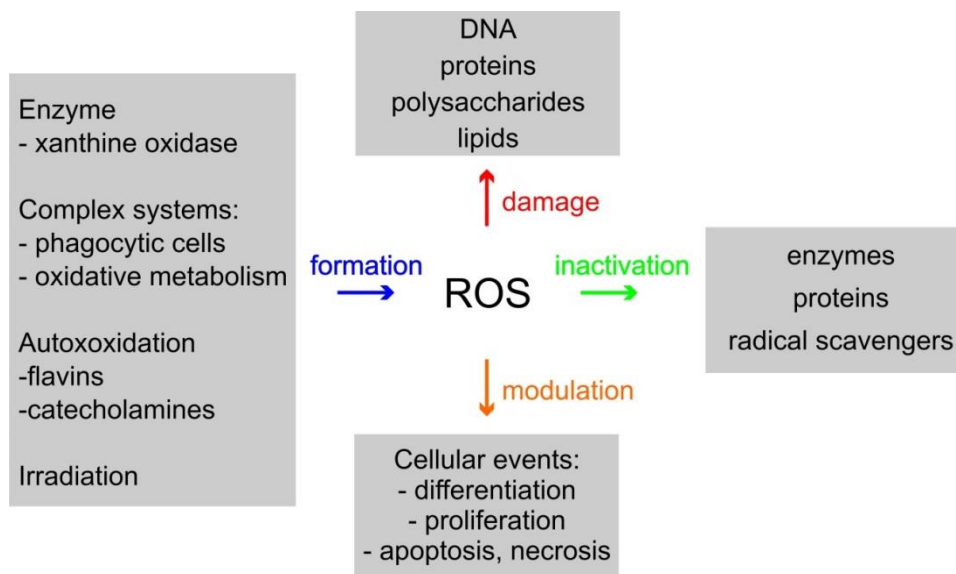


Fig. 7 Overview of the source of reactive oxygen species and its impact on biomolecules and biological processes.

Exogenous agents such as smog, ozone, pesticides, ionizing radiation, xenobiotics etc. and a variety of endogenous processes, such as the mitochondrial respiration, cytochrome P-450 detoxification reactions, xanthine oxidase oxidation, phagocytic oxidative bursts, and peroxisomal leakage can generate significant amount of ROS. This leads to damage, inactivation and modulation of biological molecules, such as proteins, carbohydrates, lipids, and nucleic acids and of cellular events due to the activity of ROS (Fig. 7).

Dramatic effect on suitable adaption of metabolic processes had to occur due to the availability of oxygen in the course of evolution. Amongst others, the development of antioxidant defence mechanisms to regulated ROS was essential for survival.

1.6.1. Natural defence mechanism

Superoxide radicals and related hydrogen peroxide are continuously produced during the mitochondrial respiratory as a result of univalent oxygen reduction by Complex I.⁹³ But also in peroxisomes, where the fatty acid α -oxidation, the β -oxidation of very long chain fatty acids, the catabolism of purines, and the biosynthesis of glycerolipids and bile acids occurs, reactive oxygen species can be formed.⁹⁴ The natural defence mechanisms are able to reduce reactive oxygen species to tolerable, non-toxic amounts due to their toxic effect at concentration above the threshold produced during the metabolism or necessary for signal transduction. Antioxidant substances are part of the defence mechanism, which are able to minimise or prevent substrate oxidation. These can be for example enzymes such as superoxide dismutase (SOD), catalase (CAT), both found in peroxisomes, peroxidases (e.g. lactoperoxidase or horseradish peroxidase), glutathione peroxidase and transferases, quinone reductases or small molecular weight substances such as glutathione, ascorbic acid, vitamin C and E, uric acid, carotenoids, etc. able to act as antioxidants.

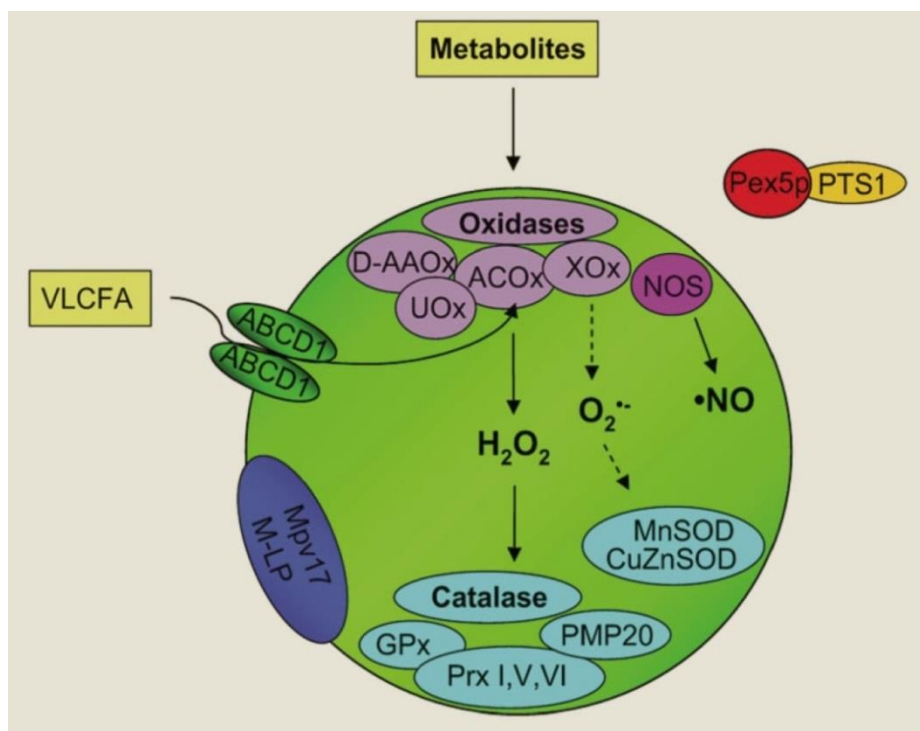
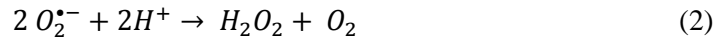


Fig. 8 Schematic overview of ROS homeostasis occurring in peroxisomes. Specific transporters (e.g. ABCD1) transport various peroxisomal metabolites such as VLCFA across the membrane and most of the peroxisomal matrix proteins are imported in a PTS1/Pex5p-dependent manner. Peroxisomal oxidases (light purple) are responsible to break down the substrates so that the hydrogen extracted from the substrate is directly transferred to O₂. Peroxisomal antioxidant enzymes (light blue) convert the generated H₂O₂ to H₂O and O₂. A by-product of the xanthine oxidase (XO) activity is O₂^{•-}, which is immediately reduced by manganese superoxide dismutase (MnSOD) and copper-zinc-superoxide dismutase (Cu/ZnSOD). Others, such as Mpv17 and M-LP (dark blue) are involved in the regulation of peroxisomal ROS metabolism, even though it is not clear if they are localized in the peroxisome. Reprinted with permission from Ref. 94. Copyright 2009 WILEY-VCH Verlag GmbH & Co. KGaA.

The importance of ROS detoxification is illustrated in the schematic overview of ROS homeostasis occurring in peroxisomes, as shown in Fig. 8.⁹⁴ It proceeds as a cascade reaction, where SOD detoxifies the O₂^{•-}

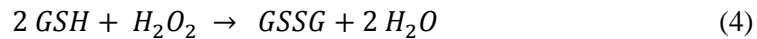
radicals to hydrogen peroxide, shown in equation 2.



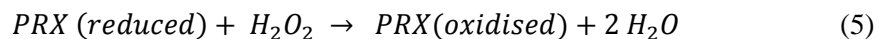
The toxic character of H_2O_2 implies its further decomposition to harmless products, water and O_2 , which is made either by CAT, glutathione peroxidase, peroxiredoxin or PMP20, which also belongs to the peroxiredoxin family.⁹⁵ CAT detoxifies H_2O_2 in a catalactic reaction (equation 3).



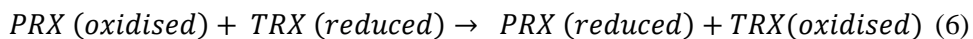
The mechanism, where glutathione peroxidase is involved, removes H_2O_2 by the oxidation of glutathione (GSH) to its oxidised form, glutathione disulphide (GSSG) (equation 4).



The peroxiredoxin (PRX) system uses thioredoxin (TRX) to detoxify H_2O_2 . The following reaction mechanism is proposed: (equation 5)



Due to the inactivity of PRX (oxidised), it needs to be restored to its reduced form by TRX, shown in equation 6.



TRX is a polypeptide especially occurring in the endoplasmic reticulum and in mitochondria. It contains a dithiol-disulfide active site. Its reduced state is obtained by flavoenzyme thioredoxin reductase.

1.6.2. Antioxidant therapy

The aim of the antioxidant therapy is to counteract the functional failure or the overcharge of natural antioxidant mechanisms by providing

antioxidants. These are able to reduce the harmful effects of ROS and thus prevent or cure oxidative stress and related diseases. Early antioxidant therapies made use of antioxidants known from the natural defence mechanism, such as SOD or CAT.⁹⁶ But also vitamins, such as vitamin A, vitamin C, or vitamin E were used to reduce the amount of ROS.⁹⁷ Nevertheless, the short half-life in blood plasma and difficulty for efficient cellular uptake of antioxidant substances lower the efficacy of an antioxidant therapy. For example it is known that SOD and CAT were inadequately delivered to targeted cells.^{98,99} A strategy to increase uptake behaviour was for example by conjugation of antioxidant enzymes with antibodies to improve their biocompatibility.^{99,100} The risk is that conjugation of enzymes with other molecules can dramatically lower the activity of the enzymes.¹⁰¹

Nevertheless, both the use of antioxidant enzymes, as well as the use of vitamins in order to efficiently treat conditions of oxidative *in vivo* did not yield convincing benefits yet.

1.7. Concept of molecular recognition

Molecular recognition allows specific biological interactions by non-covalent bonds such as hydrogen bonds, hydrophobic interactions, metal coordination etc. and supports instant response in different processes. Molecular recognition is distinguished between static molecular recognition and dynamic recognition. Static molecular recognition can be described as a key-lock system (Fig. 9A), where the key exactly fits into the lock. Dynamic molecular recognition implies on the contrary that a binding of a first guest molecule to the host allows a second molecule via a conformation change to fit (induced fit) (Fig. 9B). Hence, in a positive allosteric system, the binding of the first guest molecules increases the

binding affinity towards the second guest, while in a negative allosteric system, the first guest molecule decreases the binding affinity towards the second guest.

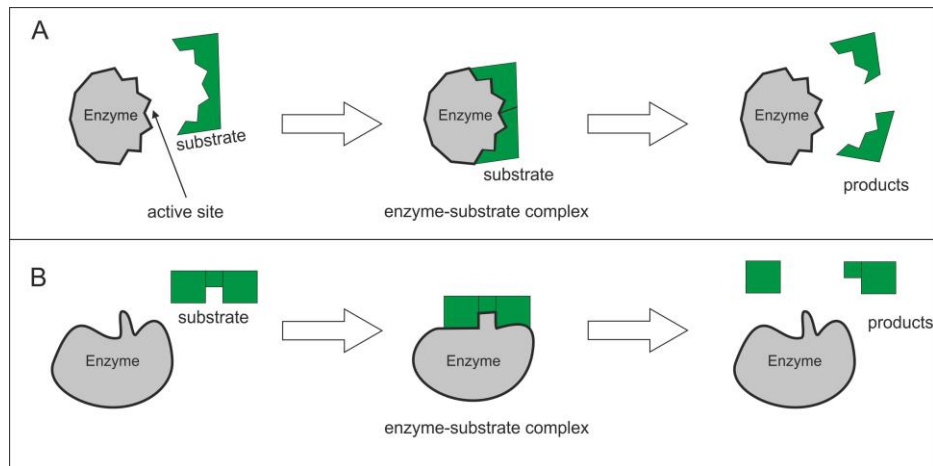


Fig. 9 Different models of substrate binding to enzymes: A) In the lock-key model, the correctly sized and shaped substrate binds to the active site of an enzyme in order to undergo an enzymatic reaction. B) In the induced fit model, the substrate determines the correct shape of the active site of the enzyme, in order to process the substrate to the product.

Technical realisation of the molecular recognition concept resulted in the principle of key-lock systems or the use of affinity tags and is widely applied in the purification^{102,103} and immobilisation^{20,23,104,105} of biomolecules, protein labelling,^{106,107} targeting approaches,¹⁰⁸ etc.

1.7.1. Molecular recognition strategies in nature

Molecular recognition in biological systems helps molecules to self-assemble, organise, recognise or communicate and to achieve biological function. Natural recognition models are for example the antigen-antibody,^{109,110} receptor-ligand systems (the nicotinic acetylcholine receptor or the folate receptor),¹¹¹ DNA-protein assemblies,¹¹² or RNA-ribosomes.

1.7.2. Targeting strategies

In order to specifically target nanocarriers or nanoreactors, the natural principle of molecular recognition, which allows identification of patterns to be recognised by each other, can be applied to synthetic systems. It is achieved by functionalisation of the polymersome surface to build specific recognition points, which is presented in the following section.

Metal-functionalised polymer membranes

Functionalisation of amphiphilic diblock copolymers with metal-based recognition sites that can self-assemble to polymersomes allow production of metal-functionalised polymer membranes. In these supramolecular assemblies, the free coordination points of the metal centre interacts with biomolecules by replacing the solvent molecules and rearranging its geometry.⁵⁵ Prominent ligands that are able to be recognised by peptides and proteins when complexed with metals such as copper or nickel are iminodiacetato (IDA), bis(2-pyridylmethyl)amine (BPA), diethylenetriamine (DIEN), nitrilotriacetic acid (NTA) or tris nitrilotriacetic acid (trisNTA), tris(2-pyridylmethyl)amine (TPA), and tri(2-aminoethyl)amine (TREN).^{55,113} This approach finds application in the selective binding of biological molecules for functional and oriented immobilisation,¹¹⁴ and can be successfully used for 2D and 3D protein immobilisation. Polymersomes, functionalised with specific molecular moieties on the outer surface, such as biotin, antibodies, or metal complexes,^{21,23} allow for cellular uptake, protein binding or can be used to be immobilised on solid supports.⁵²

1.7.3. Metal-chelation: NTA and trisNTA

Metal-chelation describes the ability of molecules or ions to bind to metal sites and implies that the binding of a polydentate ligand to the

metal centre consists of at least two coordination bonds. The metal complexes formed with these ligands have a coordination sphere that consists of strongly binding atoms of the ligand and weak binding solvent molecules. The biomolecule interacts with the metal ion as it replaces the solvent molecules and rearranges the geometry. This binding mechanism confers the advantage of stable immobilisation of the biomolecule, similarly to nature.¹¹⁵ In this respect, NTA- and IDA-metal complexes have been used to design synthetic receptors that bind peptides or proteins under physiological conditions.^{113,116} The NTA ligand is widely applied in immobilised-metal affinity chromatography.¹¹⁷ It coordinates for example the Ni^{2+} with four valences as shown Fig. 10.

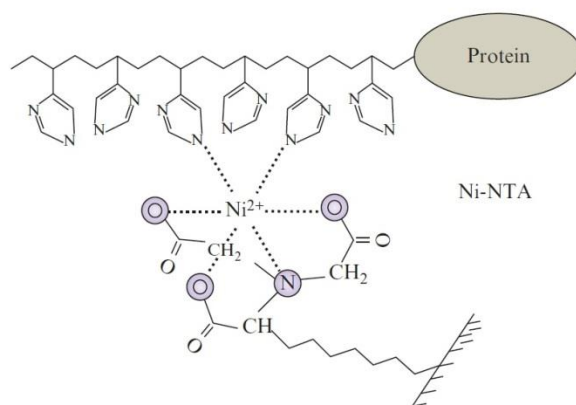


Fig. 10 Model of the interaction between residues in the His-tag and the metal ion in tetra-pentadentate NTA ligand. Reprinted with permission from Ref. 117. Copyright 2009 Elsevier Inc.

In this molecular configuration, two additional valences are available to be coordinated to the imidazole rings of histidine residues. In a further development, increased binding capability was achieved by using trisNTA moieties for protein immobilisation studies. The trisNTA molecules (Fig. 11b, here complexed with Cu^{II}) feature three NTA (Fig. 11a) moieties, all

complexed with a metal ion, which are simultaneously involved in the ligand-binding process.

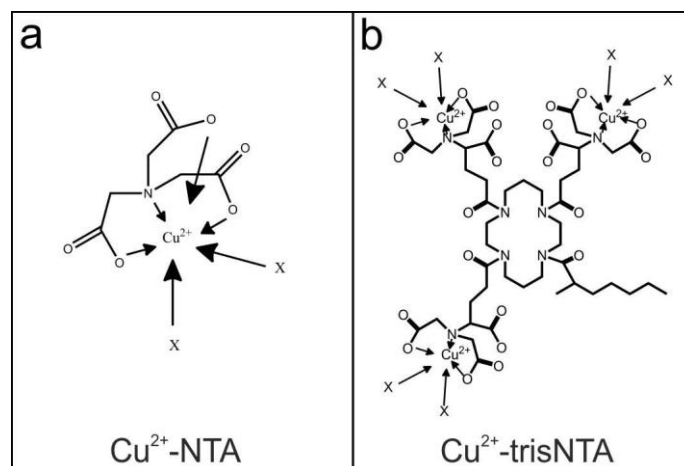


Fig. 11 Schematic formula of a) Cu^{II} -NTA complex and b) Cu^{II} - trisNTA. X represents solvent molecules or external binding atoms of other molecules. Reprinted with permission from Ref. 55. Copyright 2012 American Chemical Society.

1.7.3. His-tags and His-tagged molecules

His-tagged molecules can be used not only for immobilisation or purification purpose of proteins but also in order to study molecular recognition interactions. These molecules most commonly consist of a tag moiety with at least six consecutive histidines covalently bound. Other reported His-tag sequences were summarised in a review of immobilised-metal affinity chromatography.¹¹⁷ The tag moiety has been shown to specifically bind to metal binding sites by a shift of the association/dissociation equilibrium constant to the site of association as a result of the known affinity of histidines to transition metals, such as Zn^{2+} , Cu^{2+} , Ni^{2+} , or Co^{2+} .¹¹⁵ There, typical dissociation rates of different systems were determined to range between 10^{-6} and 10^{-9} M. The

system's properties, such as the used medium, buffer solution, pH, ligand density or concentration or accessibility can have an influence on the binding behaviour. As an example, the oligohistidine sequence consisting of six histidines efficiently interacts with Ni^{II}-NTA complexes with a binding affinity in the subnanomolar range.^{107,118,119} When the number of histidines on each tag was increased, for example, 10 histidines instead of 6 histidines) a decreased metal binding affinity was observed.¹¹⁵ His₆-tag affinity to different transition-metal ions was predicted by molecular dynamic simulations, including Cu²⁺, Fe³⁺, Ni²⁺, and K⁺ ions,. The results indicated that the His₆-tag exhibits the strongest binding affinity for Ni²⁺ and Cu²⁺ ions.¹²⁰

2. Combat superoxide anion radicals by antioxidant nanoreactors

A key challenge in life and nano-sciences is to fuse biological entities, such as enzymes, with synthetic materials, for example block copolymers in order to create new, complex synthetic biological devices. Combination of specificity and efficiency of biological molecules with robustness and possibility of tailoring of polymeric materials allows the design of efficient mimics of living entities, or of electronic-inspired systems, on the nano-scale domain. These out-perform conventional chemical or biological approaches to generate revolutionary, highly-specific communicating or processing systems, such as biosensors, signal amplifiers, electron-transfer devices, or nanoreactors.^{1,25,121} Enzymatic activity can be improved and enzymatic pathways customised by combining synthetic with biological materials, as has been shown by trypsin encapsulation in PS-*b*-PAA block copolymers¹²² or by reconstitution of ubiquinone oxidoreductase in copolymer membranes.⁶⁹ However, a real challenge is related to the preservation of the enzyme activity as well as its integrity when combined with polymeric systems. This renders the situation more complex than in bulk conditions, and requires mild procedures of generating the hybrid systems, as well as to establish the polymer/protein interactions, and their effect on enzyme structure and activity.

Recently such bio-synthetic materials were successfully applied for local bio-conversion on surfaces,⁵³ and inside living cells.⁶¹ Here we plan to extend these concepts to the detoxification of reactive oxygen species (ROS), including the superoxide radical anion ($O_2^{\cdot-}$), peroxy nitrite, hydroxyl radical, and hydrogen peroxide, whose natural production is dramatically increased during oxidative stress.¹²³ Oxidative stress has been reported to play an important role both related to the toxicology of inorganic nanoparticles,¹²⁴ and in the pathogenesis of many diseases,

such as arthritis, Parkinson's disease, amyotrophic lateral sclerosis, cancer, or AIDS.^{89,90,125}

2.1. Motivation and concept

Many attempts to detoxify ROS by direct antioxidant enzyme administration were undertaken, but no conclusive data was obtained. SOD, for example, was quickly eliminated from the blood stream.⁹⁸ In addition, attempts to modify SOD in order to improve delivery were tried. To this end, SOD was covalently modified with poly(ethylene glycol) (PEG)¹²⁶ or encapsulated in liposomes^{127,128} and in polymeric microspheres.¹²⁹ But none of these attempts could improve SOD delivery significantly.

A promising attempt was the design of antioxidant nanoreactors encapsulating SOD inside oxygen permeable polymeric vesicles. The enzyme efficiently catalysed the reaction of superoxide radicals to generate hydrogen peroxide.⁵¹ However, hydrogen peroxide as a final product is well known to still contribute to oxidative damage.¹³⁰ Therefore, in order to detoxify superoxide radicals and related harmful hydrogen peroxide, similar to cellular antioxidant mechanisms, an intricate system must be engineered.

Here, we use this concept in order to engineer advanced nanoreactors based on the encapsulation of two different antioxidant enzymes, superoxide dismutase (SOD) and lactoperoxidase (LPO) or catalase (CAT), in polymersomes for detection and detoxification of reactive oxygen species (ROS). The encapsulated antioxidant enzymes act simultaneously *in situ* while protected from proteolytic attack.^{15,41}

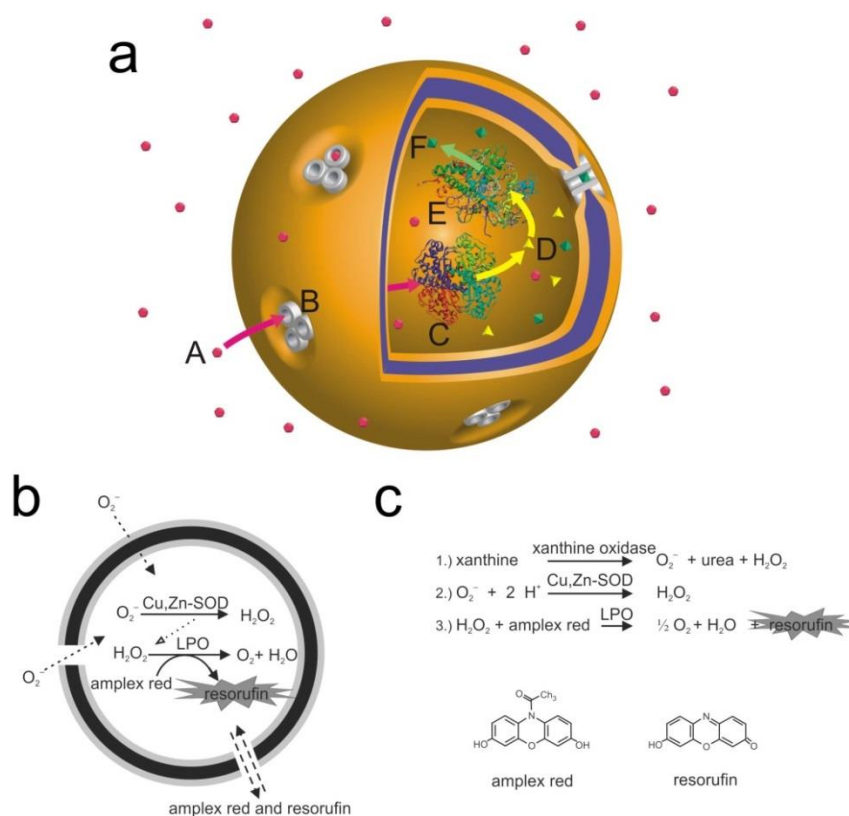


Fig. 12 a) Specialised enzymatic cascade reaction inside polymeric nanovesicles for detection and detoxification of superoxide radicals. Two different types of enzymes act inside the polymersome in a cascade reaction with substrates (D) and products (F) to detoxify reactive oxygen species (A). Substrates, products, and reactive oxygen species penetrate the polymeric membrane due to the insertion of protein channels (B); b) Schematic illustration of the reaction mechanism of the SOD/LPO cascade reaction inside a polymersome; c) Chemical reactions allowing the detection and detoxification of superoxide radicals: 1) generation of O_2^- ; 2) reactions involving SOD; 3) reactions involving LPO. Adapted with permission from Ref. 56. Copyright 2011 Wiley-VCH Verlag GmbH & Co. KGaA.

The selected enzymes catalyse the same reaction in nature. Superoxide radicals can diffuse through the polymer membrane and reach the enzymes, where they were reduced in a cascade reaction to harmless reaction products H_2O and molecular oxygen (Fig. 12b).

In order to observe the detoxification process, i. e. the detection of superoxide radicals and testing the antioxidant activity inside cells, membrane proteins were needed in order to allow the passage of substrates and products of LPO through the polymer membrane, which is highly impermeable to small molecules.⁵⁶ This was realised by the incorporation of the outer membrane protein F (OmpF) in the vesicle membrane to permit passive diffusion of molecules of sizes smaller than 600 Da.⁷⁴ OmpF allowed that a second substrate for LPO, amplex red, was able to penetrate the aqueous cavity of the vesicles, which was converted *in situ* to a fluorescent product, resorufin, so that the activity of the enzymes could directly be observed.

2.2. Design of an enzymatic cascade reaction to fight oxidative stress

The cascade reaction is initialised by SOD, which catalyses the reduction of superoxide radicals, generated for test purpose in the initial reaction by xanthine/xanthine oxidase (Fig. 12c), to hydrogen peroxide at high efficiency. The reaction rate remains unchanged at physiological pH, the condition used here, and appears not to be affected by pH variation in range between pH 6 and 9.¹³¹ In the second step of the cascade reaction, hydrogen peroxide is decomposed by LPO or CAT in presence of one of its specific substrate, amplex red, which is converted to a fluorescent product resorufin that can easily be detected (Fig. 12c). LPO was chosen as a second enzyme due to its high activity at physiological pH – 80% of its activity is preserved,¹³² which makes it compatible to SOD. In addition, the ability to use a second substrate for LPO to generate a fluorescent product in the end of the cascade reaction allows detailed characterisation of the enzyme kinetics in bulk, in the nanoreactor and when used as artificial organelle.

In order to further optimise the cascade reaction, the use of CAT instead of LPO as the second enzyme was considered. CAT plays an important role in the ROS homeostasis of peroxisomes and is therefore a promising enzyme in order to detoxify hydrogen peroxide.

2.3. Design and characterisation of antioxidant nanoreactors

We engineered antioxidant nanoreactors comprising of membrane protein gated polymersomes, which are able to detoxify superoxide anion radicals in the aqueous cavity via a cascade reaction. The cascade reaction is based on the activity of Cu/Zn-SOD, which is the first enzyme, and LPO or catalase (CAT) as the second enzyme.

To provide the reaction cavity, polymersome superstructures were generated from the amphiphilic triblock copolymer poly(2-methyloxazoline)-*b*-poly(dimethylsiloxane)-*b*-poly(2-methyloxazoline) (PMOXA-PDMS-PMOXA) by self-assembly in aqueous solution at physiological condition. The generated vesicles were mechanically very stable,¹³³ and do not comprise of structural defects as known from liposomes. The used polymer membrane is highly permeable to superoxide anion radicals, but impermeable to higher molecular weight molecules such as saccharide ions or water.⁶⁷ The functional incorporation of OmpF in the polymersome membrane allows only a passive diffusion of molecules up to 600 Da⁷⁴ and thus is appropriate for the use with a second substrate for LPO, amplex red, which is converted in the presence of hydrogen peroxide, to a fluorescent product, resorufin. This in turn simplifies the detection of the superoxide anion radical and hydrogen peroxide detoxification process.

Based on the chemical nature and the hydrophobic-to-hydrophilic ratio of the used PMOXA₁₂-PDMS₅₅-PMOXA₁₂ copolymer, polymersome

preparation was made using the direct dissolution method. This method provides mild conditions so that the integrity and activity of different enzymes encapsulated in nanoreactors were preserved.^{56,63}

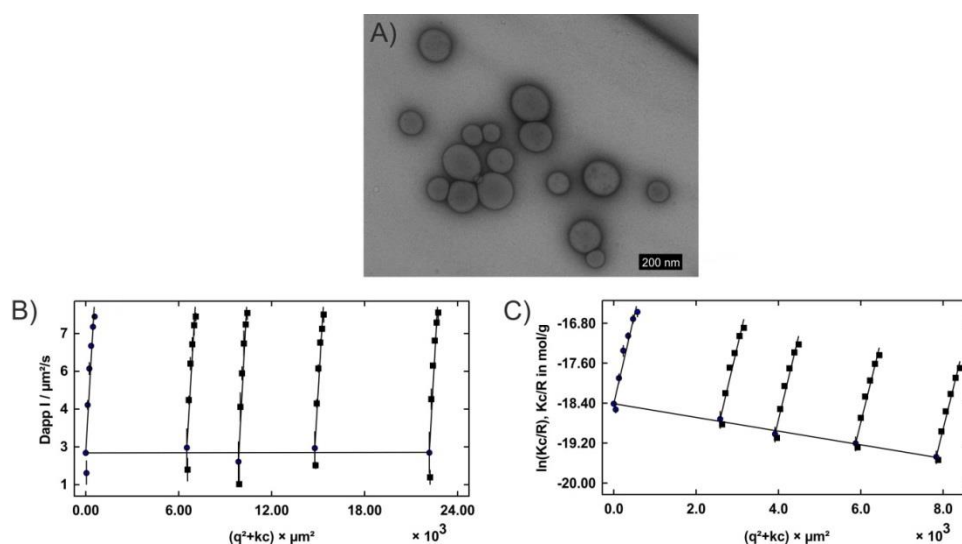


Fig. 13 A) TEM micrograph of empty PMOXA-PDMS-PMOXA polymersomes. Scale bar = 200 nm; Light scattering of empty polymersomes: B) First order fit of DLS data; C) Guinier plot representation of SLS data. Reprinted with permission from Ref. 78. Copyright 2013 American Chemical Society.

Via this preparation method, homogeneous, empty PMOXA-PDMS-PMOXA polymer vesicles with a diameter of 200 ± 40 nm were formed in PBS buffer, as confirmed by TEM (Fig. 13A) and dynamic and static light scattering (Fig. 13B and C).

Membrane permeability was adjusted according to an increase of permeability while keeping the polymersomes intact. An OmpF concentration of $50 \mu\text{g/mL}$ proved optimal for membrane permeability, and did not affect membrane stability.⁷⁰

2.3.1. Optimised encapsulation of individual enzymes in polymersomes

In order to work the best condition out to engineer efficient co-encapsulated antioxidant nanoreactors, characterisation and optimisation of each encapsulated enzyme type must be evaluated individually. In this respect, individual encapsulation efficiencies needed to be assessed – taking care not to induce vesicle aggregation or to disturb the vesicle self-assembly process.

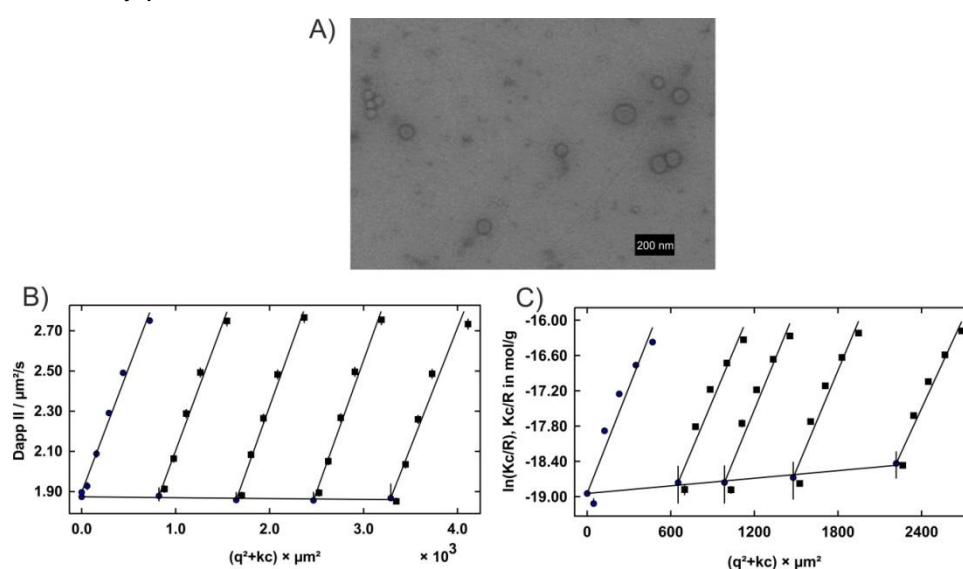


Fig. 14 A) TEM micrograph of SOD-encapsulated PMOXA-PDMS-PMOXA polymersomes. Scale bar = 200 nm; Light scattering of SOD-encapsulated polymersomes: B) Second order fit of DLS data; C) Guinier plot representation of SLS data. Reprinted with permission from Ref. 78. Copyright 2013 American Chemical Society.

The different concentrations used for polymersome preparation did not affect their morphology or size of the nanoreactors, as established by a combination of light scattering and TEM for: SOD (Fig. 14), LPO (Fig. 15), and CAT (Fig. 16).

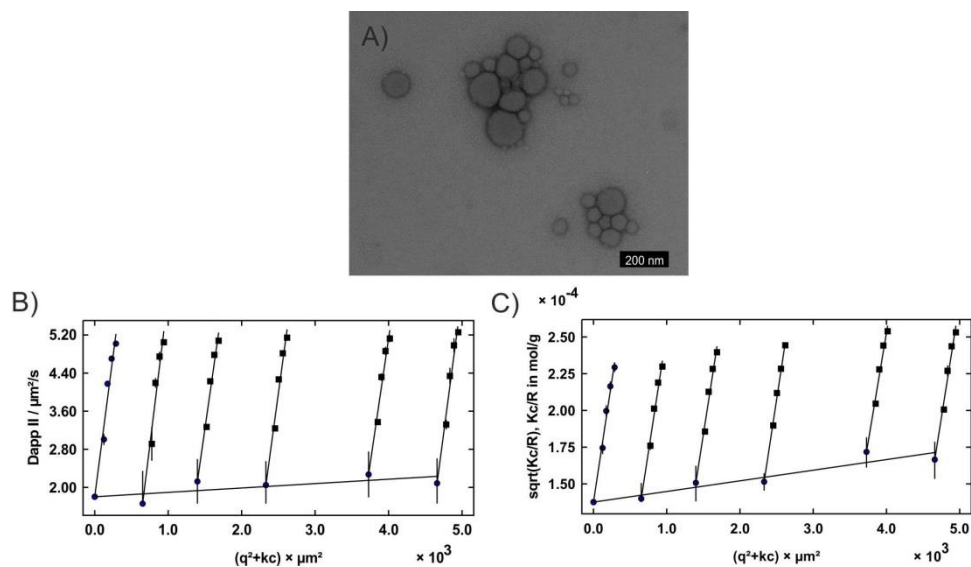


Fig. 15 A) TEM micrograph of LPO-encapsulated PMOXA-PDMS-PMOXA polymersomes. Scale bar = 200 nm; Light scattering of LPO-encapsulated polymersomes: B) Second order fit of DLS data; C) Guinier plot representation of SLS data. Reprinted with permission from Ref. 78. Copyright 2013 American Chemical Society.

In order to measure and quantify the number of encapsulated enzymes and to increase the encapsulation efficiency of enzymes per polymersome, the enzymes were labelled with different fluorescent dyes – AlexaFluor-488 for SOD, AlexaFluor-633 or dylight-633 for LPO, and dylight-488 for CAT – and the efficiency was determined by a combination of fluorescence correlation spectroscopy and fluorescence brightness measurements.

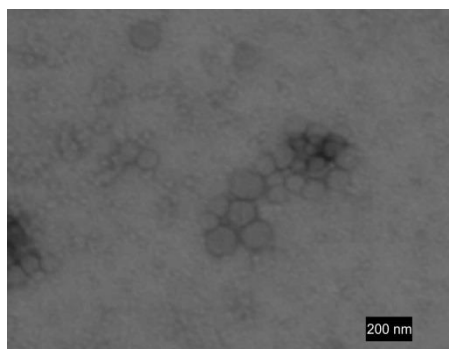


Fig. 16 TEM micrograph of CAT-encapsulated polymersomes. Scale bar = 200 nm. Reprinted with permission from Ref. 78. Copyright 2013 American Chemical Society.

Upon labelling SOD with AlexaFluor-488, a labelling efficiency of three AlexaFluor-488 molecules per SOD was obtained, which was considered for the calculation of the encapsulation efficiency. Furthermore, one AlexaFluor-633 molecule or 2.7 dylight-633 molecules per LPO, and 1 dylight-488 molecule per CAT was achieved.

The molecular brightness of the enzyme-containing polymersomes, recorded as counts per molecules (CPM), was divided by the CPM of freely-diffusing labelled enzymes to determine the number of enzymes per vesicle. This number was then used to calculate the encapsulation efficiency in vesicles (EE_v) based on the initial enzyme concentration by dividing the number of enzyme molecules per polymersome by the maximum number, which could be theoretically encapsulated inside a vesicle via a statistical, self-assembly process of encapsulation. The detailed encapsulation efficiency (EE_v) calculation is shown in the Appendix.

When SOD-AlexaFluor-488 was encapsulated in polymersomes, the diffusion time τ_D changed from 109 μs , which corresponds to the free

SOD-AlexaFluor-488, to a value of 3.5 ± 1 ms, which indicates that the enzyme was encapsulated in vesicles (Fig. 17A).

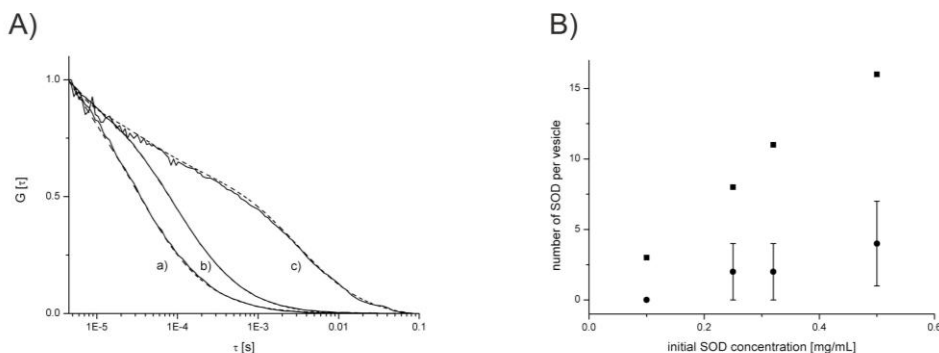


Fig. 17 A) FCS autocorrelation curves and the simulation of: a) free AlexaFluor-488; b) SOD-AlexaFluor-488; c) SOD-AlexaFluor-488-containing vesicles; B) Comparison of the theoretical and experimental amount of enzymes encapsulated in a polymer vesicle as a function of initial enzyme concentration: Theoretical (squares) and experimental (dots) number of SOD encapsulated in 75 nm radius-sized polymersomes. Reprinted with permission from Ref. 78. Copyright 2013 American Chemical Society.

Preparing polymersomes with different initial amounts of SOD-AlexaFluor-488 from 0.1 mg/mL to 0.5 mg/mL allowed the optimisation of a maximum encapsulation efficiency of EE_v of $25 \pm 10\%$ at an initial concentration of 0.25 mg/mL (Fig. 17B). To rule unspecific binding of the enzyme or of the labelled enzyme out, which would affect the calculated number of encapsulated enzymes, control measurements using empty polymersomes incubated with dye-labelled enzymes or with only the dye were performed. In this case, no change of diffusion time was observed, proving that neither AlexaFluor-488 nor SOD-AlexaFluor-488 interact to empty polymersomes. Increasing the SOD concentration used for encapsulation to 0.9 mg/mL caused solubility problems of SOD being the limiting factor of further increase. The resulting high encapsulation efficiency of SOD together with the high reaction kinetics

($k_{\text{cat}} \approx 10^{-9} \text{ M}^{-1} \text{ s}^{-1}$)¹³¹ were basic pre-requisites for efficient antioxidant properties.

Similarly, encapsulation of LPO-AlexaFluor-633 in polymersomes was characterised by a change in the diffusion time from 320 μs , corresponding to the free LPO-AlexaFluor-633, to $8.5 \pm 1 \text{ ms}$, showing successful enzyme encapsulation (Fig. 18A). In order to optimise LPO encapsulation efficiency, differently concentrated enzyme solutions from 0.1 mg/mL to 0.5 mg/mL were used. The optimum EE_v of $66 \pm 33\%$ was reached with an initial LPO concentration of 0.25 mg/mL (Fig. 18B).

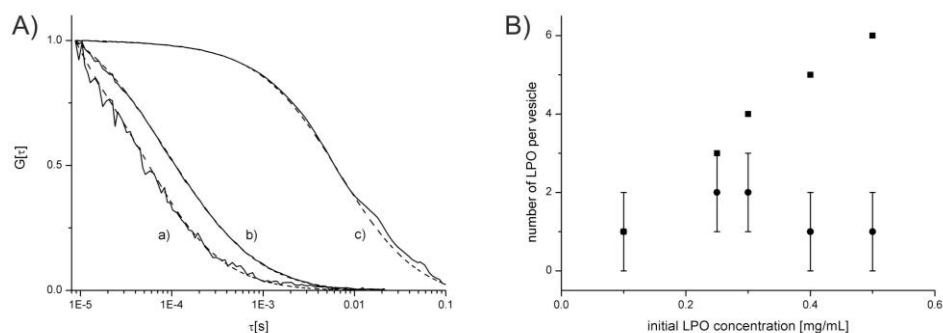


Fig. 18 A) FCS autocorrelation curves and the simulation of: a) free AlexaFluor-633; b) LPO-AlexaFluor-633; c) LPO-AlexaFluor-633-containing polymersomes; B) Comparison of the theoretical and experimental amount of enzymes encapsulated in a polymer vesicle as a function of initial enzyme concentration: Theoretical (squares) and experimental (dots) number of LPO encapsulated in 75 nm radius-sized polymersomes. Reprinted with permission from Ref. 78. Copyright 2013 American Chemical Society.

Further increase of the concentration of LPO-AlexaFluor-633 used for the encapsulation to 0.83 mg/mL led to the formation of aggregates during the self-assembly process, characterised by FCS with diffusion times of $>30 \text{ ms}$ and confirmed by TEM (Fig. 19A and B).

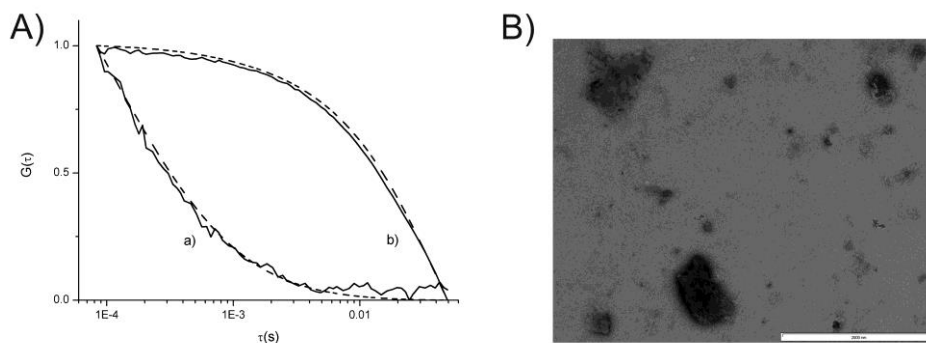


Fig. 19 A) FCS autocorrelation curves and the simulation of: a) free AlexaFluor-633 (50 nM) and b) LPO-AlexaFluor-633-containing aggregates (0.83 mg/mL); B) TEM micrograph of LPO-AlexaFluor-633 containing aggregates. Scale bar = 2 μm . Reprinted with permission from Ref. 78. Copyright 2013 American Chemical Society.

The reason for aggregate formation is the unspecific binding, observed, when free AlexaFluor-633 was incubated with empty polymer-somes, which increased the diffusion time to 7 ms. When a high, initial LPO-AlexaFluor-633 concentration was used for encapsulation, non-encapsulated labelled enzymes served as aggregation points on the outer vesicle surface and induced aggregate formation. When LPO was labelled with dylight-633 using the same high initial concentration, the formation of aggregates could be avoided (Fig. 20).

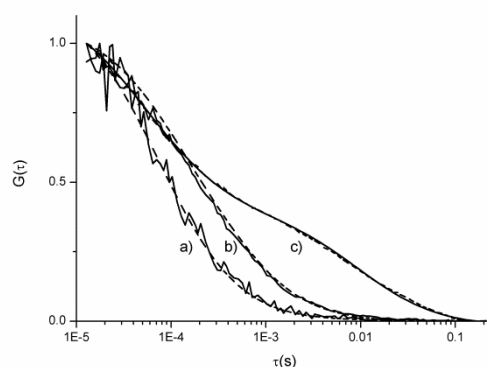


Fig. 20 Fluorescence autocorrelation curves: FCS autocorrelation curves (line) and the simulation (dashed line) of a) free dylight-633 (50 nM); b) dylight-633-labelled LPO (50 nM) and c) empty ABA polymersomes incubated with dylight-633. Reprinted with permission from Ref. 78. Copyright 2013 American Chemical Society.

Nevertheless, aggregate formation is not a limiting factor of the optimisation of the encapsulation efficiency, because the optimum EE_v was obtained at significantly lower concentration. Therefore, all further experiments were conducted with LPO-AlexaFluor-633 for nanoreactor-, and later artificial peroxisome-characterisation.

The modular build-up of nanoreactors allows to exchange enzymes for further adaption to specific functions. Instead of LPO, we used CAT as a second enzyme to test, if the nanoreactor activity could be further increased. CAT is differed from LPO, it detoxifies H_2O_2 in a catalactic reaction without the necessity of additional co-substrates and it has a higher molecular weight of 250 kDa.¹³⁴ When CAT-dylight-488 was encapsulated, FCS measurements resulted in diffusion times of 4 ± 1 ms, which can be attributed to CAT-dylight-488-containing polymersomes (Fig. 21c). On the other hand, a diffusion time of 340 μ s was characteristic of the free, labelled-enzyme (Fig. 21a), whereas the

diffusion time for the free dye was 44 μs . No aggregates were formed for all different CAT concentrations used during vesicle formation.

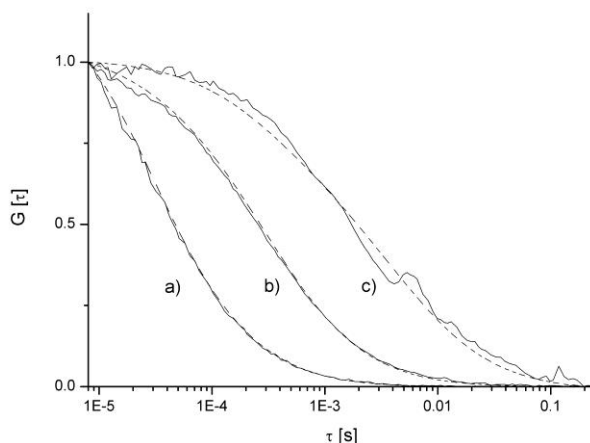


Fig. 21 Normalized FCS autocorrelation curves (lines) and the simulation (dashed lines) of a) free dylight-488; b) CAT-dylight-488 and c) CAT-dylight-488-containing PMOXA₁₂-PDMS₅₅-PMOXA₁₂ vesicles. Reprinted with permission from Ref. 78. Copyright 2013 American Chemical Society.

A maximal EE_v of $16 \pm 9\%$ was calculated based on brightness measurements, which is lower compared to LPO. This can be explained by the higher molecular weight of CAT compared to LPO, which creates problems for efficient encapsulation, as shown before with lipid vesicles.¹³⁵

2.3.2. Activity assay of individual enzyme species in solution and in polymersomes

LPO activity of the free enzyme in solution and encapsulated in polymersomes was determined by using an activity assay comprising of amplex red, which is converted by LPO in presence of hydrogen peroxide to resorufin, shown in Fig. 22A and B, respectively.

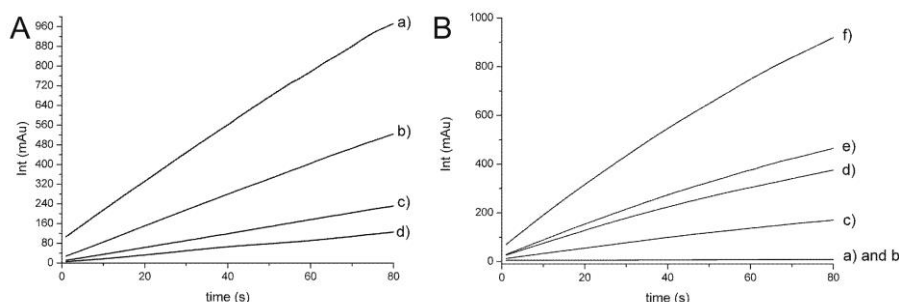


Fig. 22 A) Activity assay for LPO in free conditions with different concentrations of amplex red: a) 3.75 μM ; b) 1.88 μM ; c) 0.94 μM and d) 0.47 μM . B) Activity assay of: a) empty polymersomes (amplex red 0.5 μM); b) LPO encapsulated in polymersomes without channel proteins (amplex red 0.5 μM) and LPO encapsulated in polymersomes with channel proteins and with gradient of amplex red: c) 0.18 μM ; d) 0.37 μM ; e) 0.5 μM and f) 1 μM . Reprinted with permission from Ref. 56. Copyright 2011 Wiley-VCH Verlag GmbH & Co. KGaA.

In order to measure enzyme kinetics, different substrate concentrations of amplex red were used. As expected, polymersomes containing LPO without OmpF gated membranes produced no resorufin signal. On the other hand, LPO containing vesicles with gated membranes clearly converted amplex red to resorufin in proportion to the initial substrate concentration. This demonstrates that OmpF allows substrates diffusing through the membrane.

Calculation of the kinetic constants for the LPO enzymatic reaction (K_M and V_{max}) in free conditions compared to encapsulated conditions using the Lineweaver-Burk equation¹³⁶ gave information about the preservation of enzyme activity. This showed that substrate affinity to LPO in nanovesicles is slightly higher (K_M value of $2.9 \pm 0.1 \mu\text{M}$) compared to free conditions (K_M value of $9.4 \pm 0.3 \mu\text{M}$). Higher substrate affinities in encapsulated condition have already been reported,¹²² which results from higher collision frequencies, due to the location of both enzyme and substrate at the same interface. Comparison of the maximal reaction

rates V_{\max} of the encapsulated enzyme ($37.1 \pm 7.1 \mu\text{Ms}^{-1}$) with the enzyme in free condition ($132.3 \pm 75.9 \mu\text{Ms}^{-1}$) shows that it is lower in the encapsulated condition, but still comparable to the free condition.

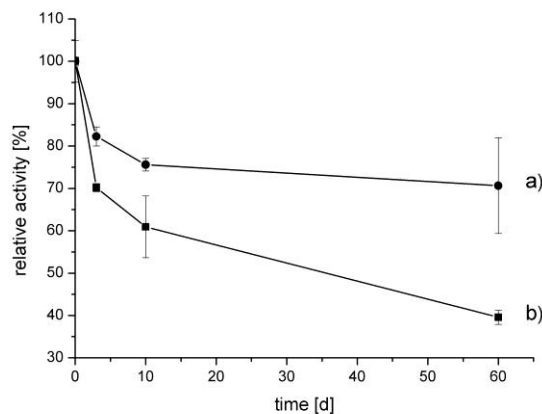


Fig. 23 LPO activity over time, when a) encapsulated in polymersomes and b) in free condition. Reprinted with permission from Ref. 56. Copyright 2011 Wiley-VCH Verlag GmbH & Co. KGaA.

The stability of encapsulated LPO was also compared to free LPO over a time period of 60 days (Fig. 23); both systems were stored in dark at 4 °C. After 60 days, LPO activity inside the polymersomes was still approximately 70%, while the activity of LPO free in solution decreased to 40%, which could be a result of possible contamination with small amounts of proteases of the free enzyme containing solution. This further confirms that the aqueous cavity of the polymersomes provides advantageous conditions for the enzyme in means of protection, which was also reported for SOD containing polymersomes.⁵¹

During the optimisation of the antioxidant nanoreactor, we also compared the enzyme kinetics of LPO-containing polymersomes to that of CAT-containing polymersomes according to the activity assay presented in Scheme 1. At comparable concentrations of LPO and CAT

in free condition adjusted to the concentration range expected to be present in polymersomes, CAT activity was comparable to the activity of LPO (Fig. 24A). CAT activity was also measured in CAT-encapsulated polymer vesicles. The successful incorporation of the channel protein OmpF, which allows passage of H_2O_2 and amplex red through the membrane, led to a clear decrease in the fluorescence signal (Fig. 24B b) compared to the condition in which no CAT-encapsulated polymer vesicles were present (Fig. 24B a). Thus, CAT was encapsulated in an active form.

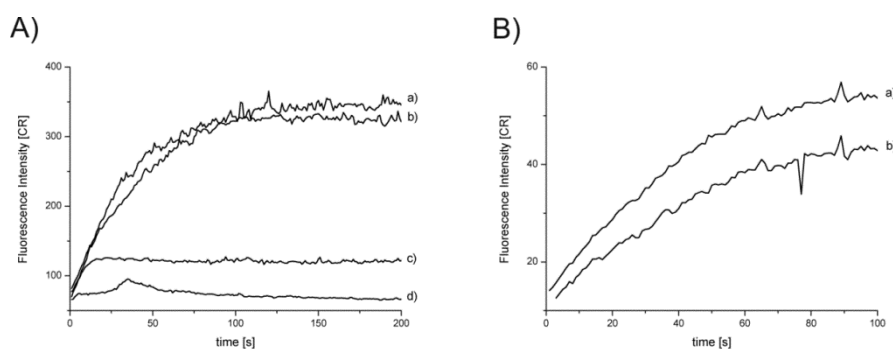


Fig. 24 A) CAT activity assay based on an assay containing LPO (50 nM), H_2O_2 (3 μM) and amplex red (0.5 μM) to monitor CAT activity in free conditions using different CAT concentrations: a) 0 nM; b) 10 nM; c) 50 nM; d) 100 nM. B) CAT activity assay based on an assay containing LPO (10 nM), H_2O_2 (0.6 μM) and amplex red (0.1 μM) to monitor CAT activity: a) without nanovesicles; b) in nanovesicles with incorporated OmpF channel membrane. [CR] = count rate. Reprinted with permission from Ref. 78. Copyright 2013 American Chemical Society.

Similar kinetics between peroxidases and CAT at low substrate concentrations and under physiological conditions have already been reported.¹³⁷ But the result of the lower encapsulation efficiency of CAT compared to LPO makes hydrogen peroxide degradation by CAT-containing polymersomes less effective. The determinant of the enzyme activity is in this case the encapsulation efficiency and not the specificity

of the enzyme. Therefore, further experiments were performed using only LPO as second enzyme.

2.3.3. Optimised co-encapsulation of SOD and LPO in polymersomes

Superoxide radical detoxification by the antioxidant nanoreactors needs successful co-encapsulation of both enzyme types, SOD and LPO, in polymersomes.

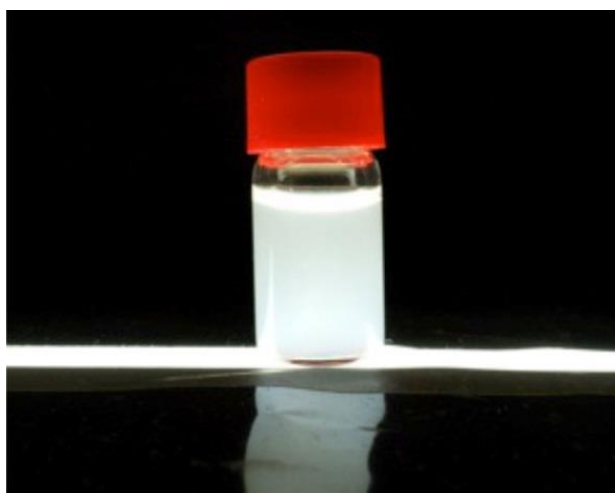


Fig. 25 Turbid solution containing SOD/LPO-co-encapsulated polymersomes. (Sample after size-exclusion- and dye separation (dialysis) process.) Reprinted with permission from Ref. 78. Copyright 2013 American Chemical Society.

The simultaneous co-encapsulation, using the optimised condition of each individual enzyme type and self-assembly of the block copolymer produced a turbid solution (Fig. 25). Co-encapsulation did not affect the morphology or the size of the vesicles, as shown by TEM and light scattering (Fig. 26A, B and C).

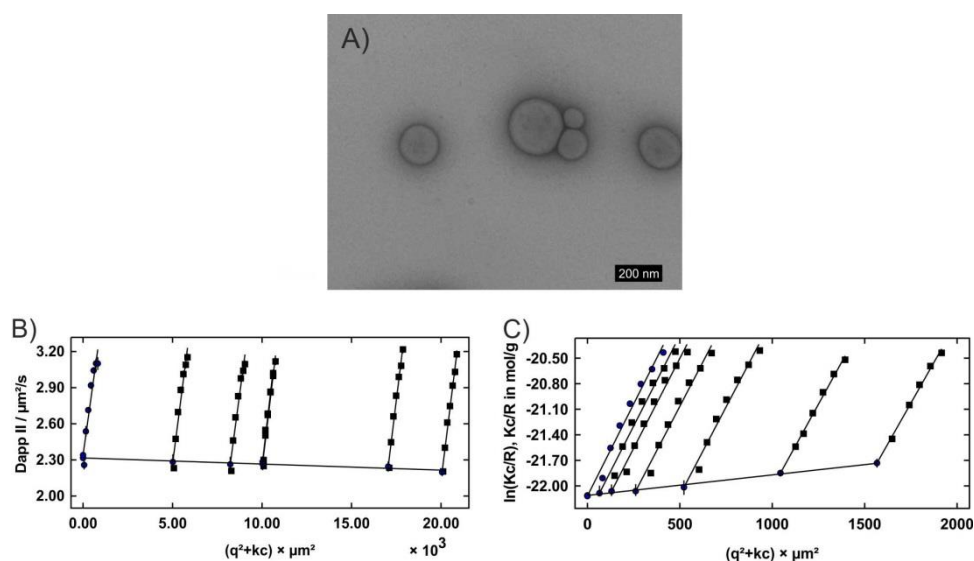


Fig. 26 A) TEM micrograph of SOD/LPO co-encapsulated polymersomes; Light scattering data for SOD/LPO-co-encapsulated vesicles: B) Second order fits of DLS data; C) Guinier plot representation of SLS data. Adapted with permission from Ref. 78. Copyright 2013 American Chemical Society.

In order to relate the ROS detoxification efficacy with the quantity of co-encapsulated enzymes, fluorescence cross-correlation spectroscopy (FCCS) was used. Because the encapsulation of the enzymes inside polymersomes is based on a probabilistic process due to the unspecific inclusion of molecules during the self-assembly process in vesicles, the encapsulation of two different types of enzymes can produce the following scenario. Either only one type of enzyme is encapsulated, none of them were encapsulated, or both types of enzymes were simultaneously encapsulated. In order to quantify the co-encapsulation, FCCS is used, which is based on monitoring the fluorescence intensity fluctuation of two fluorescent species in overlaying confocal volumes. If the two species are moving in a simultaneous way, e.g. when located inside the same confinement, a cross-correlation can be calculated, which is proportional

to the degree of simultaneous movement. This technique allows to determine the degree of co-localisation of the fluorescently labelled enzymes SOD and LPO in the same polymersome.

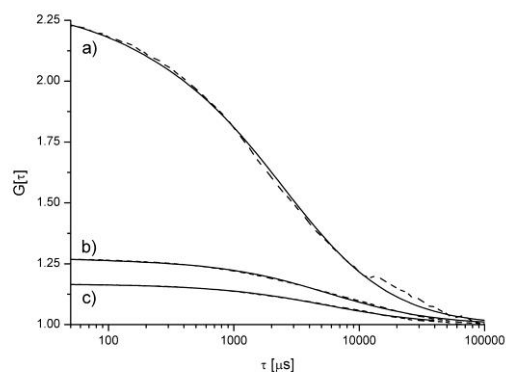


Fig. 27 FCS and FCCS of SOD/LPO co-encapsulated polymersomes: a) autocorrelation curves of vesicles containing SOD-AlexaFluor-488; b) autocorrelation curves of vesicles containing LPO-AlexaFluor-633, and c) Cross-correlation curves of SOD-AlexaFluor-488 and LPO-AlexaFluor-633 co-encapsulated in the polymersomes. Dotted lines are experimental curves. Reprinted with permission from Ref. 78. Copyright 2013 American Chemical Society.

Successful co-encapsulation was obtained, as shown in the positive cross-correlation curve of the FCCS measurement (Fig. 27c). Qualitative analysis of the fluorescence brightness measured in each channel (Fig. 27a and b) of the FCS measurement revealed that an enzyme ratio of SOD:LPO of 1:2 was present inside the polymersomes. Fluorescence from the first species detected in the second channel and vice versa, also known as cross-talk, was negligible (<0.5 kHz) in the FCCS experiment, due to the well-separated fluorescence emission spectra of AlexaFluor-488 and AlexaFluor-633. Calculation of the relative amplitude of the cross-correlation curve in relation to the amplitude of the auto-correlation curve allows calculating that approximately $22 \pm 10\%$ of the polymersomes contained simultaneously both enzymes. This is close to

the value of a theoretical calculation, based on the self-assembly process of vesicle formation during individual enzyme encapsulation.

2.3.4. Multi-enzyme kinetics in a solution that simulates polymersome conditions

In order to carry out complex reaction as efficiently and in accordance with nature, specific enzyme functionality in multi-enzyme systems needs to be maintained. Based on the result of the FCS/FCCS quantitative analysis, activity tests of the SOD/LPO cascade reaction in solution under conditions simulating the concentration ranges of enzymes encapsulated in polymersomes were performed.

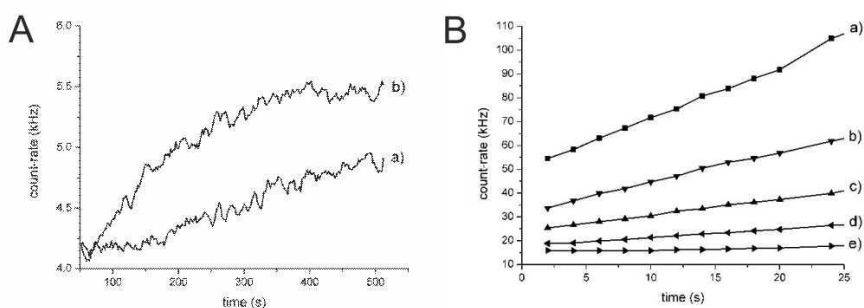


Fig. 28 A) Cascade reaction in free conditions (xanthine (XA): 25 μM ; xanthine oxidase (XO): 0.17 U/mL; LPO: 16 nM): without SOD a), and with SOD (205 nM) b). Both curves were smoothed via adjacent-averaging. B) Cascade reaction in free conditions (XA: 25 μM ; XO: 0.17 U/mL; LPO: 1.6 nM; SOD: 205 nM) for a gradient of amplex red: a) 12.5 μM ; b) 8.4 μM ; c) 5.6 μM ; d) 3.3 μM and e) 1.7 μM . Reprinted with permission from Ref. 56. Copyright 2011 Wiley-VCH Verlag GmbH & Co. KGaA.

In the SOD/LPO cascade reaction, the slope is increased in the presence of SOD (Fig. 28A b) showing that the reaction completely detoxifies superoxide radicals via hydrogen peroxide to water and molecular oxygen. In comparison, when SOD is absent (Fig. 28A a), the signal intensity is clearly reduced, which was taken into account as background signal together with amplex red autooxidation. Because

these effects can be neglected for other activity tests at high enzyme concentration, the kinetics of encapsulated enzymes (Fig. 28B) will only be compared to that of free enzymes in solution providing similar concentration conditions as observed in nanovesicles.

2.3.5. Multi-enzyme kinetics *in situ* inside polymersomes

Optimisation of the co-encapsulation by the selection of optimal enzyme concentrations and ratios allows a very efficient cascade reaction, taking place *in situ* in the polymersome cavity, where superoxide radicals were successfully reduced to molecular oxygen and water (Fig. 29A a). Resorufin, the product generated in the step by LPO in presence of hydrogen peroxide was detected by fluorescent measurements. The FCS set-up was used in these measurements due to its high sensitivity and the requirement of only low sample volume.

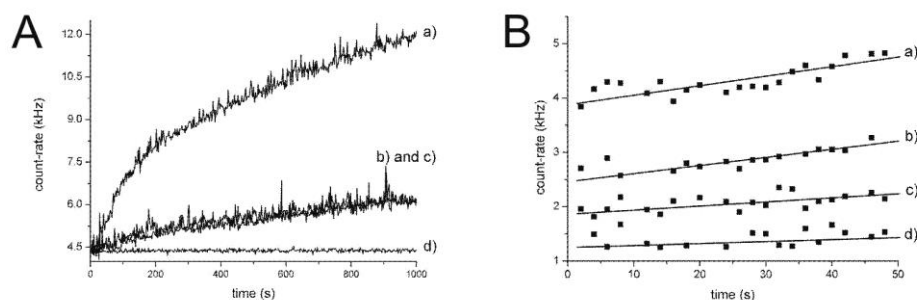


Fig. 29 A) Cascade reaction of: a) SOD-LPO-loaded nanocontainers with OmpF inserted inside the polymer membrane; b) SOD-LPO-loaded nanocontainers without OmpF inserted inside the polymer membrane; c) LPO-containing vesicles with OmpF inserted inside polymer membrane and d) empty polymer vesicles in the presence of amplex red. B) Cascade reaction of SOD-LPO-loaded nanocontainers with OmpF inserted inside the polymer membrane with added amplex red gradient (XA: 25 μM ; XO: 0.17 U/mL): a) 16.7 μM ; b) 8.3 μM ; c) 4.16 μM ; d) 1.7 μM . Adapted with permission from Ref. 56. Copyright 2011 Wiley-VCH Verlag GmbH & Co. KGaA.

SOD/LPO co-encapsulated polymersomes without OmpF (Fig. 29A b) showed low resorufin formation, which can be attributed to non-encapsulated LPO, which is still present in low amount after polymersome purification and is able to oxidise amplex red in presence of H_2O_2 generated by xanthine/xanthine oxidase (XA/XO) as a by-product. Similarly, LPO-encapsulated polymersomes with OmpF, but lacking of SOD also showed low resorufin formation, which was detected due to the generation of H_2O_2 generated by XA/XO (Fig. 29A c). The used triblock copolymer did not induce amplex red autoxidation (Fig. 29A d). In contrast, SOD/LPO containing polymersomes with OmpF reconstituted channels were able to generate a considerable amount of resorufin (Fig. 29A a), which is characteristic for a complete cascade reaction. In direct comparison to SOD/LPO containing polymersomes without reconstituted OmpF (Fig. 29A b), resorufin intensity was clearly decreased. These results are in agreement with FCCS measurements, which already proved successful co-encapsulation.

SOD/LPO containing polymersomes with reconstituted OmpF could statistically co-exist with polymersomes without OmpF. Based on the OmpF concentration employed, approximately 14 OmpF molecules are embedded in one polymersome. Due to this high amount of channels per polymersome and the statistical distribution of channels, the probability that a polymersome contains no channels should be small.

In order to qualitatively analyse this cascade reaction, the Michaelis-Menten kinetic approach has shown to be a suitable model, e. g. in characterising HRP in the glucose oxidase/horseradish peroxidase tandem reaction.¹³⁸ Even if the signal to noise ratio is at the detection limit due to being close to the single molecule level, Michaelis-Menten kinetics provided reliable results.¹³⁹ Therefore, we applied the Michaelis-Menten kinetic to extract the kinetic parameters of the SOD/LPO cascade reaction

in free condition (for single molecules) and inside polymersomes (in bulk: Fig. 28B and in polymersome condition: Fig. 29B).

Calculation of the Michaelis-Menten constant K_M revealed a value of $1.1 \pm 0.1 \mu\text{M}$ in free condition, which is lower compared to the value of $7.3 \pm 0.4 \mu\text{M}$ for the SOD/LPO containing nanoreactors, because the co-encapsulation is limited by the encapsulation efficiencies of the individual enzymes as confirmed by FCCS. The individual enzymes containing polymersomes also contribute to the overall cascade reaction, but this reaction pathway is less effective than the pathway occurring in the co-encapsulated polymersomes, because the hydrogen peroxide, converted by SOD containing polymersomes, needs to exit the polymersome and need to get in contact with polymersomes containing either SOD/LPO or only LPO. However, the condition of excess of H_2O_2 is fulfilled due to the extremely high SOD reaction speed and the presence of OmpF, which allows good accessibility of the enzymes so that Michael-Menten kinetics can be simulated.

With respect to V_{max} , a value of $11.1 \mu\text{Ms}^{-1}$ for enzymes in bulk compared to the value of $0.02 \mu\text{Ms}^{-1}$ shows the same trend as for single enzyme encapsulation, where the conversion rate of the enzyme is higher in bulk condition, because the substrate needs to pass through the membrane proteins in order to reach the reaction volume inside the polymersomes.

2.4. Combating superoxide anion radicals in cells by artificial peroxisomes

Polymersomes are qualified for the use inside cells due to their intrinsic properties such as high stability and their limited miscibility with phospholipids.¹⁴⁰ Artificial organelles can be designed by the successful uptake of polymersomes containing the desired enzymes in cells,

providing that the enzymatic activity inside the polymersomes is preserved under cellular conditions. The combination of the naturally occurring enzymes SOD and LPO in synthetic polymersomes generates a hybrid system, which shares the functionality and properties of peroxisomes (morphology and size from 200 nm to 1.1 μm)¹⁴¹ when implanted in cells.

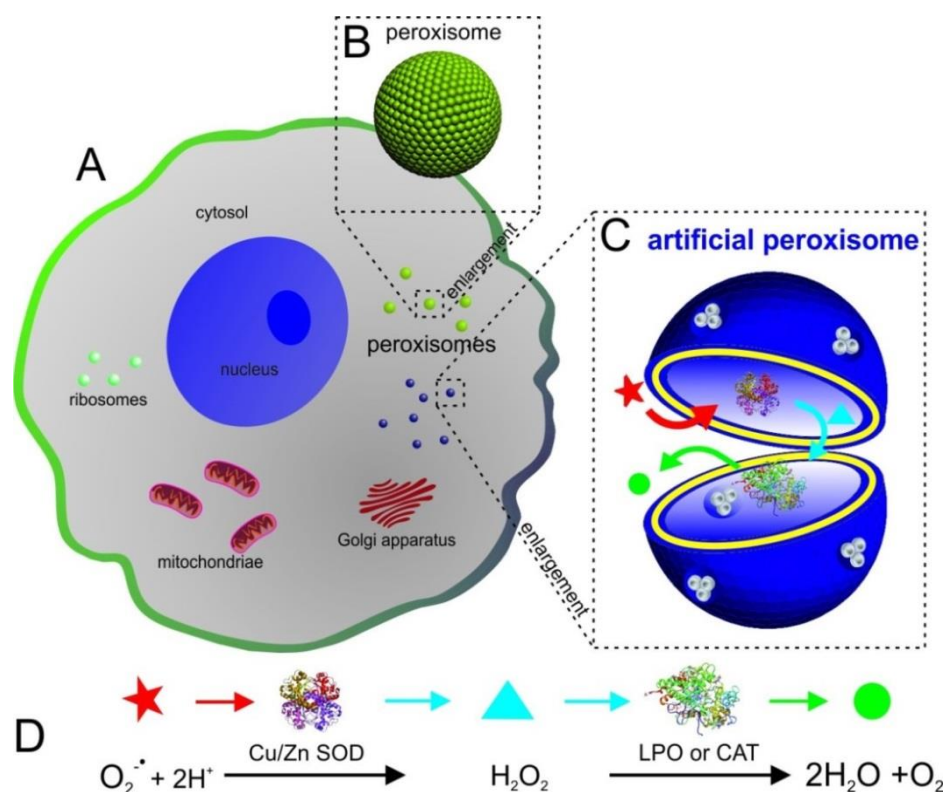


Fig. 30 A) Schematic view of a cell showing various organelles. B) Peroxisomes are spherical, cell organelles of sizes in the nanometre range that play a significant role in the regulation of ROS. C) An artificial peroxisome (AP) is based on the simultaneous encapsulation of a set of antioxidant enzymes in a polymer vesicle, with a membrane equipped with channel proteins. The APs serve for ROS detoxification inside cells. D) Schematic enzymatic cascade reaction occurring inside the AP and serving to detoxify superoxide radicals and related H_2O_2 . Reprinted with permission from Ref. 78. Copyright 2013 American Chemical Society.

The aim is to combat reactive oxygen species (ROS) in cells (Fig. 30). Thus, designing efficient artificial peroxisomes (AP) (Fig. 30C) requires an understanding of their integration into cells and the influence of their properties on cellular interactions. Cell integration and preservation of function needs that toxicity, cell-uptake of the polymersomes, intracellular trafficking and translocation and functionality in intra-cellular conditions must be studied.

2.4.1. Integration of artificial peroxisomes in cells

The first requirement of the compatibility to use artificial peroxisomes (APs) in living systems is to assess possible toxic effect to cells. The toxicity of APs was evaluated by a MTS assay in the HeLa cell line. APs exhibit minimal *in vitro* cytotoxicity in HeLa cells for a period of up to 48 hours (Fig. 31A).

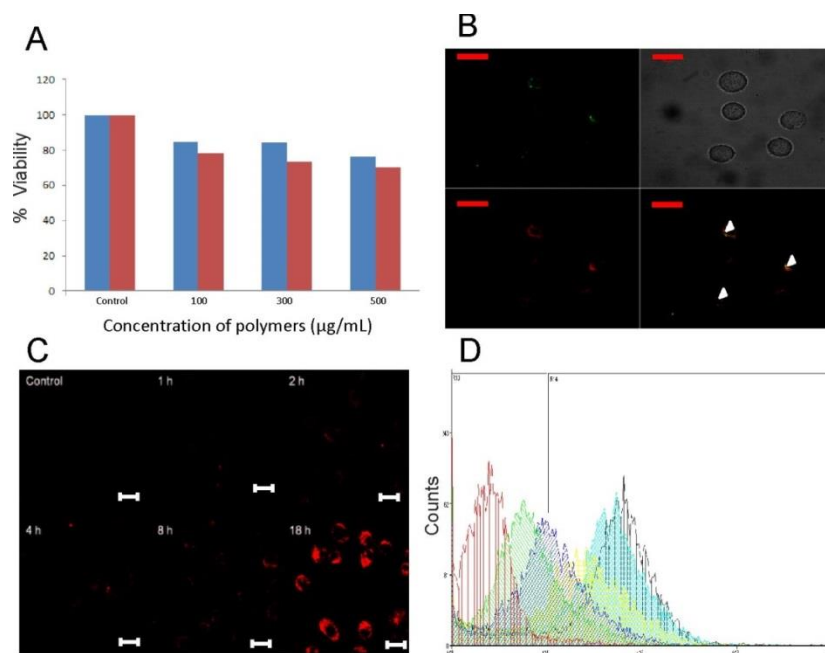


Fig. 31 A) Viability in HeLa cells after incubation with different concentrations of APs (MTS assay). Blue bars: incubation time 24 h, red bars: incubation time 48 h. B) CLSM images of HeLa cells incubated with APs containing SOD-AlexaFluor-488 and LPO-AlexaFluor-633 for 24 h (Scale bar = 20 µm). C) CLSM images of HeLa cells incubated with APs containing SOD and LPO-AlexaFluor-633 for different incubation times. (Scale bar = 20 µm). D) Flow cytometry analysis of APs in HeLa cells for different incubation times (0-, 2-, 4-, 8-, 18-, 24 h). Reprinted with permission from Ref. 78. Copyright 2013 American Chemical Society.

This is in agreement with the reported non-toxicity of PMOXA-PDMS-PMOXA-based copolymers with different block lengths studied in other cell lines.^{57,62}

The first interaction of an AP with a cell is the interaction with the cell membrane, which determines a possible uptake in the following step. To this end, we studied the uptake behaviour into HeLa cells of AP co-encapsulated with SOD-AlexaFluor-488 and LPO-AlexaFluor-633. By the use of a dual channel confocal fluorescence microscope, co-localisation of a fluorescence signal coming from SOD-AlexaFluor-488 and of a signal from LPO-AlexaFluor-633 showed that both enzymes were uptaken in

cells (Fig. 31B). This is the first time that two different types of enzymes capable of working in tandem in polymersomes are uptaken in cells.

Although two different enzymes were loaded in polymer vesicles earlier by us and others,^{56,142} here we demonstrate for the first time the presence of nanoreactors containing both enzymes in cellular system. Further, we directly evidenced the effect of initial concentration dependent co-encapsulation efficiencies of SOD-LPO enzymes inside nanoreactors in intra-cellular conditions (Fig. 32). The concentration of SOD inside nanoreactors (number of enzymes) can be increased to only a certain extent, probably due to solubility. This effect was demonstrated by FCS measurements used to determine the number of SOD per vesicle as a function of SOD concentration (Fig. 17). However, we observed reduced SOD fluorescence intensity, due to the interaction of LPO AlexaFluor-633 with the copolymer, which suppresses SOD encapsulation efficiency during the co-encapsulation process. FCS and FCCS experiments corroborated well with cellular uptake studies.

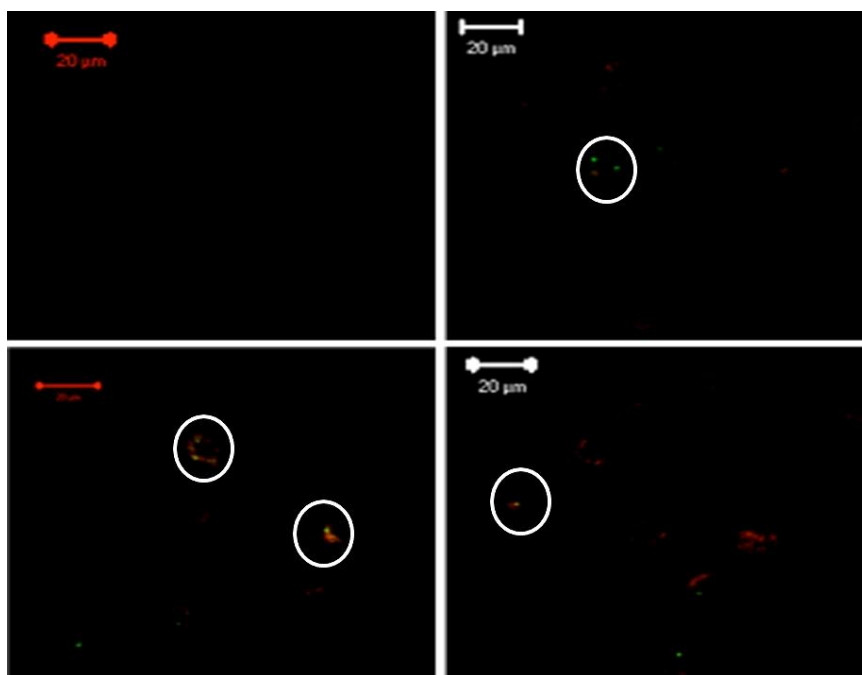


Fig. 32 Confocal image of HeLa cells incubated with SOD-LPO co-encapsulated in PMOXA_{12} -PDMS₅₅- PMOXA_{12} polymersomes prepared with different initial concentrations. a) Control cells b) initial concentration of SOD (0.25 mg/mL) and LPO (0.1 mg/mL) c) initial concentration of SOD (0.5 mg/mL) and LPO (0.2 mg/mL) d) initial concentration of SOD (0.25 mg/mL) and LPO (0.5 mg/mL). Reprinted with permission from Ref. 78. Copyright 2013 American Chemical Society.

However, for detailed uptake kinetics experiments, we used APs only encapsulated with AlexaFluor-633 labelled LPO to simplify the measurements. Cellular uptake was increased with time from 2h to 18h indicating time dependent internalisation of APs (Fig. 31C). Fluorescence intensity varied from cell to cell, suggesting the number of internalised APs in individual cells is different due to non-specific interactions and miscellaneous level of direct contact to the cells at the close proximity.

In general, cellular uptake is directly related to the concentration of nanoparticles. However, aggregation can dramatically influence the dose

of nanoparticle exposed to a cell, changing the exposed concentration compared to the initial bulk concentration.¹⁴³ Aggregation behaviour will not only affect the concentration of APs exposed to a cell surface, but also change the properties of the APs by having some enzymes outside which may mislead to inaccurate activity assessments. To test this hypothesis, we studied the uptake kinetics of APs containing two different initial concentrations of LPO-AlexaFluor-633 (0.25 mg/mL and 0.83 mg/mL). As we studied the effect of initial enzyme concentration on encapsulation efficiency and aggregation (FCS experiments), we carefully choose those two different initial concentrations. At low concentration (0.25 mg/mL), no aggregation is observed (Fig. 18A), while the higher concentrated system (0.83 mg/mL) allows to study aggregation behaviour that was characterised by FCS (Fig. 19A). The rate of uptake was quantified by using flow cytometry based on the mean cell fluorescence corresponding to overall cell population. APs containing LPO-AlexaFluor-633 (0.25 mg/mL) showed minimal uptake of around 10% after 2 h. Uptake linearly increased over time and reached a plateau at 85% after 18h: cells were saturated with the uptake of APs after 18h under the used experimental conditions. This saturation might be due to a depletion of APs for the uptake or saturation of the storage capacity of cells.^{144,145} APs containing LPO-AlexaFluor-633 at a concentration of 0.83 mg/mL forming aggregates as observed by TEM and FCS showed a dramatic change in the uptake reaching 60% after 2 h incubation time compared to APs containing LPO-AlexaFluor-633 (0.25 mg/mL). This indicates that aggregation can dramatically influence the dose of APs in cellular uptake as well as the internalisation kinetics.

The uptake kinetics can also depend on the mechanism of the internalisation pathway.¹⁴⁶ The effects of several membrane entry inhibitors on nanoreactor uptake were examined by first incubating the

HeLa cells for 1 h at 37 °C with chlorpromazine (10 µg/mL) in order to inhibit the formation of clathrin vesicles, filipin III (1 µg/mL) to inhibit caveolae, or amiloride (50 µM) to inhibit macropinocytosis, and then treating the cells with nanoreactors (100 µg/mL) for an additional 24 h. Next, the cells were washed twice with PBS (pH 7.2) and analysed with flow cytometry.

Nanoreactors are generally internalised by cells through various endocytotic pathways. Understanding the route of entry into cells for nanoreactors is important because it determines intracellular fate and therapeutic efficacy. Uptake kinetics can also depend on the mechanism of the internalisation pathway. Preliminary experiments to detect the mechanism of internalisation by using specific endocytosis pathway inhibitors were analysed in flow cytometry (Fig. 33). The quantified data suggest that at least two different pathways were involved in nanoreactor uptake; clathrin-mediated endocytosis and macropinocytosis. Cellular uptake of APs is dramatically hampered by amiloride, an inhibitor of macropinocytosis (70%). Thus, macropinocytosis is one of the dominant uptake pathways and is known for non-specific uptake; therefore, aggregation strongly affects cellular uptake kinetics based on the route of entry mechanism. Often more than one endocytotic pathway is involved in the uptake of polymeric nanoparticles and particularly so in the case of non-specific uptake.¹⁴⁷

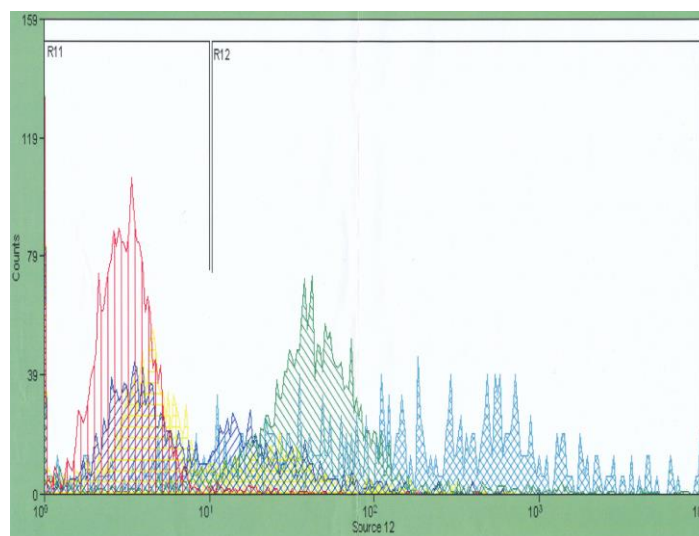


Fig. 33 Flow cytometry analysis of LPO encapsulated in PMOXA₁₂-PDMS₅₅-PMOXA₁₂ vesicles in HeLa cells with different endocytotic pathway inhibitors (red: non-treated cells, green: cells treated with nanoreactors without inhibitors yellow: cells treated in advance with nanoreactors and with chlorpromazine, blue: cells treated in advance with nanoreactors and with dimethyl amiloride, light blue: cells treated in advance with nanoreactors and with filipin III). Reprinted with permission from Ref. 78. Copyright 2013 American Chemical Society.

When nanoreactors serve as APs inside cells, endosomal escape is a critical requirement. To evaluate whether APs escape endosomes or are trafficked for degradation, we used an endo-lysosome marker, pH-rodo, and visualised cells by confocal laser-scanning microscopy (CLSM). The majority of APs were located in intracellular regions, particularly in the peri-nuclear region, and only few were stayed in endo-lysosome compartments (Fig. 34A). Based on the fluorescent signals from the peri-nuclear region, it can be concluded that APs escaped from endosomes. Co-localisation signals of endo-lysosome compartments and APs imply that APs were transported through endocytosis. By visualisation of the intracellular localisation of APs with TEM, further insight into endosomal escape was gained. TEM micrography proved the presence of structurally

intact APs in peri-nuclear regions, with only a few collapsed APs (Fig. 34B). In endosome-like compartments, the APs were present in clearly reduced number (Fig. 34C). Intact APs escaped from endosomes and were allocated in the cytoplasm, which is in agreement with the CLSM co-localisation studies. Escape from endosomes by PMOXA-PDMS-PMOXA vesicles has already been reported in THP-1 cells.⁶²

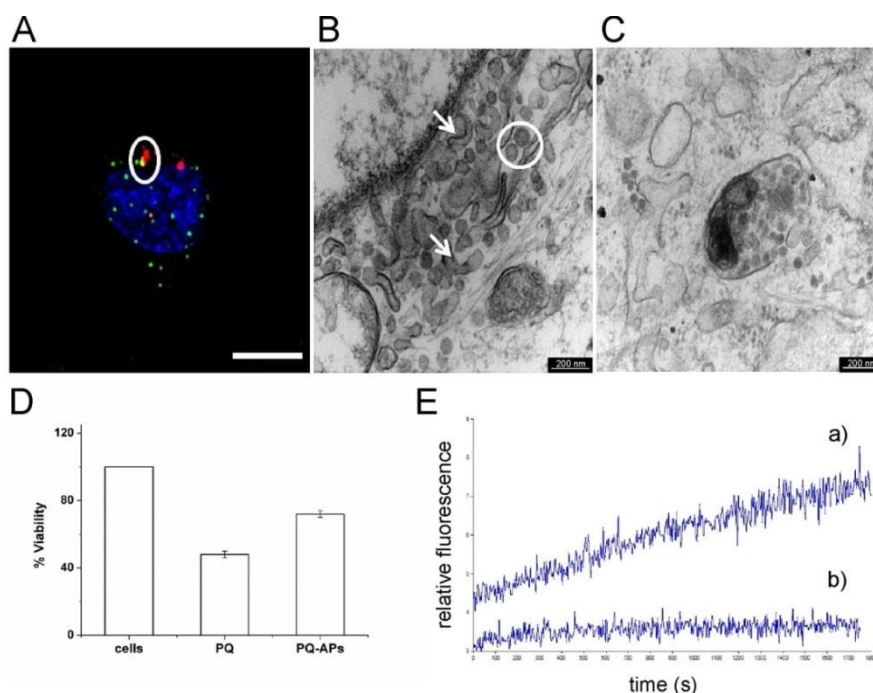


Fig. 34 A) CLSM image of HeLa cells incubated for 24 h with APs (blue: nucleus stained with Hoechst, green: endosome/lysosome stained with pH-rodo, red: artificial peroxisomes) (Scale bar = 5 μ m). B) TEM images of the peri-nuclear region of HeLa cells incubated with APs for 12 h (Scale bar = 200 nm). C) TEM images of endosome-like compartments in HeLa cells incubated with APs for 12 h (Scale bar = 200 nm). D) Protective effect of APs against paraquat by flow cytometry analysis: viability of untreated cells considered as 100%, (cells), viability of cells after treatment with paraquat (PQ) and viability of cells pre-treated with APs for 24 h, and sequentially treated with paraquat for a further 24 h (PQ-APs). E) Real time ROS detoxification kinetics of APs in: a) cells treated with pyocyanin, and b) cells pre-treated with APs (8 h) followed by treatment with pyocyanin. Reprinted with permission from Ref. 78. Copyright 2013 American Chemical Society.

It is noteworthy that similar block copolymer was studied for polymer-lipid interactions to understand interfacial effects of the tri-block copolymer with cell membrane. It has been demonstrated that smaller amounts of the tri-block copolymer system was sufficient to force the lipid membranes to phase separate and form domains.¹⁴⁰ Additionally we have shown in earlier studies that similar tri-block copolymer based polymersomes escape the endosomes in THP-1 cells.⁶² Therefore, it is clear that APs escape the endosomes possibly due to the ability to force the endosomal membrane to phase separate thereby causing endosomal escape.

To assess the APs antioxidant functionality, oxidative injury was induced by paraquat in HeLa cells, known to induce toxicity involving production of ROS.¹⁴⁸ Since ROS serve as important intracellular signalling molecules that affect cell viability, this viability in turn is modulated by the intracellular production of ROS. The viability of the cells was quantified by staining them with propidium iodide (PI), a fluorescent and intercalating agent, and subsequent analysis using flow cytometry. Cells pre-treated with APs provided an around 26% protective effect against the oxidative stress caused by paraquat, although the number of enzymes inside APs was low (Fig. 34D). Indeed, the efficient cascade reaction inside the APs explains that the increased viability corresponds to protective effect exclusively by APs. In order to determine the involvement of APs in the ROS detoxification directly in cells, it is important to be able to monitor ROS generation in intact, living cells. Such detection is difficult due to the low concentration and high reactivity of ROS. The short half-life of the ROS requires an immediate and real time monitoring in the live cells. Live cell analysis of ROS detoxification kinetics of APs was monitored in real time using highly sensitive ROS fluorescent probes. We optimised the concentration of pyocyanin to

stimulate the ROS in cells without causing cell death and cell suspension over a period of 30 min, which shows continuous production of ROS. Stimulated cells treated with APs detoxified the ROS under oxidative stress in live cells (Fig. 34E). As expected, cell populations demonstrate significant heterogeneity in rate of ROS generations upon stimulation to pyocyanin. Thus, individual cells within a population may exhibit different kinetics of ROS production as well as different detoxification kinetics.

2.5. Conclusion

We engineered artificial peroxisomes by the combination of natural occurring antioxidant enzymes with synthetic block copolymers, which form polymersomes, aiding the cellular antioxidant defence mechanism in case of oxidative stress. Similar to nature, these APs contain SOD and LPO or CAT, which detoxifies superoxide radicals *in situ* via hydrogen peroxide to the harmless products water and molecular oxygen. The generation of functional nanoreactors, which are able to be cell uptaken and function as an artificial organelle, represent a milestone in the development of *in vivo* cell implants and will open new frontiers in medical therapy. The main advantage over previous attempts to reduce reactive oxygen species is that the APs are not limited for example in uncontrolled release of enzymes. They carry out the function of a cell organelle permanently. The polymersome properties were optimised by means of high encapsulation efficiency to allow an enhanced cascade reaction and to mimic the morphology and function of a natural peroxisome. Enzymatic activity over time is preserved even longer than in solution, making this hybrid system not only suitable for therapeutic applications but also for technical applications such as biosensors. For the therapy of oxidative stress, we were able to show that the APs escaped in intact form from

endo-lysosomes and were distributed within the cytoplasm, important for proper functioning. In addition, viability measurements revealed that the APs were non-toxic. Concluding the high efficacy of the APs in cells in detoxification of superoxide radicals, the APs are a significant innovation in the treatment of cellular ROS and the repair of disturbed cell functions. This is of particular importance, because disturbed cell functions are mainly responsible in the development of disease such as Parkinson`s disease, arterial sclerosis, cancer and many more.

3. Design of pH-triggered nanoreactors

The design of pH-triggered nanoreactors is based on the encapsulation of environment-sensitive molecules in polymersomes and their remote control via specific and functional ion-channels incorporated in the polymersome membrane. Feasibility of this concept was proven using lipid vesicles encapsulating pyranine (a pH dependent fluorescent molecule) and a channel was formed in the lipid membrane with the ion-channel forming molecule gramicidin A.¹⁴⁹ Because lipid vesicles are very fragile and short-lived, the further goal was to use polymersomes in order to design stable and pH-triggerable nanoreactors.

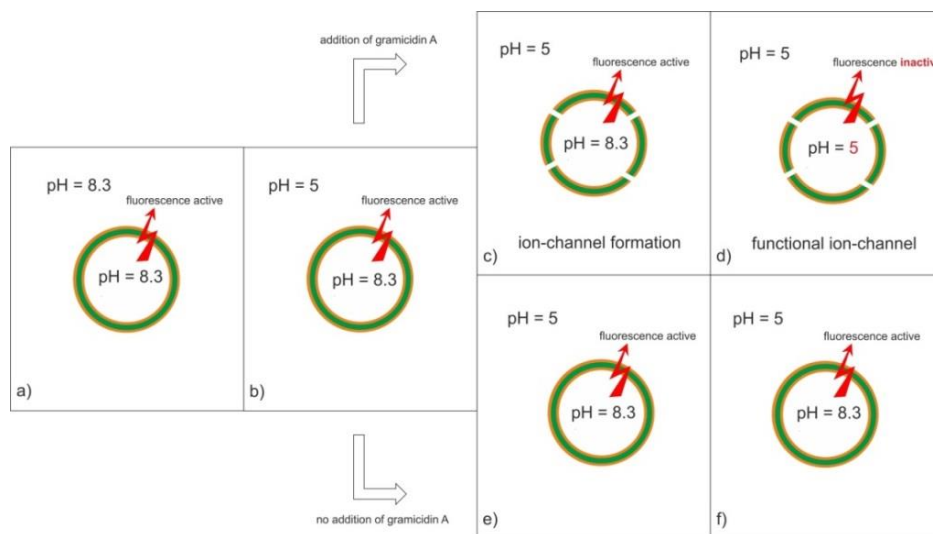


Fig. 35 Procedure to prove functional gramicidin channel formation: a) Pyranine encapsulated vesicles show high fluorescence at pH = 8.3. b) Upon lowering the pH of the vesicle solution to pH = 5, the fluorescence of non-encapsulated pyranine drops immediately. c) Upon addition of gramicidin, functional channel formation lead to a permeabilisation of the vesicles and d) thus to a reduction of fluorescence of the encapsulated pyranine. e) and f) Pyranine encapsulated vesicles preserve their fluorescence activity, when no gramicidin was added.

3.1. Motivation and concept

Specific functions under biological conditions of polymersomes can be induced by external trigger factors, such as pH, light or temperature. This is especially useful for therapeutic applications when unwanted side reactions need to be avoided. A possible strategy to develop responsive nanoreactors is by combining specific pores, such as gramicidin in the membrane of polymersomes. Gramicidin incorporation in liposomes was already reported.¹⁵⁰ The proof of functionality of gramicidin in the membrane was realised by encapsulating a pH-sensitive dye, pyranine, in the aqueous cavity of liposomes. Upon lowering the pH of the liposome solution, the quenching of pyranine molecules was directly monitored. In this case, due to the protective character of the vesicles, encapsulated pyranine molecules were not quenched and still yielded high fluorescence intensity. In the next step, upon addition of the gramicidin ion-channels to the vesicle solution, the pore forming capabilities were proven by direct observation of the quenching of the dye encapsulated in the vesicles. The conceptual steps of functional gramicidin incorporation are illustrated in Fig. 35. After the successful realisation of this technique with liposomes, the same preparation procedure and execution of the experiments were performed using polymersomes.

3.2. Evidence of functional ion-channel incorporation in liposomes

Gramicidin appears in different conformations when dissolved in different solvents¹⁵¹ and not every solvent provides functional pore formation. First a suitable solvent had to be identified, which allows ideal pore formation and would not destroy the vesicles. The different solvents for gramicidin, dimethyl sulphoxide (DMSO), trifluoroethanol (TFE), dioxane, pyridine, isopropanol, decane and the mixtures DMSO:ethanol

(DMSO:EtOH) in the ratio 1:1 and the mixture TFE:DMSO:EtOH (2:1:1) were first tested on lipid pyranine-encapsulated vesicles. Fluorescence spectroscopy results for liposomes were shown in Fig. 36.

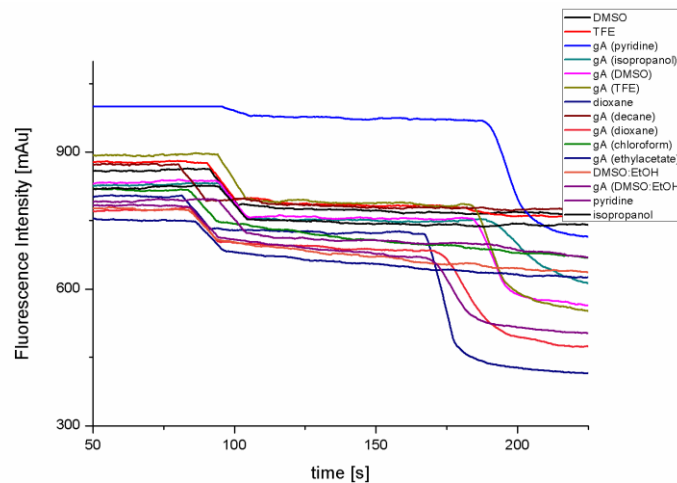


Fig. 36 Fluorescence spectrometry: Time driven fluorescence measurement of the fluorescence emission of pyranine encapsulated in lipid vesicles after lowering pH from 8.3 to 5 (each measurement around time point of 75 s) and subsequent addition of gramicidin (in different solvents) after around 160 s.

As expected (due to the pH dependent fluorescence intensity of pyranine), a decrease in fluorescence intensity occurred after adding HCl solution. Subsequently, gramicidin in different solvents was added. A further decrease of fluorescence intensity in liposomes was only observed, when gramicidin dissolved in DMSO, TFE, pyridine, decane, DMSO:EtOH (1:1), or isopropanol was added after around 160 s to the liposome solution, shown in Fig. 36. This indicates that functional ion-channels were reconstituted in the membrane of the liposomes. In addition, these used solvents were not able *per se* to permeabilise/weaken the liposome membranes, because no change of signal intensity was observed after the treatment with the solvent.

3.3. Evidence of functional ion-channel incorporation in polymersomes

The solvents that allowed gramicidin to build a functional pore into the liposome membrane were then tested with pyranine encapsulated PMOXA₁₄-PDMS₆₅ polymersomes.

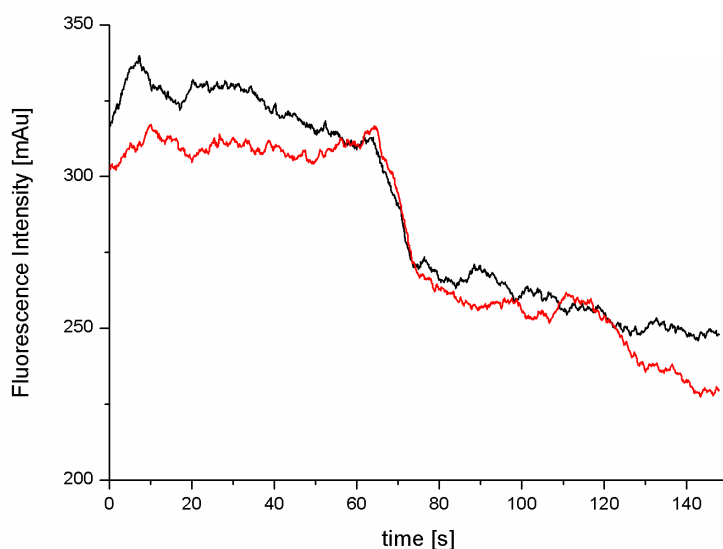


Fig. 37 Fluorescence spectrometry: Time driven fluorescence measurement of the fluorescence emission of pyranine encapsulated in PMOXA₁₄-PDMS₆₅ vesicles after lowering pH from 8.3 to 5 (after 65 s) and subsequent addition of gramicidin (in TFE:DMSO:EtOH (2:1:1)) after 110s. Addition of gramicidin (red); addition of solvent (TFE:DMSO:EtOH (2:1:1)) (black).

HCl was added after 50 s to 80 s and the solvents (with and without gramicidin) were added after 110 s to 130 s. Only gramicidin dissolved in TFE:DMSO:EtOH (2:1:1) added to the vesicles lead to a reduction of fluorescence intensity, without destroying/destabilising the membrane by the solvent alone (Fig. 37). Note that we observed a permeabilisation of the membrane, when solely TFE was used. Interestingly, this behaviour was not observed when liposomes were used.

In order to prove structural integrity of the polymersomes after different steps, preliminary TEM measurements and light scattering experiments were performed before, after lowering pH and after addition of the gramicidin dissolved in TFE:DMSO:EtOH (2:1:1). In the first step, TEM micrographs showed the formation of pyranine-encapsulated polymersomes in pH 8.3 (Fig. 38A). After lowering the pH of the polymersome solution from 8.3 to 5, TEM micrography revealed structural defect vesicles (Fig. 38B).

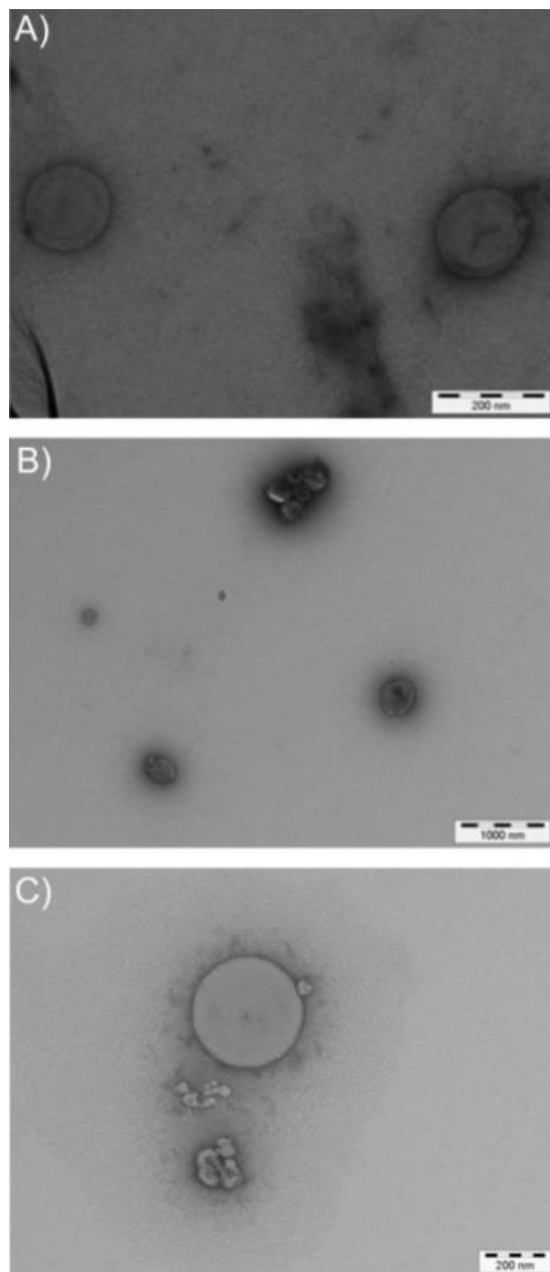


Fig. 38 TEM micrographs of A) AB polymersomes containing pyranine. pH inside and outside of polymersomes = 8.3; B) AB polymersomes containing pyranine. Image was taken after pH of the solution was reduced to pH = 5; C) AB polymersomes containing pyranine. Image was taken after pH was reduced to pH = 5 and subsequent addition of gramicidin.

Considering that the fluorescence intensity during fluorometric experiments did not vanish completely when the pH was lowered, the TEM results suggest that a high proton pressure induced a polymersome collapse during harsh TEM sample preparation. This explanation is further supported by TEM micrographs showing intact polymersomes (Fig. 38C), when the pH of the polymersome solution was decreased, while gramicidin was incorporated into the polymersome membrane. Under these conditions, the high proton gradient induced by the pH change is immediately equalized inside the polymersomes by functional pore formation.

In addition, gramicidin incorporation also shows no membrane destabilisation effects. These results further underline preliminary light scattering experiments (Fig. 39A - C), where the hydrodynamic radii did not change between the different steps of the experimental procedure; i. e. A) non-treated polymersomes, B) measurement after lowering pH, C) measurement after lowering pH and subsequent addition of gramicidin. In this last step, an additional small peak in the size range of 10 nm appeared, which can be contributed to the formation of micelles induced by the solvent of gramicidin.

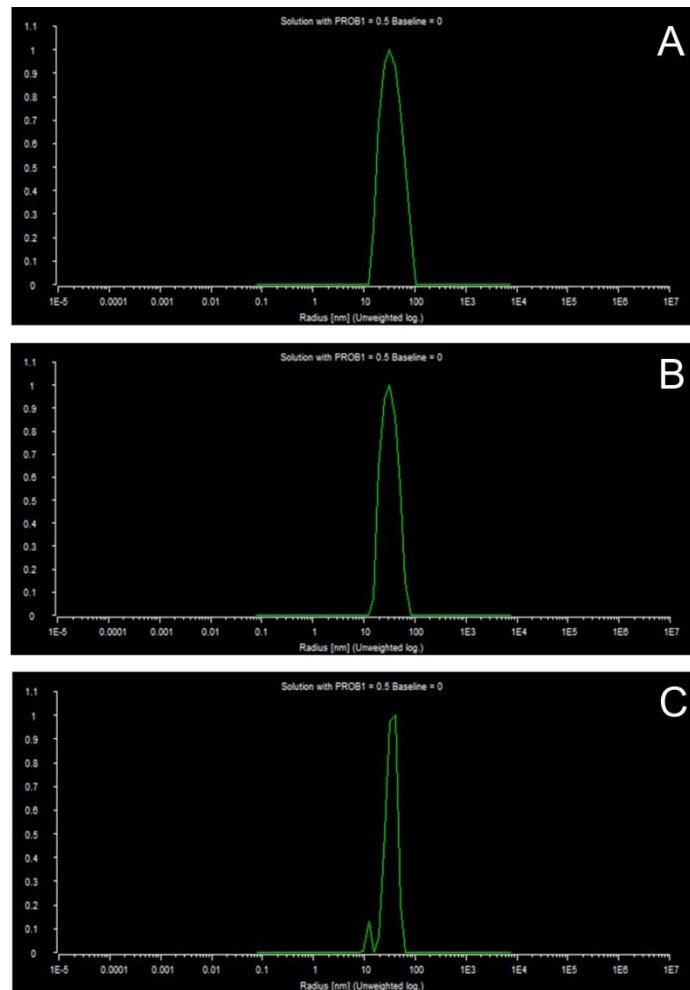


Fig. 39 Preliminary dynamic light scattering experiments of A) AB polymersomes containing pyranine. pH inside and outside of polymersomes = 8.3; B) AB polymersomes containing pyranine after the pH of the solution was reduced to pH = 5; C) AB polymersomes containing pyranine after the pH was reduced to pH = 5 and subsequent addition of gramicidin.

3.3.1. Ion-channel formation (H^+ kinetics) as a function of gramicidin concentration in polymersome membranes

Different gramicidin concentrations were used to study H^+ influx rate as a function of gramicidin concentration in the membrane of

polymersomes. Already at a gramicidin concentration of 65 nM (Fig. 40, red line), H^+ influx can be observed, showing that already a low number of gramicidin is sufficient for proton trafficking. This is in agreement with the high monovalent cation conductance of gramicidin.¹⁵¹ A two-fold increase of the gramicidin concentration to 130 nM showed no significant increase in the H^+ influx rate (Fig. 40, blue line), while at a gramicidin concentration of 32 nM no pore formation was detected (Fig. 40, black line).

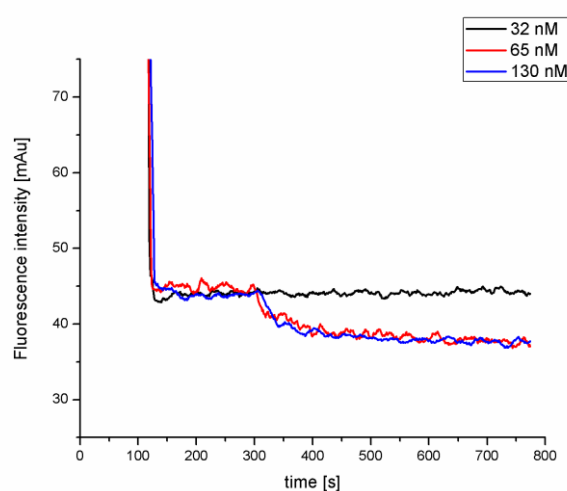


Fig. 40 Fluorescence spectrometry: Time driven fluorescence measurement of the fluorescence emission of pyranine encapsulated in $PMOXA_{14}$ - $PDMS_{65}$ polymersomes after lowering pH from 8.3 to 5 (after 125 s) and subsequent addition of gramicidin (after 300 s) (in TFE:DMSO:EtOH (2:1:1)) at different gramicidin concentrations (dark line: 32 nM; red line: 65 nM; blue line: 130 nM).

3.4. pH-triggered nanoreactors

Gramicidin incorporation in $PMOXA_{14}$ - $PDMS_{65}$ polymersomes forms the basis to engineer pH-triggered nanoreactors, which are composed of a model pH-sensitive enzyme, acid phosphatase. In order to visualise enzymatic activity, a suitable substrate need to be co-encapsulated with

the enzyme. Here the enzyme substrate ELF97 was used, which is converted into a fluorescent product, upon activation of the enzyme (Fig. 41).

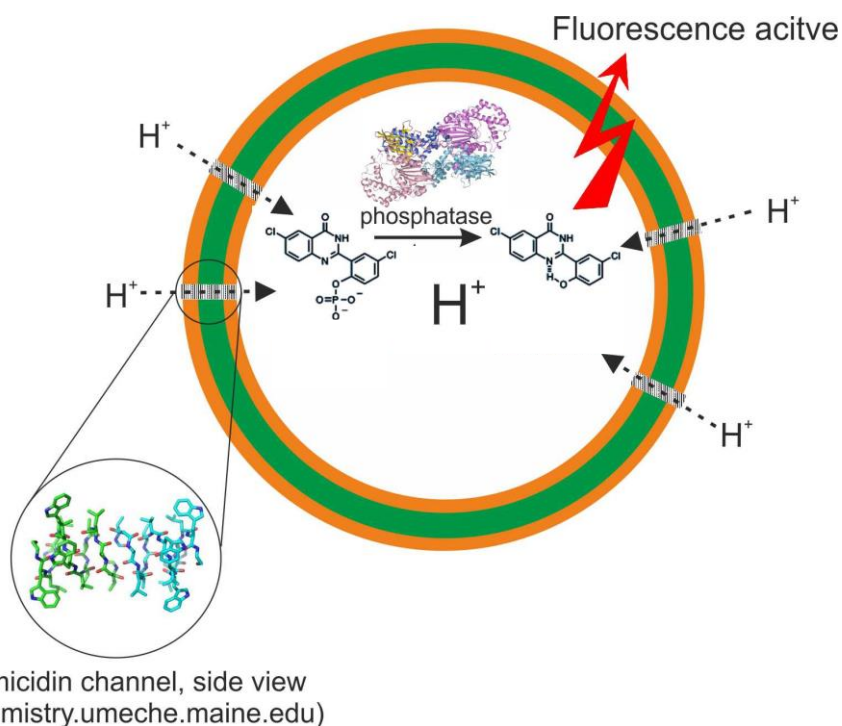


Fig. 41 Schematic view of acid phosphatase and ELF97 co-encapsulated vesicles. Upon lowering pH to around pH = 5 and subsequent addition of gramicidin in order to permeabilise the vesicle membrane, the resulting pH condition inside the vesicle activates acid phosphatase, which produces a fluorescent product from the ELF97 substrate.

In order to prove the concept, acid phosphatase together with ELF97 was co-encapsulated in liposomes. Inside the liposomes, activation of acid phosphatase by a change of pH to either pH 6 (Fig. 42 blue line) or pH 5 (Fig. 42 dark line) led to the formation of fluorescent ELF97 product, when gramicidin formed ion-channels in the vesicle membrane. Under these conditions, the successful lowering of the pH in the vesicles allowed

to activate the enzyme. In contrast, no fluorescent product was formed in absence of gramicidin (Fig. 42 red line).

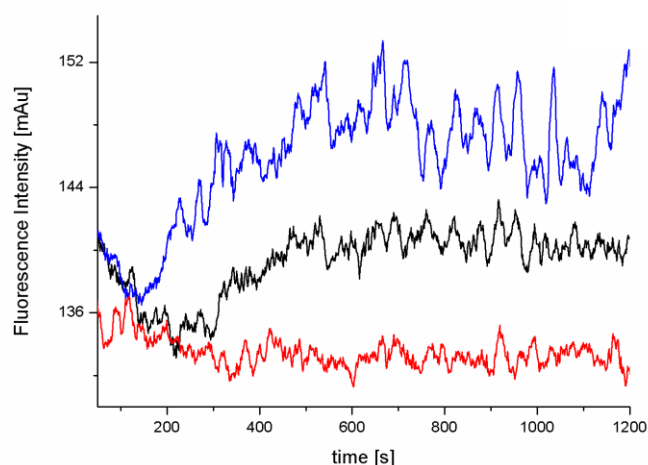


Fig. 42 Time dependent fluorescence emission of ELF97 product encapsulated in acid phosphatase co-encapsulated liposomes: black line) Adjusting pH to around 6 and subsequent addition of gramicidin led to the formation of the fluorescent ELF97 product; red line) Adjusting pH to around 6 in absence of gramicidin did not induce product formation; blue line) Adjusting the pH to 5 and subsequent addition of gramicidin led to an increased formation of the fluorescent ELF97 product.

When the same reaction was performed using vesicles made from PMOXA₁₄-PDMS₆₅ copolymer, no increase of fluorescence was observed. Thus, we were not able to generate pH-sensitive polymer nanoreactors. The reason for this result might be that a low encapsulation efficiency of the enzyme does not allow for simultaneous co-encapsulation of the substrate, necessary to detect the enzymatic functionality. To solve this problem, further optimisation of the individual encapsulation of the enzyme and substrate is needed in order to allow co-encapsulation. Another possibility could be the switch to a new enzyme/substrate

system, which is distinguished with improved properties such as increased encapsulation behaviour and assay sensitivity.

3.5. Conclusion

The diblock copolymer used here formed vesicles in the diameter of approximately 200 nanometres and was able to encapsulate a pH sensitive dye, pyranine. This was used in order to prove the incorporation of gramicidin in the membrane of polymersomes. This achievement is an important step towards the design of pH-triggerable nanoreactor, in order to activate or deactivate the nanoreactor activity upon request via specific ion-channels. Up to now, encapsulation of a pH sensitive enzyme, acid phosphatase, together with its substrate is only possible in case of liposomes generating only a low detection signal. In case of polymersomes, no signal could be generated, indicating no simultaneous co-encapsulation of the enzyme and its substrate. Further investigation to improve encapsulation efficiency of the enzyme and the substrate to achieve pH-sensitive nanoreactor are on-going. It is also considered to exchange the enzymatic system in order to improve the system's performance and thus to engineer functional pH-switchable nanoreactors.

4. Metal-functionalised polymersomes for molecular recognition

The specificity exhibited by molecular recognition assemblies is based on a perfect structural match between biological entities, which results in minimisation of energy, allowing the energy barrier to be by-passed and to fulfil a biological role. The fact that molecular recognition is based on highly selective moieties, their application is discussed in industrial and medical context, such as the purification^{102,103} and immobilisation^{21,23,104,105} of biomolecules, labelling of proteins,^{106,107} 2D-crystallisation^{23,104} and biosensing.^{152,153} Molecular recognition also plays an important role in the development of nanocarriers for drug/protein delivery or nanoreactors due to the potential decrease of dosages and improved localisation in a desired biological compartment. In this respect, these carriers need to be functionalised with a specific affinity tag to enable molecular recognition.

4.1. Motivation and concept

In a molecular recognition process, solvent molecules are specifically replaced by ligands. During this process, a change of geometry can occur at the binding site, which allows specific recognition. Even though the principle is widely applied in technology, the change of geometry and the exact mechanism are in many cases poorly understood.

Here, we characterise in detail the conformation change of the coordination sphere of Cu^{II}-trisNTA centres, which were used to functionalise poly(butadiene)-*b*-poly(ethylene oxide) (PB-*b*-PEO) diblock copolymers. These metal-functionalised block-copolymers are able to form polymersomes in aqueous solution with metal centres exposed at the inner and outer surface (Fig. 43A), while only the outer exposed metal centres were used for binding studies. We used trisNTA (Fig. 43E) for functionalisation, because its binding affinity is higher than NTA (Fig.

43C). His₆-tags with optional labelling can be used to bind to these molecular architectures (Fig. 43D). The use of His₆-tags is regarded to be a simplified model of His₆-proteins, which were used to bind to metal sites of the polymersomes` surface. This simplification of using short His₆-tags allows better understanding of the docking mechanism, which is essential for biological, technical and medical applications. Compared to Ni²⁺ ions, which are used in many NTA-based systems that have an octahedral coordination sphere, different coordination geometries exists for Cu(II).¹⁵⁴ The different arrangements of Cu(II) are induced by its stereochemistry and allows us to use copper as the metal-coordination for His₆-tags and to gain a deep insight into the rearrangement of the metal centre upon binding of a tagged molecule.

The high affinity of different His-tagged proteins to metal-NTA functionalised liposomes and PB-*b*-PEO diblock copolymer polymersomes is widely known.^{21,23,104} Because the dissociation constant of His-tagged proteins is more or less independent of the surface where the metal centre is bound, the local environment of the metal is crucial during the binding process.

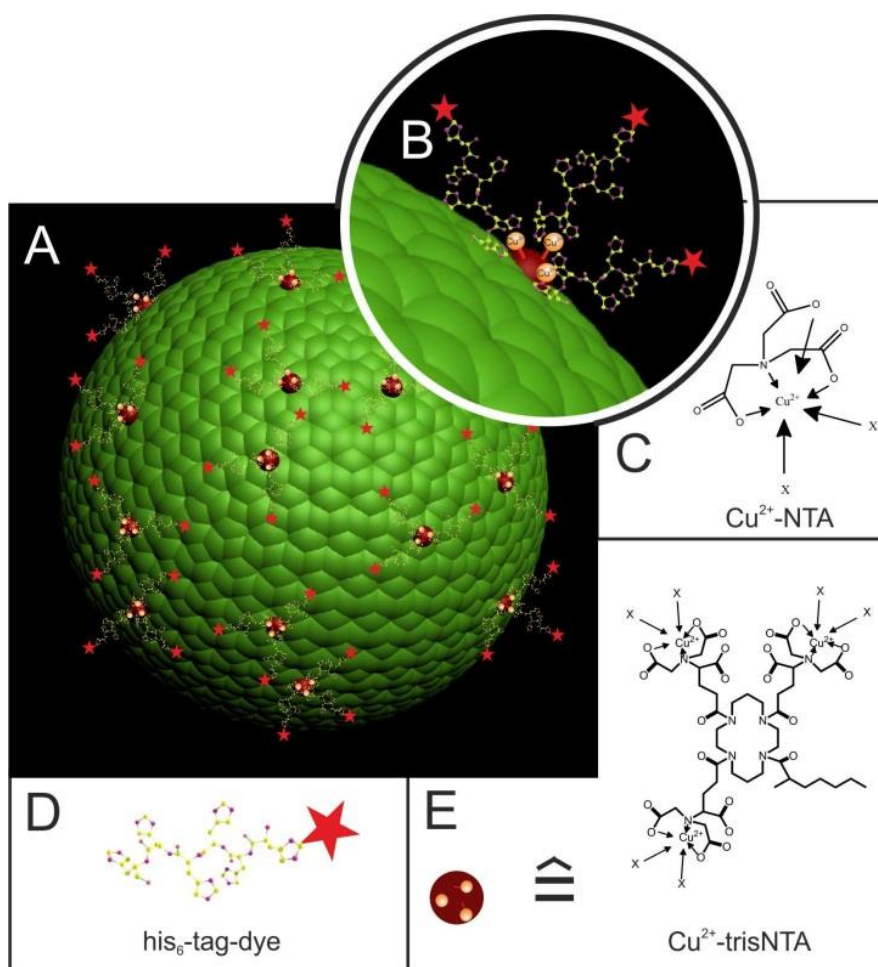


Fig. 43 A) Schematic representation of Cu^{II}-functionalised PB-*b*-PEO vesicles. The metal centres available for binding are located on the outer vesicle surface that can be recognised by fluorescently labelled His₆-tags; B) Detailed view of A); C) Schematic formula of Cu^{II}-NTA complex and D) fluorescently labelled (sulphorhodamine B-His₆-tags; E) Cu^{II}-trisNTA. X represents solvent molecules or external binding atoms of other molecules. The red star represents sulphorhodamine B. Reprinted with permission from Ref. 55. Copyright 2012 American Chemical Society.

4.2. Formation of Cu(II)-trisNTA functionalised polymersomes

Using the diblock copolymer PB₃₉-PEO₃₆-SA-OH-containing 10% PB₃₉-PEO₃₆-SA-trisNTA.d-Cu²⁺ and applying the film rehydration method led to the self-assembly of polymersomes. In order to reduce the polydispersity of polymersome sizes, ranging from giant vesicles to nanovesicles, the sample solutions were extruded through a 1 μm, 400 nm and 200 nm pore-sized filter membrane in descending order. The use of copper instead of nickel has the advantage of studying the copper stereochemistry and to determine the final structural changes in the metal-coordination environment by EPR while a high binding affinity is provided by Cu(II).

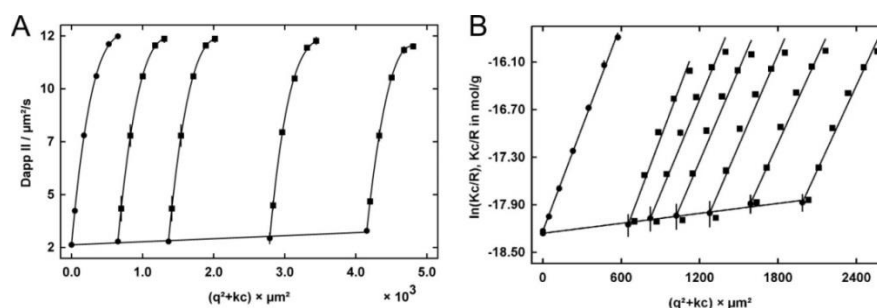


Fig. 44 A) Dynamic light scattering representation. Data extrapolated to zero concentration and zero angle of vesicles made from 10% Cu^{II}-functionalised PB₃₉-PEO₃₆ block copolymer; B) Guinier plot representation of static light scattering data of vesicles made from 10% Cu^{II}-functionalised PB₃₉-PEO₃₆ block copolymer. The data is extrapolated to zero concentration and zero angle. Reprinted with permission from Ref. 55. Copyright 2012 American Chemical Society.

Dynamic light scattering¹⁵⁵ was used to characterise the polymersome hydrodynamic radius to a value of $R_h = 107 \pm 12$ nm (Fig. 44A), comparable to Ni^{II}-functionalised trisNTA-PB-*b*-PEO vesicles.²³ Static light scattering experiments (Fig. 44B) allow to calculate the radius of gyration (R_G) and the ratio of R_G/R_h was determined subsequently as 0.96, which indicates a hollow-sphere morphology.¹⁵⁵

As expected, size and morphology of the polymersomes were not affected by using similar copper concentration compared to nickel inside the NTA moieties.²³ This also indicates that the metal ions are complexed in the NTA pockets of the trisNTA and do not affect the polymer membrane. Further, static light scattering characterisation provided the weight average molecular weight of a vesicle (M_w) to be $8 \times 10^7 \pm 3 \times 10^6$ g mol^{-1} and the second virial coefficient A_2 to be close to zero, ruling out any long-range interactions between the vesicles in the investigated concentration range. In addition, the polymersomes preserved their size and shape over several months at room temperature.

Another characteristic of polymersome formation is the aggregation number, which is obtained by dividing the weight average molecular weight of a vesicle by the weight average molecular weight of the diblock copolymer. The value calculated for this system is 20,000, which is typical for nanometre-sized polymersomes.²⁴

This aggregation number can be used to qualitatively analyse the number of functional metal ions on the outer polymersome surface. There is a 50% probability that the used Cu-trisNTA-functionalised diblock copolymers protrude at the outer surface. Further, it has to be considered that only 10% of polymers used were functionalised, which, in addition, decreases the percentage of active available functional groups. Therefore, based on the assumption that only 10% of block copolymers was rehydrated during the film hydration process, we estimated that a polymersome contains approximately 300 metal ions, which corresponds to 20 copper ions per 100 nm^2 of polymersome surface (nanometre-sized polymersomes).

4.3. His₆-tags binding to Cu^{II}-trisNTA polymersomes

When His₆-tags bound to the nanometre-sized Cu^{II}-trisNTA polymersomes, no change in morphology or structure was observed, demonstrating the high stability after the recognition process (Fig. 45). Also, no aggregate formation was induced upon binding of the tag-molecules, which could affect cellular-uptake behaviour for potential therapeutic applications. This was shown by TEM micrographs of 10% copper-functionalised polymersomes, before and after the addition of His₆-tags (Fig. 45A and B). In both cases, the size of the polymersomes is consistent with the values measured with light scattering. Contrast differences in the TEM micrographs of non-bound Cu-trisNTA-functionalised polymersomes compared to the same polymersomes with attached His₆-tags are likely due to different capillary effects.

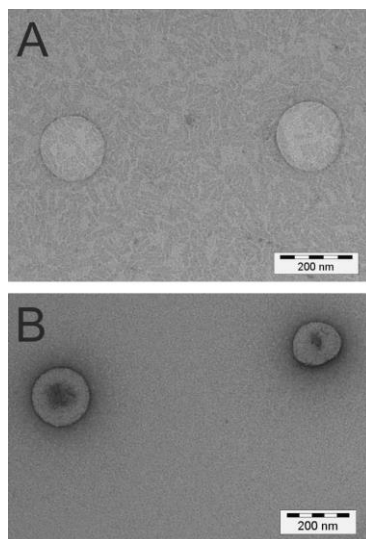


Fig. 45 TEM micrograph of 10% copper-functionalised polymersomes. A) Cu^{II}-trisNTA-functionalised PB-*b*-PEO polymersomes; B) His₆-tag bound to Cu^{II}-trisNTA-functionalised PB-*b*-PEO polymersomes. Reprinted with permission from Ref. 55. Copyright 2012 American Chemical Society.

To visualise His-tag binding with confocal laser-scanning microscopy, we generated giant Cu^{II} -trisNTA-functionalised PB-*b*-PEO polymersomes and incubated them with fluorescently labelled-His₆-tags (s-His₆-tags). To reduce the background fluorescence intensity of the images, non-bound peptide (in a small amount) was removed by dialysis. In the laser-scanning micrographs, polymersomes specifically bound with s-His₆-tags appear as bright fluorescent coronas (Fig. 46A). Because the PB-*b*-PEO polymersome membrane is highly impermeable to small molecules, the fluorescent s-His₆-tags were not able to penetrate the membrane. The hollow vesicular structure of the peptide bound polymersomes could be clearly rendered by the composition of fluorescent z-stack images taken in different layers of the sample (Fig. 46B).

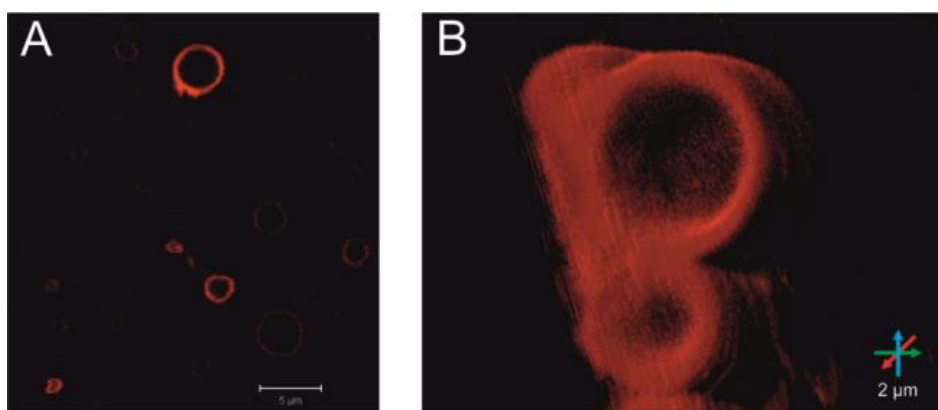


Fig. 46 Confocal fluorescence microscopy image of fluorescently labelled His₆-tags bound to the outer surface of PB₃₉-PEO₃₆-SA-/ 10%-PB₃₉-PEO₃₆-SA-trisNTA.d-Cu²⁺ (800 μM) vesicles incubated with s-His₆-tags in bidistilled water. A) Two-dimensional cut, focused on the mid-plane of the selected vesicles; B) three-dimensional image produced by merging two-dimensional layers measured at different heights. Reprinted with permission from Ref. 55. Copyright 2012 American Chemical Society.

Fluorescence correlation spectroscopy (FCS) is widely used to investigate molecular interactions of fluorescent molecules, such as green fluorescent protein interaction to an antibody.¹⁵⁶ Here, this technique is

used to study the binding of fluorescently labelled His₆-tags to nanometre-sized polymersomes, based on the change of diffusion times, which is different from small molecules (for example fluorescently labelled His₆-tags) compared to big entities, for example nanovesicles. Cu^{II}-functionalised polymersomes (at a concentration of 8 μM) incubated with s-His₆-tags (initial concentration of 50 nM) showed two populations. A small portion (< 5%) of a population with a diffusion time of 56 μs represents free peptides still present in solution. The other population, to a portion of more than 95%, has a characteristic diffusion time of 7.5 ms, which can be attributed to s-His₆-tags bound to vesicles (Fig. 47A).

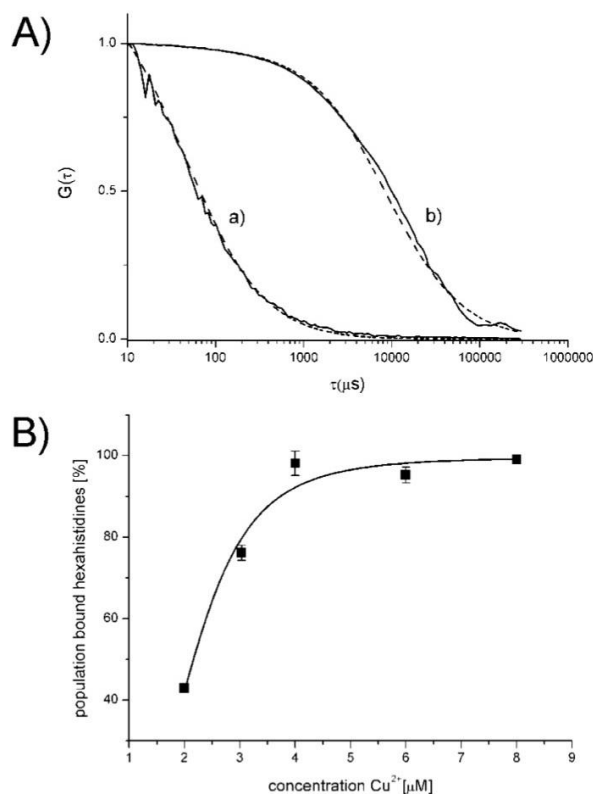


Fig. 47 A) FCS autocorrelation curves and the simulation of a) sulphorhodamine B acid chloride labelled His₆-tags; b) sulphorhodamine B acid chloride labelled His₆-tags bound to vesicles; B) Fraction of bound s-His₆-tags as a function of the Cu^{II} content of PB₃₉-PEO₃₆-SA-OH/ 10%PB₃₉-PEO₃₆-SA-trisNTA-Cu²⁺ vesicles generated in bidistilled water. (Initial concentration of His₆-tag: 50 nM, and initial concentration of Cu-trisNTA functionalised vesicles: 8 μM). Reprinted with permission from Ref. 55. Copyright 2012 American Chemical Society.

Similar experiments of His₆-red fluorescent protein to Ni^{II}-functionalised PB-*b*-PEO polymersomes exhibited a similar binding behaviour, proving that our His₆-tag model system can be used to check binding properties of much larger His-tagged proteins. The small size of the model peptides should also cause less interference with the vesicle surface, which in turn allows faster and stronger binding behaviour.

FCS results are in agreement with the observations from confocal microscopy, where the majority of s-His₆-tags are bound to the metal-functionalised polymersomes (Fig. 47A and B). From the diffusion time obtained by FCS, the hydrodynamic radius R_h can be determined via the Stokes-Einstein equation to be 90 nm – comparable to both values obtained from light scattering and TEM.

The dissociation constant of s-His₆-tags bound to Cu²⁺-functionalised polymersomes was determined by a titration of the s-His₆-tags (50 nM) with increasing amounts of polymersomes (Fig. 47B). The Cu²⁺ of the vesicle was varied from 2 to 8 μM. The corresponding curve was fitted by a Langmuir isotherm^{21,157} (equation 7) and the binding constant was determined.

$$F = \frac{PK_D}{1+PK_D} \quad (7)$$

F corresponds to the corrected fraction of His₆-tags-bound vesicles and P is the metal concentration of the related samples. K stands for the binding constant. A dissociation constant K_D of s-His₆-tags was calculated to a value of 0.6 ± 0.2 μM. In comparison to other K_D of similar systems shown in Table 1, this value is lower, which stands for increased binding.

Table 1 Different K_D -values in polymersomes and liposomes using different His-tagged ligands.

Vesicle system	Ligand	K_D [μM] (FCS-based)	Ref.
PB ₆₀ - <i>b</i> -PEO ₃₄ -SA/PB ₆₀ - <i>b</i> -PEO ₃₄ -SA-NTA.d-Ni ²⁺	His ₆ -EGFP	12.0 ± 0.8	²¹
PB ₃₉ - <i>b</i> -PEO ₃₆ -SA/PB ₃₉ - <i>b</i> -PEO ₃₆ -SA-trisNTA.d-Ni ²⁺	His ₆ -RFP	2.0 ± 0.4	²³
PB ₃₉ - <i>b</i> -PEO ₃₆ -SA/PB ₃₉ - <i>b</i> -PEO ₃₆ -SA-trisNTA.d-Ni ²⁺	His ₁₀ -MBP-FITC	7.0 ± 1.2	²¹
PB ₃₉ - <i>b</i> -PEO ₃₆ -SA/PB ₃₉ - <i>b</i> -PEO ₃₆ -SA-trisNTA.d-Ni ²⁺	His ₆ -EGFP	12.3 ± 1.2	²¹
Ni ²⁺ -NTA-NBD-lipid	His ₆ -peptide	4.3 ± 0.8	¹⁵⁷
PB ₃₉ - <i>b</i> -PEO ₃₆ -SA/PB ₃₉ - <i>b</i> -PEO ₃₆ -SA-trisNTA.d-Cu ²⁺	His ₆ -tag	0.6 ± 0.2	this work

In Table 1, nickel-functionalised vesicles were used for protein binding for comparison with our copper-functionalised systems. It was shown by molecular dynamics simulations that Ni^{II} and Cu^{II} have a similar affinity towards a His₆-tag.¹²⁰ Nevertheless it was shown that copper binds His-tags more strongly than nickel, providing a high binding capacity, but a poorer specificity.

Comparing the His₆-tags binding of our copper-functionalised polymersomes with His₆-RFP binding to PB₃₉-PEO₃₆-trisNTA.d-Ni²⁺ vesicles, a much greater binding affinity can be stated. We assume that in addition to the different binding affinity as explained before, the small peptide molecules interfere less with the flexible PEO chains at the polymersome surface, so that improved binding conditions were provided. Polymersomes containing no metal-functionalised block copolymers showed less than 3% His₆-tag binding measured under the same conditions. This low unspecific binding of the His₆-tag is in agreement with the protein repellent character of PEO chains at the vesicle surface.²² Also non-functionalised vesicles did not bound s-His-tags after addition of Cu(OTf)₂, clearly defining that copper complexed in the NTA pocket is the recognition point of His-tag proteins.

FCS can be also used to quantify the number of bound s-His₆-tag per polymersome by performing brightness measurements. The molecular brightness of peptide-bound polymersomes recorded as counts per molecule (CPM) must be divided by the CPM of freely diffusing s-His₆-tags, taking the fluorescence quantum yield into account. This calculation resulted on average in 210 ± 36 molecules per polymersome. Compared to the value of reported His₆-RFP binding to vesicles, s-His₆-tags bound an order of magnitude higher to the polymersomes of similar nature.

When the small size of the used labelled His₆-tags compared to the size of a fluorescent protein is considered, we can hypothesise that more metal-trisNTA moieties can be more easily occupied with small peptides, which explains the small K_D value (Fig. 43A and B). Furthermore, the calculated number of His₆-tags per polymersomes is in agreement with the available metal ions/polymersomes calculated from the aggregation number determined by light scattering.

4.4. Structure of the coordination sphere of Cu^{II} in His₆-tag-Cu^{II}-trisNTA polymersomes in comparison to model systems

In order to gain more insight inside the coordination sphere of Cu(II) before and after the binding process of the His-tag molecules, electron paramagnetic resonance spectroscopy (EPR) was applied. EPR can be used to characterise structural information of paramagnetic species, e. g. transition metals or radicals. The observed X-band CW-EPR spectrum of polymersomes (Fig. 48a) produces only a broad signal with a low intensity, which can be ascribed to a high local copper concentration coming from the high number of metal ions per polymersome as calculated from light scattering data. In this case, the resulting strong dipolar interactions of the Cu^{II} centres are potentially responsible of broadening of the EPR spectrum to the detection limit. On the other hand, EPR measurements of Cu^{II}-functionalised PB₃₉-PEO₃₆-SA-trisNTA.d.²¹ provided clear spectra. The CW-EPR spectrum of the functionalised polymersomes (Fig. 48a) is different from the simulated spectrum, where the reported EPR parameters of the latter building blocks were used for the polymersomes (Fig. 48b). Because the spectrum in polymersomes (Fig. 48a) exhibits spectral features, which were characteristic of strong dipolar interactions between Cu^{II} sites, it cannot be simulated using a single species.

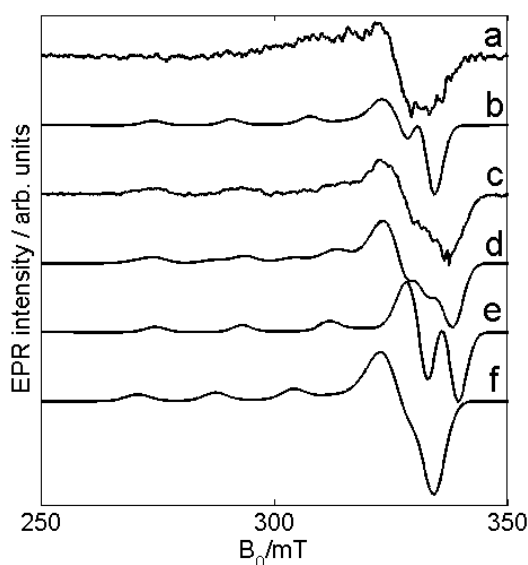


Fig. 48 (a) X-band CW-EPR spectrum of a frozen solution of Cu^{II} -trisNTA functionalised vesicles in bidistilled water taken at 100 K. (b) Simulation of the CW-EPR spectrum of the $\text{PB}_{39}\text{-PEO}_{36}\text{-SA-trisNTA}$.d using the parameters reported in Ref. ²⁰. (c) Experimental X-band CW-EPR spectrum of a frozen solution of Cu^{II} -trisNTA functionalised vesicles incubated with the His_6 -peptide in a 1:50 ratio taken at 10 K. (d) Simulation of (c) using the parameters in Table 1. (e) and (f) individual contributions to the simulation (d). All presented spectra are normalised for clarity. The spectral intensity of (a) is more than a factor 10 lower than that of (c). Reprinted with permission from Ref. 55. Copyright 2012 American Chemical Society.

When we incubated the polymersomes with $\text{His}_6\text{-RFP}$, $\text{His}_6\text{-EGFP}$ or with His_6 -tags, only the addition of His_6 -tags, at an initial concentration of 2 mM, led to a change in the EPR spectra compared to the non-bound condition, observable in an increased CW-EPR signal. This behaviour is caused by the lower concentration of His_6 -proteins used, which is limited by their commercial availability and the function of the peptide to act as a spacer between the different Cu^{II} sites. In Fig. 48c, the X-band CW-EPR spectrum together with its simulation (Fig. 48d) of His_6 -peptide incubated polymersomes is shown. Two contributions can be discerned (EPR

parameters are given in Table 2), although the signal is poorly resolved. The EPR parameters are typical of type II copper centres.¹⁵⁸ The vesicle:His₆ system is in agreement with the situation where Cu^{II} is equatorially ligated either to four oxygen atoms (4O) or to one nitrogen and three oxygen atoms (1N3O) as the first EPR parameters. The second types imply that either two nitrogen atoms and two oxygen atoms (2N2O), three nitrogen atoms and one oxygen atom (3N1O), or four nitrogen atoms (4N) are coordinated with Cu^{II}, whereas the last set supports histidine binding. In this case, high values for the z-component of the copper hyperfine have been reported.¹⁵⁹⁻¹⁶³ The third contribution caused by the copper sites located on the inner vesicle surface will be present at considerably lower intensity, which is in agreement with the spectrum in Fig. 48a.

Different model systems have been studied to interpret the above findings: a) a mixture of Cu-triflate (Cu(OTf)₂) with NTA, b) a mixture of Cu(OTf)₂ with His₆-peptide and c) a mixture of Cu(OTf)₂ with His₆-tags and NTA. The obtained EPR parameters are presented in Table 2. It is evident that the His₆-tags cannot bind to free Cu^{II} ions under the given conditions. This possibility was excluded by the fact that the spectral changes did not occur (Fig. 48), when peptide was added to non-functionalised vesicles containing free Cu^{II} ions in the solution. Moreover, EPR experiments made with different mixtures of Cu(OTf)₂, NTA and the His₆-peptide showed that both NTA and the peptide ligate to the Cu(II) ion. Also, it became obvious that more Cu^{II} centres are linked with increasing His₆-tag concentration.

Table 2 Principal g and copper hyperfine values of Cu^{II} -trisNTA functionalised polymersomes compared with different model systems. The hyperfine values are given for the ^{63}Cu nucleus.

	g_x, g_y	g_z	$ A_x , A_y /\text{MHz}$	$ A_z /\text{MHz}$
Cu^{II} vesicles with His_6	2.035 (\pm 0.004)	2.230 (\pm 0.001)	5 (\pm 20)	570 (\pm 1)
	2.066 (\pm 0.005)	2.215 (\pm 0.001)	5 (\pm 20)	590 (\pm 2)
$\text{Cu}(\text{OTf})_2:\text{NTA}$ (1:5)	2.061 (\pm 0.005)	2.302 (\pm 0.001)	45 (\pm 20)	512 (\pm 2)
$\text{Cu}(\text{OTf})_2:\text{His}_6$ (1:5)	2.074 (\pm 0.005)	2.375 (\pm 0.001)	21 (\pm 20)	450 (\pm 2)
$\text{Cu}(\text{OTf})_2:\text{NTA}:\text{His}_6$ (1:5:5)	2.058 (\pm 0.005)	2.282 (\pm 0.001)	10 (\pm 20)	510 (\pm 2)
$\text{PB}_{39}\text{PEO}_{36}\text{-SA-trisNTA.d}$	2.052	2.253	91	517
$\text{Cu}(\text{His})$ solution at pH 7.3 (Ref. 162)	2.058	2.24	37	561
$\text{Cu}(\text{His})$ solution at pH 3.8 (Ref. 159)	2.06	2.31	-	507

A hexacoordination of the metal site is typically assumed (Fig. 43C) for aqueous transition-metal complexes of NTA, which involves the ligation of three carboxyl groups, an amine group and two water molecules. Although no structural data are available, a similar binding mode is proposed for the interaction between a polyhistidine tag and metal-NTA chelates. The crystal structure of a bisimidazole complexed to Cu^{II} and NTA shows a five-coordinate square pyramidal structure, with one protonated carboxyl group, two imidazoles and two carboxy groups of NTA equatorially ligated, and a weak axial coordination of the NTA amine group.²³ Therefore pulsed EPR experiments were performed to verify this structure. The low-frequency area of the HYSORE spectrum of a $\text{Cu}(\text{OTf})_2:\text{NTA}$ (1:5) mixture exhibits no cross peaks from a weakly coupled ^{14}N nucleus as expected when amine nitrogen atoms binds axially to copper. The Mims ENDOR spectra (Fig. 49) and the ^1H HYSORE spectra, taken at different magnetic field positions, show maximum ^1H hyperfine couplings of 7 to 9 MHz.

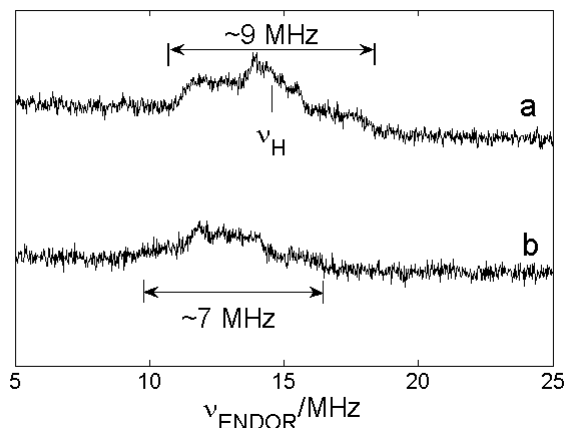


Fig. 49 Mims-ENDOR of $\text{Cu}(\text{OTf})_2\text{:NTA}$ mixture of 1:5 ratio in frozen water solution recorded (a) at $B_0 = 344.8$ mT (observer position corresponding to $g \approx g_{x,y}$), and (b) at $B_0 = 303.0$ mT (observer position corresponding to $g = g_z$, $\text{MI} = -1/2$). Reprinted with permission from Ref. 55. Copyright 2012 American Chemical Society.

This is in accordance with the findings for $[\text{Cu}(\text{H}_2\text{O})_6]^{2+}$ in frozen water¹⁶⁴ and in $\text{Mg}(\text{NH}_4)_2(\text{SO}_4)_4 \cdot 6\text{H}_2\text{O}$ crystals¹⁶⁵ and corroborate with the equatorial water ligation in the Cu^{II} -NTA complex. The large proton coupling is not likely to be caused by the NTA protons, as their far distance from the copper site would result in smaller hyperfine couplings. Davies ENDOR spectroscopy was used to probe the interactions with directly coordinated nitrogen atoms. A value of ~ 25 MHz for the z -component of the hyperfine interaction of the amine nitrogen was obtained, confirming an equatorial ligation of this amine.

A low-frequency HYSCORE spectrum was obtained by adding His_6 -tags to a $\text{Cu}(\text{OTf})_2\text{:NTA}$ mixture, which shows contributions of a weakly coupled ^{14}N nucleus (Fig. 50A) simulated by using the data in Table 3 (Fig. 50B). The obtained parameters resemble the reported values for the remote imidazole nitrogen in Cu^{II} -bound imidazole complexes¹⁶⁶ and Cu^{II} -bound histidine complexes.^{159,161,167,168} This underlines the His_6 -

peptides binding, seen in CW-EPR measurements. Furthermore, the Mims ENDOR and HYSCORE spectra indicate a maximum proton coupling of 5.8 MHz (Fig. 51). This corresponds to the known proton hyperfine coupling value for the H ϵ proton of an equatorially ligated histidine imidazole to be max. 5.4 MHz.¹⁶² Therefore, the water, equatorially ligated to copper centre, is substituted with His residues.

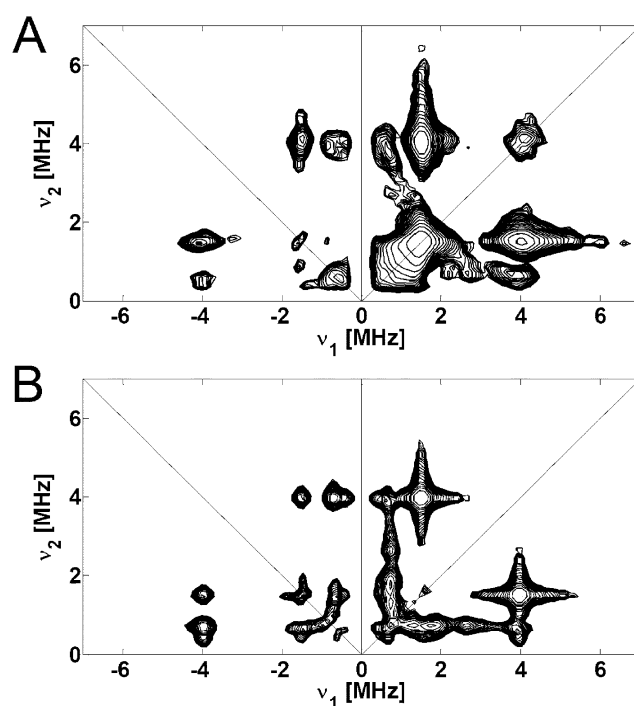


Fig. 50 A) X-band HYSCORE spectrum of a frozen solution of $\text{Cu}(\text{OTf})_2$:NTA:His₆-peptide mixture at a 1:5:50 ratio taken at 5 K; B) Simulation of A) using the parameters from Table 3. The observer position is 335.0 mT, $\tau = 104$ ns. Reprinted with permission from Ref. 55. Copyright 2012 American Chemical Society.

Table 3 Comparison between the experimental ^{14}N spin Hamiltonian parameters derived from the HYSCORE spectra for His₆-tag ligation and the Cu^{II}-NTA functionalised vesicles and the Cu^{II}-NTA complexes.

	A/MHz	$e^2qQ/h/\text{MHz}$	h
Cu ^{II} vesicles with His ₆	$\pm 1.9 (\pm 0.3)$	$\pm 1.5 (\pm 0.1)$	$0.95 (\pm 0.10)$
Cu(OTf) ₂ :NTA:His ₆ (1:5:50)	$\pm 1.7 (\pm 0.3)$	$\pm 1.5 (\pm 0.1)$	$0.90 (\pm 0.10)$
Cu(His) (Ref. 107)	1.4	-1.43	0.95

The pulsed EPR analysis described here allowed to assess the effect of His₆-tag addition to Cu^{II}-NTA functionalised polymersomes. Only a weak spin echo signal of a frozen solution containing the polymersomes without peptide was obtained and no pulsed EPR experiments could be performed in agreement with the CW-EPR spectrum (Fig. 48a).

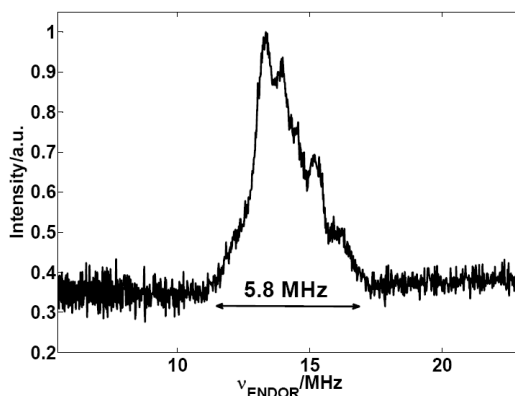


Fig. 51 ^1H Mims-ENDOR spectrum of a frozen solution of Cu(OTf)₂ with NTA and His₆-peptide mixture taken at 5 K at the field position $B_0 = 334.0$ mT, $\tau = 120$ ns. A maximum ^1H hyperfine coupling of 5.8 MHz is observed. Reprinted with permission from Ref. 55. Copyright 2012 American Chemical Society.

After the addition of the His₆-peptide, the echo intensity improved, which could be explained by the peptide acting as a spacer between the Cu^{II} sites on the polymersome surface, thereby reducing the dipolar

interaction between these sites. Nevertheless, a low echo intensity was still observed so that ESEEM or ENDOR experiments could only be performed at the position of highest echo intensity (corresponding to the observer position $g = g_{x,y}$). This is shown in the ^{14}N HYSCORE spectrum (Fig. 52A) with its corresponding simulation (Fig. 52B) using the given data in Table 3. The data confirms a binding of the His₆-tags to the copper site, as the parameters match with data, which is expected for the remote nitrogen of a His ligand. In addition, Mims-ENDOR experiments arrived to the same conclusion and are against an equatorial H₂O ligation.

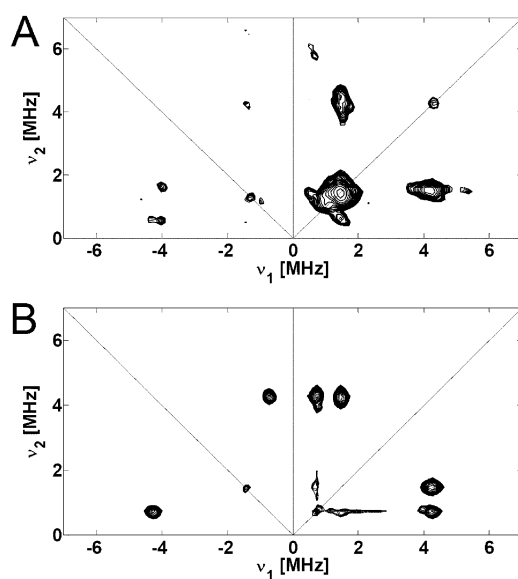


Fig. 52 A) X-band HYSCORE spectrum of a frozen solution of Cu^{II}-NTA-functionalised vesicles with His₆-peptide at a 1:50 ratio taken at 5 K; B) Simulation of a) using the parameters from Table 3. The observer position is 338.8 mT, $\tau = 120$ ns. Reprinted with permission from Ref. 55. Copyright 2012 American Chemical Society.

Combining all data, EPR analysis of the aqueous Cu^{II}-NTA- and the Cu^{II}-NTA-His₆ complexes clearly shows the existence of type-II copper complexes. Pulsed EPR and ENDOR data clarified that the copper ion is

equatorially bound to at least one water molecule and to the NTA amine nitrogen. This is different from the observation of the X-ray structure of copper(II)-nitrilotriacetic acid-bis(N-methylimidazol-2-yl)ketone ternary complexes where the NTA amine is in an axial position.¹⁶⁹ In this case, it is reasonable that a flat bis-imidazole complex may be the cause of this different configuration.

Upon addition of His₆-tags to copper-trisNTA functionalised polymersomes, the equatorial water is replaced by His residues, as clearly shown by HYSCORE and ENDOR data. This is further corroborated by pulsed EPR data, which confirms an equatorial ligation of the imidazole(s) of His₆-tags attached to the Cu^{II}-NTA moieties on the surface of polymeric vesicles.

Incubation of His₆-tags to the polymersomes provoked the formation of two different type-II copper sites (Table 2) as established from CW-EPR. Their principal *g* and copper hyperfine values significantly differ from those observed for the Cu(OTf)₂:NTA:His₆-peptide mixture. This could suggest that the surrounding structure influenced the local copper complex structure. Hence, the *g_z* value of Cu^{II}-PB₃₉-PEO₃₆-SA-trisNTA.d is also lower than that observed for the aqueous copper NTA complex. The EPR parameters of the vesicle/His₆-tag mixture resemble the values obtained for copper histidine complexes at neutral pH,¹⁶² while the parameters of the Cu(OTf)₂:NTA:His₆-peptide mixture were comparable to those of the copper-histidine complexes at pH 3.82.¹⁰² The copper-histidine ligation difference at different pH values originates from the number of His residues and corresponding amine groups ligating to the copper centre.

DFT computations complemented these observations. While it is known that DFT cannot exactly reproduce EPR parameters of transition-metal complexes in means of underestimated *g* values and dissatisfying

transition-metal hyperfine values yet, the computations can be still used to estimate general trends and hyperfine values of the ligand nuclei.¹⁷⁰ Therefore, the EPR parameters of three models were computed using DFT (Fig. 53A, B and C). The effect of the exchange of water by His residues was simulated and the impact of the overall charge of the complex on the EPR parameters was evaluated. In model A, one NTA and two water molecules are ligated to the copper site, while models B and C includes the ligation of one NTA and a bis-imidazole molecule with a peptide-like linker. While in model C all carboxy groups are deprotonated, models A and B have one protonated carboxy group. All structures were optimised in terms of their overall lowest energy state via geometry optimisation using different starting geometries. The corresponding coordinates of the models are given in the Appendix. The DFT results are presented in Table 4 and the corresponding spin density distributions (Fig. 54 – Fig. 56) are shown in the Appendix. The computed parameters of models A and B reproduce different experimentally observed trends: Both typically have a quasi-axial g tensor, characteristic of type-II complexes with the copper in a $d_{x^2-y^2}$ ground state. The computations confirm for model A, the aqueous Cu^{II} -NTA model, the experimental observation of the NTA amine nitrogen located in the equatorial plane (i.e. plane determined by $d_{x^2-y^2}$) located NTA amine nitrogen and bearing a considerable amount of spin density. The computed z -component of this hyperfine interaction (27 MHz) resembles to the experimental value (25 MHz). Also, the computed maximum hyperfine interactions (absolute value) of equatorially ligated water protons (10.7 MHz) is in the same order of magnitude as the experimental values (9 MHz).

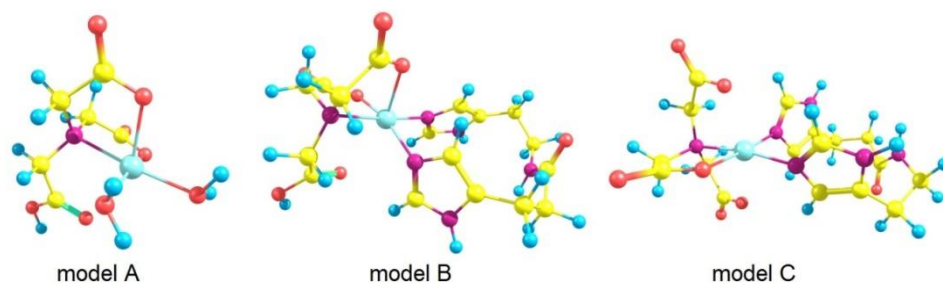


Fig. 53 DFT-optimised structures of the three models. **Model A:** $[\text{Cu}(\text{N}(\text{CH}_2\text{COO})_2(\text{CH}_2\text{COOH}))(\text{H}_2\text{O})_2]$; **Model B:** $[\text{Cu}(\text{N}(\text{CH}_2\text{COO})_2(\text{CH}_2\text{COOH}))(\text{C}_{11}\text{H}_{15}\text{N}_5\text{O})]$; **Model C:** $[\text{Cu}(\text{N}(\text{CH}_2\text{COO})_3)(\text{C}_{11}\text{H}_{15}\text{N}_5\text{O})]$. Reprinted with permission from Ref. 55. Copyright 2012 American Chemical Society.

Following the experimental trend of computed maximum proton hyperfine couplings, the value for model B (His residues) are smaller (6.4 MHz). Indeed, the hyperfine values of the remote nitrogen atoms are around 1.5 – 2.2 MHz. In agreement to the experimental results, g_z decreases upon attachment of the His residues and the copper $|A_z|$ values are similar for both models A and B. To conclude, these results agree with the experimental trends and confirm the EPR parameters, which indicates that addition of His₆-tags to Cu(OTf)₂:NTA is entirely due to the replacement of the equatorial water by His residues.

In a next step, protonation effects of the NTA carboxyl groups are studied by comparing model B (one protonated carboxyl group) and model C (no protonation of the carboxyl groups). Deprotonation of the third carboxyl group caused an increase of the g_z value and the g tensor to become rhombic. The copper $|A_z|$ value and the NTA amine nitrogen hyperfine coupling are reduced considerably, while the rest of the ligand hyperfine values are less affected ranging in the order of the experimental errors. Thus protonation could play a role in the different EPR parameters of the Cu(OTf)₂-NTA-His₆ mixture and the polymersome-His₆ systems.

Similar hyperfine values were found in both systems for the protons and the remote nitrogens of the His residues, which were also computed for both models B and C. Lower g_z (higher $|A_z|$ values) were seen for the polymersome system compared to the $\text{Cu}(\text{OTf})_2\text{-NTA-His}_6$ mixture. Additionally, the copper $|A_z|$ values differ more between the two His_6 -ligated systems than between $\text{Cu}(\text{OTf})_2\text{-NTA}$ and $\text{Cu}(\text{OTf})_2\text{-NTA-His}_6$. A similar trend is also observed for a higher copper $|A_z|$ value difference between models B and C compared to models A and B. These results suggest that the NTA carboxy groups on the polymersome system are protonated, probably induced by polymersome surface properties. The presence of two different copper complexes in the polymersome system could result from changes in the number or orientation of the His ligands.

Table 4 Computed principal g and hyperfine values for models A-C (Fig. 53).

		g_x	g_y	g_z
Model A		2.067	2.075	2.210
Model B		2.059	2.061	2.193
Model C		2.038	2.099	2.202
	nucleus	A_x [MHz]	A_y [MHz]	A_z [MHz]
Model A	Cu	69	77	-522
	N(NTA)	27	45	27
	H (H ₂ O) ^a	-10.8	6.2	-5.4
Model B	Cu	49	76	-533
	N(NTA)	27	41	27
	N1(His) ^b	44	36	35
	N2(His) ^c	1.7	2.3	1.6
	H (His) ^a	6.4	-0.4	0.1
Model C	Cu	173	-3	-495
	N(NTA)	20	33	20
	N1(His) ^b	42	34	33
	N2(His) ^c	1.6	2.2	1.6
	H (His) ^a	5.9	-0.3	0.2

^aData for the proton with the largest hyperfine coupling (in absolute value), ^bAverage of computed hyperfine values of copper bound His nitrogens; ^cAverage of computed hyperfine values for remote His nitrogen atoms.

4.5. Conclusion

The Cu^{II}-trisNTA-functionalised PB-*b*-PEO polymersomes are well suited to study molecular recognition process of peptide binding. As peptides, we used a model system of an oligohistidine sequence consisting of six histidines – a His₆-tag – to study their binding to copper centres on the polymersome surface. Upon binding, a detailed structural view of the rearrangement of the metal coordination sphere was obtained. Qualitative binding analysis revealed that more than 200 fluorescently labelled His₆-tags were bound to one polymersome. This was visualised by fluorescence laser-scanning microscopy as a highly intense fluorescent corona surrounding the metal-functionalised polymersomes. FCS measurements revealed that this system has a high binding affinity, which was found to be higher than of similar systems using His-tagged

proteins.^{21,23} Different EPR and ENDOR methods were used to investigate the electronic and geometric change of the copper centre complexed in the NTA pocket upon binding of the model His₆-tags. His₆-tag binding was demonstrated via the typical HYSCORE signature of the remote nitrogen of the imidazole ligand of the residue, and by the reduction of the proton hyperfine coupling using EPR and DFT data from model systems. As expected from other experiments, these findings confirmed the strong and selective binding. The highly specific binding capacity of the copper-functionalised PB-*b*-PEO polymersomes together with a simple preparation procedure and inherent high structural stability make the system very suited for a wide range of applications such as protein crystallisation, targeting approaches or immobilisation on solid supports.

5. Overall conclusion

We designed and developed protein-polymer assemblies to engineer artificial organelles. The development required to study three key aspects in order to increase the overall efficacy of the artificial organelles: i) increased efficacy by means of optimised building blocks, ii) introduction of specific membrane permeability by the use of selective ion-channels and iii) applying specific recognition points by the use of a molecular recognition strategy:

i) Combination of natural occurring antioxidant enzymes with synthetic block copolymers, which are able to self-assemble into polymersomes, allowed engineering of artificial peroxisomes (APs). They can support natural peroxisomes and help the cellular antioxidant defence mechanism in general to combat oxidative stress. As active compounds, SOD and LPO or CAT were used in complex, optimised conditions, which detoxify in tandem superoxide radicals *in situ* via hydrogen peroxide to harmless products. These APs were able to be taken up by cells and function as specific artificial organelles, opening a new direction in medical therapy. The polymersome properties were optimised by means of high encapsulation efficiency in order to allow enhanced cascade reactions and to mimic the morphology and functions of natural peroxisomes. Enzymatic activity is preserved over time even longer than in solution, making this hybrid system not only suitable for therapeutic applications, but also for technical applications such as biosensors. For the therapy of oxidative stress, we were able to show that the APs escaped intact from endo-lysosomes and were distributed within the cytoplasm, which is important for properly functioning. In addition, viability measurements revealed that the APs were non-toxic.

ii) In order to address the polymersome membrane permeability in more detail, in addition to the incorporation of OmpF in triblock copolymer

vesicles, diblock copolymer vesicles of 200 nanometres in diameter were produced to encapsulate a pH sensitive dye, pyranine. This system was used in order to prove the membrane incorporation of gramicidin. The successful accomplishment of the ion-channel incorporation is an important step towards the design of pH-triggerable nanoreactors and artificial organelles, where the activity of the protected active compounds can be activated or deactivated via specific ion-channels “on demand”.

iii) Next to the controlled activity, the site specific action of the active compound is also important. To address this challenge, Cu^{II}-trisNTA-functionalised PB-*b*-PEO polymersomes were used to study molecular recognition process of specific peptide binding. A model system of an oligohistidine sequence consisting of six histidines – a His₆-tag – was used to study their binding to copper centres on the polymersome surface. Upon binding, a detailed structural view of the rearrangement of the metal coordination sphere was obtained. More than 200 fluorescently labelled His₆-tags were bound to one polymersome, proving efficient binding. The system was also characterised by a high binding affinity. Different EPR and ENDOR methods were used to investigate the electronic and geometric change of the copper centre complexed in the NTA pocket upon binding of the model His₆-tags. These experiments, as well as DFT computations, confirmed strong and specific binding. This detailed knowledge about the molecular recognition behaviour of the system and the simple preparation procedure allows to further engineer specific artificial organelles with site-specific action capabilities.

6. Experimental section

Materials

Cu/Zn-superoxide dismutase (Cu/Zn-SOD) from bovine erythrocytes (>3,000 U/mg), lactoperoxidase (LPO) from bovine milk (>200 U/mg), catalase (CAT) from bovine liver (\geq 10,000 units/mg), xanthine oxidase (XO) (microbial, 7 U/mg), xanthine (XA), sodium phosphate buffer (DPBS 1 x Dulbecco's salts without calcium chloride and magnesium chloride, pH 7.3), hydrogen peroxide, 30% (w/w)) and dimethyl sulphoxide (DMSO) (>99.5%), were purchased from Sigma Aldrich and were used without any further treatment. 10-acetyl-3,7-dihydroxyphenoxazine (Amplex red), AlexaFluor 488 carboxylic acid succinimidyl ester, and AlexaFluor-633 carboxylic acid succinimidyl ester were obtained from Molecular Probes (Invitrogen) (Eugene, OR, USA) and were used as received. Dylight-488 carboxylic acid succinimidyl ester and dylight-633 carboxylic acid succinimidyl ester were purchased from Thermo Fisher Scientific Inc. (Rockford, IL, USA) and were used without further purification. Amplex red stock solutions were prepared in DMSO (50 mM) and stored at -20 °C. N-Octyl-oligo-oxyethylene (OPOE) was purchased from Enzo Life Sciences (Lausen, Switzerland). Hoechst and propidium iodide were purchased from Invitrogen. An ROS detection kit from EnzoLife, polycarbonate membrane filters (Millipore), and sepharose 2B (Sigma Aldrich) were used. RPMI-1640 cell culture medium (GIBCO), fetal calf serum (FCS), penicillin and streptomycin (Sigma Aldrich) and PBS (GIBCO) were used in the cell experiments. L- α -phosphatidylcholine, gramicidin from *bacillus brevis* (a mixture of gramicidin A, B, C and D), pyranine (8-Hydroxypyrene-1,3,6-trisulfonic acid trisodium salt), and acid phosphatase were purchased from Sigma-Aldrich and used without further purification. ELF97 phosphatase substrate was purchased from Invitrogen. 2-(6-chloro-1H-benzotriazole-1-yl)-1,1,3,3-tetramethylammonium

hexafluorophosphate (HCTU) and rink amide AM resin (0.61mmol/g) were purchased from IRIS Biotech GmbH, Marktredwitz, Germany. The amino acids (N- α -t.-Boc-L-histidine) were obtained from Novabiochem, L aufelfingen, Switzerland. Sulphorhodamine B acid chloride (λ_{ex} : 560 nm, λ_{em} : 580 nm) and copper(II)triflate was purchased from Sigma-Aldrich, Buchs, Switzerland. Dichloromethane was provided by Brenntag Schweizerhall AG, Basel, Switzerland, dimethylformamide (DMF) by J. T. Baker and acetonitrile (ACN) by Fischer Scientific. DMF was treated with aluminium oxide to reduce the concentration of free amines prior to application in peptide synthesis.

Methods used for the design of antioxidant nanoreactors/artificial peroxisomes

Outer membrane protein F production

OmpF expression was carried out in *E. coli* (BL21 (DE3)omp8)⁷² according to a previously optimised protocol⁵³ and the product was stored at 700 $\mu\text{g}/\text{mL}$ with 3 wt% OPOE stock solution at 4 C $^{\circ}$.

Fluorescence labelling of SOD, LPO and CAT

SOD was labelled with AlexaFluor-488 carboxylic acid succinimidyl ester, LPO was labelled with AlexaFluor-633 or dylight-633 carboxylic acid succinimidyl ester and CAT was labelled with dylight-488 carboxylic acid succinimidyl ester following the protocol provided by Invitrogen (www.invitrogen.com). The solutions containing labelled enzyme were filtered through a 0.22 μm Millex low protein-binding Durapore membrane (Millipore, Billerica, MA, USA) and separated by fast protein liquid chromatography (FPLC) on a Sephadex G25 (Aldrich) column equilibrated with phosphate-buffered saline buffer (PBS). The concentration of labelled enzyme and the degree of labelling was determined by dual wavelength FPLC ( akta FPLC, GE Healthcare

Europe GmbH, Glattbrugg, Switzerland) or by UV/VIS. After the labelling and purification procedure, 209.56 μM of labelled SOD, 4.45 μM of labelled LPO and 20 μM of labelled CAT were obtained.

PMOXA-PDMS-PMOXA vesicles preparation

Synthesis and characterisation of ABA triblock copolymer $\text{PMOXA}_n\text{-PDMS}_m\text{-PMOXA}_n$ ($n = 12$ and $m = 55$) has been described previously.⁵³ Vesicles were prepared at room temperature by drop-wise addition of PBS to ABA copolymer under continuous stirring, obtaining a 5 mg/mL polymer concentration. The aqueous polymer solution was extruded with an Avanti mini-extruder (Avanti Polar Lipids, Alabama, USA) through a 400 nm diameter pore-size polycarbonate (PC) membrane (one time), and through a 200 nm pore-size PC membrane (11 times) in order to reduce size polydispersity of the vesicles.

Preparation of nanovesicles containing individual enzyme types and SOD/LPO (or SOD/CAT) containing artificial peroxisomes

To encapsulate an individual enzyme type in vesicles, a solution of SOD, LPO or CAT (in concentrations between 0.1 – 0.83 mg/mL) were mixed with a solution of ABA block copolymer, followed by the preparation steps described above. A mixture of SOD and LPO at different ratios in PBS was added drop-wise to the ABA polymer solution to encapsulate both enzymes simultaneously. When required, channel protein⁶⁸ was simultaneously incorporated by drop-wise addition of the OmpF porin stock solution to the enzyme(s)-ABA copolymer mixture with continuous stirring to reach a final concentration of 50 $\mu\text{g/mL}$ OmpF. Non-encapsulated enzymes were separated from vesicles by 48 hour dialysis (Spectrapore dialysis tube, mean width cut-off size: 300 kDa, Spectrum Laboratories Inc.), exchanging dialysis PBS buffer after 24 hours.

Transmission electron microscopy (TEM)

Empty vesicles, vesicles containing a single-enzyme constituent, SOD-AlexaFluor-488, LPO-AlexaFluor-633 or CAT-dylight-488, vesicles containing co-encapsulated SOD-AlexaFluor-488 and LPO-AlexaFluor-633 and cell-samples were negatively stained with 2% uranyl acetate solution and deposited on carbon-coated copper grids. Vesicle samples were studied using a transmission electron microscope (Philips Morgagni 268D) at 293 K.

Light scattering (LS)

Dynamic (DLS) and static (SLS) light-scattering experiments were performed on an ALV (Langen, Germany) goniometer, equipped with an ALV He-Ne laser (JDS Uniphase, wavelength $\lambda = 632.8$ nm). Vesicles dispersions were prepared by serial dilution to polymer concentrations ranging from 2.5 to 0.05 g/L. Light scattering was measured in 10 mm cylindrical quartz cells at angles of $40 - 150^\circ$ at 293 ± 0.5 K. The refractive index increment $\partial n/\partial C$ of the vesicle dispersions was determined to 0.16 ± 0.02 mL/g at 632.8 nm with an ALV-DR1 differential refractometer. The photon intensity auto-correlation function $g^2(t)$ was determined with an ALV-5000E correlator (scattering angles between 40° and 150°). DLS data were analysed via non-linear decay-time analysis supported by regularized inverse Laplace transform of $g^2(t)$ (CONTIN algorithm). The angle-dependent apparent diffusion coefficient was extrapolated to zero momentum transfer (q^2) using ALV Correlator software static and dynamic FIT and PLOT 4.31. Angle and concentration-dependent SLS data were analysed using a Guinier plots approach.

Fluorescence correlation spectroscopy (FCS) and fluorescence cross-correlation spectroscopy (FCCS)

FCS and FCCS measurements were performed at room temperature on a Zeiss LSM 510-META/Confocor2 laser-scanning microscope equipped with an argon2-laser (488 nm), a helium/neon laser (633 nm) and a 40x water-immersion objective (Zeiss C/Apochromat 40X, NA 1.2) or a 63x water emulsion lens (Olympus). The pinhole was adjusted to 70 μm , and 90 μm , respectively. For each measurement, 10 μL of sample solution, containing either free dye AlexaFluor-488 or AlexaFluor-633 or dylight-488 or dylight-633, each concentrated to 50 nM, or containing an enzyme- (or combined enzyme-) encapsulated vesicle solution used directly after the purification step, were placed in special, chambered quartz glass holders (Lab-Tek; 8-well, NUNC A/S). For FCS, spectra were recorded over 30 s, and each measurement was repeated 10 times. Excitation power of the argon2 laser was $P_L = 15$ mW, and the excitation transmission at 488 nm was 5%. Excitation power of the helium/neon laser was $P_L = 5$ mW, and excitation transmission at 633 nm was 1%. Diffusion times for free dye (AlexaFluor-488, AlexaFluor-633, dylight-488 and dylight-633) as well as for labelled SOD, labelled LPO and labelled CAT were independently determined and fixed in the fitting procedure. The results were presented as a mean value of three independent measurements. For the fitting of the autocorrelation function according to a two-component model, the following equation 8 was used:

$$G(\tau) = 1 + \frac{1}{N} \left[(1 - Y) \left(\frac{1}{1 + \frac{\tau}{\tau_{D1}}} \right) \left(\frac{1}{1 + \frac{\tau}{S^2 \tau_{D1}}} \right)^{\frac{1}{2}} + Y \left(\frac{1}{1 + \frac{\tau}{\tau_{D2}}} \right) \left(\frac{1}{1 + \frac{\tau}{S^2 \tau_{D2}}} \right)^{\frac{1}{2}} + f(\tau) \right] \quad (8)$$

where,

- N : number of fluorescent particles
- S : structural parameter

- τ_{D1} : diffusion time of the component 1 in the assay.
- $1-Y$: fraction of particles with diffusion time τ_{D1}
- τ_{D2} : diffusion time of component 2 in the assay.
- Y : fraction of particles with diffusion time τ_{D2}
- $f(T)$: function used for fitting the tripled characteristics τ_T and % τ_T of the fluorescent label within the assay.

By means of an iterative least-square method, the values calculated by the algorithm are compared repeatedly to the experimentally generated autocorrelation curve and approximated until the difference between the two curves is minimised.

FCCS measurements were performed on the same instrument in the FCCS mode. Overlap of the confocal volumes was ensured in each channel by optimising pinhole settings in each measurement channel and performing calibration measurements. Cross-talk was measured independently in each detection channel to exclude false-positive cross-correlation.¹⁷¹ The fraction of co-encapsulated enzymes (R) can be estimated by the formula (equation 9):

$$R = \frac{R_g + R_r}{R_{cc}} \quad (9)$$

where R_g is the relative autocorrelation amplitude of the green channel, R_r : relative autocorrelation amplitude of the red channel, and R_{cc} : the relative amplitude of the cross-correlation.

The theoretical fraction of co-encapsulated enzymes, P , in the hypothesis of independent event probabilities p_1 (fraction of encapsulated

SOD) and p_2 (fraction of encapsulated LPO) can be estimated by the formula (equation 10):

$$P = p_1 p_2 \quad (10)$$

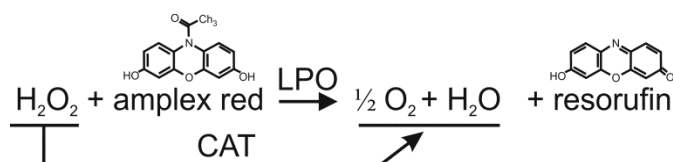
Individual enzyme types activity assay

LPO and CAT kinetics in solution or in nanovesicles were studied with a PerkinElmer LS55 fluorescence spectrometer (Waltham, Massachusetts, USA) at ambient temperature. Free LPO kinetics was tracked using a gradient of H_2O_2 and amplex red as follows: concentrations from $0.3 \mu\text{M}$ to $2.4 \mu\text{M}$ H_2O_2 , 5 nM LPO solution in PBS buffer and concentrations from $0.47 \mu\text{M}$ to $3.75 \mu\text{M}$ amplex red. The kinetics of LPO in nanovesicles were followed immediately after mixing H_2O_2 ($1.09 - 5.86 \mu\text{M}$) with a 50-fold diluted LPO-containing nanovesicle solution and the addition of amplex red ($0.18 - 1 \mu\text{M}$).

The solutions were mixed in a quartz cuvette and the fluorescence intensity of resorufin ($\lambda_{\text{ex}} = 530 \text{ nm}$, $\lambda_{\text{em}} = 580 \text{ nm}$), as the reaction product, was recorded.

CAT activity was compared to LPO activity by a competition reaction as presented in Scheme 1.

Scheme 1 CAT activity assay. Reprinted with permission from Ref. 78. Copyright 2013 American Chemical Society.



Multi-enzyme activity assay

The cascade reaction of SOD and LPO in tandem was followed in free solution or in nanovesicles by fluorescence spectroscopy using the set-up of FCS. Activity tests of free SOD and LPO in sequence were performed by mixing SOD (0.2 nM - 66 μ M) with LPO (0.016 - 1 μ M) in different concentration domains and in the presence of amplex red (9 μ M) with various amounts of xanthine (2 μ M – 25 μ M). The cascade reaction was started by the addition of xanthine oxidase (0.002 – 0.17 U/mL), with the concentrations adjusted to not short circuit SOD due to generation of H₂O₂ by the xanthine-xanthine oxidase system. Resorufin formation was followed as count rate (kHz).

Activity tests of SOD/LPO co-encapsulated vesicles were carried out by mixing 10 μ L SOD-LPO-containing nanovesicle solution with amplex red (23.8 μ M), and xanthine (35.71 μ M) to a final volume of 210 μ L. The cascade reaction was started by the addition of xanthine oxidase (0.24 U/mL).

Cell experiments

HeLa cells were cultured and maintained in Modified Eagle's Medium (DMEM) supplemented with high glucose, 10% fetal calf serum, 1% penicillin (10`000 units/mL) and streptomycin (10`000 mg/mL) (purchased from Sigma Aldrich), 2 mM L-glutamine and 1 mM pyruvate. Cells were grown in a humidified incubator (HERA Cell 150, Thermo Scientific, Germany) at 37 °C in a 5% CO₂ atmosphere until a confluence of 60 – 80% was achieved, and then harvested by trypsin-EDTA.

Cytotoxicity of the vesicles and APs

Cells were cultured in a 96-well plate at a density of 2 x 10⁴ cells/well, and incubated with 100 μ L of DMEM growth medium per well for 24 h. Different concentrations of empty polymer vesicles and enzyme-loaded

polymer vesicles were added to different wells and incubated with cells for a period of time (24 and 48 h). Subsequently, 20 μL of CellTiter® 96 Aqueous One Solution Cell Proliferation Assay (MTS) reagent (Promega) were added to each well and then incubated for a further 2 h. The absorbance of each well mixture was measured with a Spectromax M5e microplate reader (Molecular Devices) at 490 nm.

Cell uptake of APs

HeLa cells were cultured in a 6-well plate at different densities of cells per well (1×10^5 for CLSM, 2×10^5 for flow cytometry analysis, and 1×10^6 for TEM) in DMEM medium and incubated with enzyme-loaded polymer vesicle solution at different time intervals (2-, 4-, 8-, 18-, 24 h) at 37 °C in a humidified CO₂ incubator. For flow cytometry analysis, cells incubated with a solution of enzyme-loaded polymer vesicles were washed with PBS to remove free enzyme-containing vesicles and quantitatively analysed for rate of uptake of enzyme-containing vesicles with a flow cytometry set-up (CYAN, BD biosciences). A total of 10,000 events were analysed for each condition.

Study of APs escape from endosome

HeLa cells pre-incubated with a polymer vesicle solution containing co-encapsulated SOD and LPO were fixed with a solution of 3% paraformaldehyde in PBS, and 0.5% glutaraldehyde in PBS containing 1.5% saccharose (pH 7.3), and then post-fixed in 0.5% aqueous osmium tetroxide. The samples were then dehydrated using a graded series of ethanol solutions, block-stained in 6% of uranyl acetate and embedded in LR white resin (Sigma Aldrich). Ultra-thin sections were contrasted with 0.3% lead citrate and imaged with TEM.

For CLSM visualisation, the HeLa cell culture was first treated with enzyme-loaded polymer vesicles (100 $\mu\text{g}/\text{mL}$) for 4 h, followed by

treatment with pH-rodo™ Red dextran (20 µg/mL) for a further 20 min at 37 °C following the supplier's protocol. The cells were rapidly washed with PBS and prepared for imaging.

Cellular ROS detoxification by APs

HeLa cells were treated with paraquat to induce oxidative stress and analysed by flow cytometry (CYAN, BD Biosciences). HeLa cells at a density of 1×10^5 plated in a 6-well plate were first incubated with enzyme-loaded polymer vesicles (500 µg/mL) for 24 h, and subsequently with paraquat (2 mM) for a further 24 h at 37 °C in a 5% CO₂ atmosphere. Cells were washed with PBS buffer and stained with propidium iodide (PI, 50 mg/mL) to determine cell viability. A total of 10,000 events were analysed for each condition. To analyse the ROS detoxification kinetics of artificial peroxisomes in live cells, HeLa cells were seeded at 4×10^3 cells/well in a 96-well plate incubated overnight for cell attachment, followed by incubation with APs vesicles for 8 h. Afterwards, cells were treated with ROS/superoxide detection mix from EnzoLife's ROS/superoxide detection kit for 1 h. Cells were then incubated with pyocyanin (300 µM) to induce ROS generation in the cells. ROS detoxification kinetics was measured with a Spectromax M5e microplate reader (Molecular Devices) in the kinetic mode with a 550/620 nm filter set.

Methods used for the design of pH-triggered nanoreactors

PMOXA-PDMS and L- α -phosphatidylcholine vesicles preparation and encapsulation of the pH-sensitive dye (pyranine)

PMOXA₁₄-PDMS₆₅ was used to prepare vesicles at room temperature by using the film hydration method obtaining a 5 mg/mL polymer concentration. The direct dissolution method was used for the preparation

of vesicles based on L- α -phosphatidylcholine. In order to encapsulate the pH-sensitive dye pyranine, the polymer film or the lipids were hydrated using pyranine dissolved in PBS at a concentration of 50 mM. The aqueous polymer solution and liposome solution were extruded with an Avanti mini-extruder (Avanti Polar Lipids, Alabama, USA) through a 400 nm diameter pore-size polycarbonate (PC) membrane (one time), and through a 200 nm pore-size PC membrane (11 times) in order to reduce size polydispersity of the vesicles.

Measurements of gramicidin incorporation by monitoring pH change inside vesicles and design of pH-sensitive nanoreactors

Functional gramicidin ion-channel formation in the liposome or polymersome membrane was measured by using a PerkinElmer fluorescence spectrometer LS55 (Waltham, Massachusetts, USA) in the time driven mode. Pyranine encapsulated polymersomes were diluted 1:300. A pH change was monitored during addition of HCL to lower the pH from pH 8.3 to 5. The effect of subsequent addition of a low amounts of gramicidin (dissolved in different suitable solvents such as dimethyl sulphoxide (DMSO), trifluoroethanol (TFE), dioxane, pyridine, isoporpanol, decane and the mixtures DMSO:ethanol (DMSO:EtOH) in the ratio 1:1 and the mixture TFE:DMSO:EtOH (2:1:1)) to yield concentrations between 30 nM and 130 nM was compared in means of the change of the fluorescence intensity of pyranine inside the vesicles to the condition when the same amount of solvent was added and when no further components were added. In order to characterise pH-sensitive nanoreactors, simultaneously acid phosphatase (10 μ M) and ELF97 (12.5 μ M) were added during the vesicle formation process and purified as described above. pH-dependent activity of acid phosphatase inside the vesicles was measured using also the LS55 fluorescence spectrometer in the time driven mode.

Transmission electron microscopy (TEM)

Pyranine-encapsulated vesicles in condition of $\text{pH}_{\text{inside}} = \text{pH}_{\text{outside}}$, $\text{pH}_{\text{inside}} < \text{pH}_{\text{outside}}$ and after addition of gramicidin were negatively stained with 2% uranyl acetate solution and deposited on carbon-coated copper grids. Vesicle samples were studied using a transmission electron microscope (Philips Morgagni 268D) at 293 K.

Light scattering (LS)

Dynamic (DLS) experiments were performed on an ALV (Langen, Germany) goniometer, equipped with an ALV He-Ne laser (JDS Uniphase, wavelength $\lambda = 632.8$ nm). Light scattering was measured in 10 mm cylindrical quartz cells at a fixed angle of 90° at 293 ± 0.5 K for comparison of the effects of pH change and gramicidin incorporation in the polymersome membrane. The photon intensity auto-correlation function $g^2(t)$ was determined with an ALV-5000E correlator. DLS data were analysed via non-linear decay-time analysis supported by regularized inverse Laplace transform of $g^2(t)$ (CONTIN algorithm).

Methods used for study molecular interaction of metal-functionalised polymersomes with His-tags**Polymers**

Synthesis and characterisation of the diblock copolymer $\text{PB}_{39}\text{-}b\text{-PEO}_{36}$ was described previously.²¹ A mixture of $\text{PB}_{39}\text{-}b\text{-PEO}_{36}\text{-SA-OH}$ containing 10% $\text{PB}_{39}\text{-}b\text{-PEO}_{36}\text{-SA-trisNTA.d-Cu}^{2+}$ was used for all experiments. The diblock copolymer is functionalised with trisNTA a variant of NTA and complexed with Cu^{2+} ions. The non-functionalised diblock copolymer was characterised at a molecular mass of 3530 g/mol, which increased to 3690 g/mol upon functionalisation with trisNTA. Both block copolymers have a low polydispersity index.²¹

Peptide synthesis and fluorescent labelling

The peptides were synthesised on a Syro I Peptide Synthesiser (MultisynTech GmbH, Witten, Germany) using solid phase synthesis with an Fmoc-strategy. HCTU as the coupling reagent, with N-ethyl-diisopropylamine (DIPEA) dissolved in N-methyl-2-pyrrolidone (NMP) and used as the base to couple α -N-Fmoc-protected amino acids to the resin amide resin. For elongation, Fmoc-His-OH (0.5 mol/L, 4 equiv.), HCTU (0.5 mol/L, 4 equiv.) dissolved in DMF, and DIPEA (12 equiv.) were added to the resin. The mixture was agitated for 1 h and washed with DMF (3 x 3 mL). Fmoc deprotection was performed with 20% piperidine in DMF followed by 3 min agitation, draining, and repetition of deprotection for 10 min. Resin was subsequently washed with DMF (5x3 mL). Acetylation of unreacted amine groups was performed following each coupling with a solution of acetic anhydride/DIPEA (3 mol/L, 5 equiv.) in DMF. After synthesis, the peptide resin was alternately washed with DMF (3 x 6 mL), isopropanol (3 x 6 mL), and dichloromethane (3 x 6 mL), and then dried under vacuum.

The coupling of the dye to the N-terminus was performed on peptide still bound to the solid phase. A DMF solution of carboxylic-acid-succinimidyl-ester-activated dye (sulphorhodamine B) was added to the peptide. Uncoupled dye was washed away alternating with DMF (3 x 6 mL), isopropanol (3 x 6 mL), and dichloromethane (3 x 6 mL).

Cleavage of the peptide from the resin and removal of its protective groups was performed with a mixture of 95% trifluoroacetic acid (TFA), 2.5% tri-isopropylsilane, and 2.5% H₂O. The resin was additionally washed two times with this mixture (2 mL) and the peptide was precipitated in 40 mL cold di-isopropylether (IPE). The precipitated peptide was washed three times with cold IPE by centrifugation and decantation, before being dried under vacuum.

Peptide purification and characterisation

Purification and analysis of the peptides were performed by HPLC (Shimadzu Prominence 20A, Japan) on reverse phase (RP) columns (Merck Chromolith, RP-18e, 100 mm x 10 mm and 100 mm x 4.6 mm). The separation of the unlabelled peptide from labelled peptide yielded sample purities higher than 95%. This was detected by absorption at 280 nm and 560 nm. Linear gradients of solvent A (ACN) and solvent B (0.1% TFA, or 2% acetic acid in bidistilled water) were used.

The eluted sample was collected in fixed volume fractions, which were subsequently analysed for purity and molecular weight using HPLC and matrix-assisted laser desorption/ionisation time-of-flight mass spectroscopy (MALDI-TOF-MS). MALDI-TOF-MS was performed for mass confirmation with a Voyager-DETM System (Applied Biosystems, USA) in positive reflector mode, an accelerating voltage of 25 kV, grid voltage of 75% and 100 – 300 ns extraction delay time. Matrix (α -cyano-4-hydroxycinnamic acid) sample mixtures were prepared using a solution of ACN/0.1% TFA in bidistilled water on a 100-well gold plate. Fractions with matching mass and exceeding 95% purity were pooled with ammonia before neutralisation and then lyophilised. Products were stored under argon at -18 °C.

PB-*b*-PEO vesicle preparation and His₆-tag binding.

PB-*b*-PEO vesicles were prepared (800 μ M) according to the film rehydration method and contained 10% Cu^{II}-trisNTA functionalised PB-*b*-PEO copolymer.²¹ His₆-tags or sulphorhodamine B acid chloride labelled His₆-tags (s-His₆-tags) were added to the vesicle solution at different concentrations depending on the used measurement technique (see below). The solutions were extruded with an Avanti mini-extruder (Avanti Polar Lipids, Alabama, USA) through a 400 nm diameter pore-size

polycarbonate (PC) membrane (one time), and through a 200 nm pore-size PC membrane (11 times) in order to minimize nanovesicle size distribution.

Dynamic and Static Light Scattering (DLS and SLS)

Light scattering experiments were performed on an ALV (Langen, Germany) goniometer, equipped with an ALV He-Ne laser (JDS Uniphase, wavelength $\lambda = 632.8$ nm). Vesicle dispersions were prepared by serial dilution to polymer concentrations ranging from 0.7 to 0.1 g/L. Light scattering was measured in 10 mm cylindrical quartz cells at angles of $30 - 150^\circ$ at $293 \text{ K} \pm 0.5 \text{ K}$. The photon intensity auto-correlation function $g(t)$ was determined with an ALV-5000E correlator (scattering angles between 30° and 150°). DLS data were analysed via non-linear decay-time analysis supported by regularized inverse Laplace transform of $g(t)$ (CONTIN algorithm). The angle-dependent apparent diffusion coefficient was extrapolated to zero momentum transfer ($q \rightarrow 0$) using ALV Correlator software static and dynamic FIT and PLOT 4.31.

Transmission electron microscopy (TEM)

TEM images were taken using a transmission electron microscope (Philips Morgagni 268D) operated at 80 keV. The vesicle samples diluted to a final polymer concentration of $8 \mu\text{M}$ were negatively stained with 2% uranyl acetate solution for 10 s and deposited on carbon-coated copper grids in order to perform the measurement.

Confocal laser-scanning microscopy (CLSM)

PB-*b*-PEO vesicles were prepared ($800 \mu\text{M}$) as mentioned above and were incubated with fluorescently labelled His₆-tags (s-His₆-tags) ($1 \mu\text{M}$) for 5 min at room temperature. The solution was dialyzed for 24 h with a Spectrapore dialysis tube (mean width cut-off size: 300 kDa, Spectrum

Laboratories Inc.) to separate non-bound s-His₆-tags from vesicles. This solution was investigated at room temperature in special chambered quartz glass holders with a confocal laser-scanning microscope (Zeiss LSM 510-META/Confcor2), in LSM mode, using a Helium/Neon laser (543 nm) and a 63× water-immersion objective (Zeiss C/Apochromat 63X, NA 1.2). HeNe laser excitation power was PL = 1 mW, and excitation transmission at 543 nm was 20%.

Fluorescence Correlation Spectroscopy (FCS)

For FCS measurements, PB-*b*-PEO vesicle solutions with different Cu^{II}-functionalised PB-*b*-PEO concentrations (ranging from 2 μM to 8 μM) were prepared as mentioned above. The vesicle solutions containing different amounts of copper were incubated with 50 nM s-His₆-tags and were immediately measured without dialyzing. FCS measurements were performed at room temperature in special chambered quartz glass holders (Lab-Tek; 8-well, NUNC A/S), on the Zeiss LSM 510-META/Confcor2 laser-scanning microscope equipped with a HeNe laser (543 nm) and a 40× water-immersion objective (Zeiss C/Apochromat 40X, NA 1.2), with pinhole adjusted to 78 μm. Spectra were recorded over 30 s, and each measurement was repeated 10-times. The excitation power of the HeNe laser was PL =1 mW, and the excitation transmission at 543 nm was 10%. The structural parameter and diffusion times of the free dye (sulforhodamine B acid chloride) and of the dye-labelled His₆-tags were independently determined and fixed in the fitting procedure. These parameters were used to fit the autocorrelation curve of s-His₆-tags bound PB-*b*-PEO vesicles. The fluorescence signal was measured in real time and the autocorrelation function was calculated by a software correlator (LSM 510 META - ConfoCor 2 System). The results were presented as a mean value of three independent measurements.

X-band CW-EPR

Samples for X-band CW-EPR measurements were prepared similar to FCS with the exception that an 800 μM vesicle solution was incubated with 2.0 mM s-His₆-tags. X-band CW-EPR measurements (microwave (MW) frequency of about 9.44 GHz) were performed on a Bruker ESP 300E instrument, equipped with a liquid Helium cryostat (Oxford Inc.). A MW power of 10 mW, a modulation frequency of 100 kHz and a modulation amplitude of 0.5 mT were applied. All spectra were taken at 100 K and 10 K. The EasySpin program was utilized to simulate the CW-EPR spectra.¹⁷²

X-band pulsed EPR experiments were performed on a Bruker Eleksys spectrometer (9.76 GHz), equipped with a helium-gas flow cryostat (Oxford Inc.). The measurements were done at 4 K, with a repetition rate of 1 kHz.

ENDOR experiments

The ENDOR experiments were performed using the MW pulse sequence $\pi - T - \pi/2 - \tau - \pi - \tau - \text{echo}$, whereby a π radio-frequency (rf) pulse is applied during time T . The following parameters were used: $t_\pi = 48$ (96) ns, $t_{\pi/2} = 24$ (48) ns, $T = 15$ μs , $t_\tau = 13$ μs and $\tau = 200$ ns. The Mims ENDOR experiments were performed with the MW pulse sequence $\tau - \pi/2 - \tau - \pi/2 - T - \pi/2 - \tau - \text{echo}$. The parameters used were: $t_{\pi/2} = 16$ ns, $T = 15$ μs , $t_\tau = 13$ μs . The spectra were recorded at $\tau = 104$ ns.

HYSORE

The standard HYSORE experiments were performed using the $\pi/2 - \tau - \pi/2 - t_1 - \pi - t_2 - \pi/2 - \tau - \text{echo}$ sequence of pulses with $t_{\pi/2} = 16$ ns and $t_\tau = 16$ ns. The time intervals t_1 and t_2 were varied in steps of 16 ns. In order to eliminate unwanted echoes, a four-step phase cycle was applied. The time-domain HYSORE spectra were base-line corrected

with a third-order polynomial, apodized with a Hamming window and zero filled. The absolute-value spectra, obtained after two-dimensional Fourier transformation, were added to different τ values (104 ns, 120 ns, 176 ns) to reduce the blind-spot effects. The HYSORE spectra were simulated using a program developed at ETH Zurich.¹⁷³

DFT computations

Spin-restricted DFT computations were performed with the ORCA package¹⁷⁴⁻¹⁷⁷ on different models for aqueous Cu^{II}-NTA and Cu^{II}-NTA-His₆-tag binding (see results and discussion sections). Geometry optimisations were performed with the BP86 functional with an Ahlrich split-valence plus polarization (SVP) basis set for all other atoms except copper, for which a more polarized triple zeta valence basis set (TZVPP) is used. The geometry optimisations were tested for different starting geometries and the most stable geometry overall was chosen for further computation of the EPR parameters. For the latter, the B3LYP functional was taken, combined with the EPR-II basis set for nitrogen and hydrogen, the ORCA basis set “Core Properties” (CP(PPP)) and SVP for all other atoms. A dielectric surrounding with the dielectric constant of water was simulated assuming the COSMO model in all computations.

7. Appendix

Calculation of the encapsulation efficiency:

To determine maximum enzyme encapsulation efficiency based on the number of encapsulated enzymes per vesicle, following equations were used:

$$C = cN_A \quad (11)$$

$$\frac{1}{c} = V_{\text{apparent}} \quad (12)$$

$$\frac{V_{\text{vesicle}}}{V_{\text{apparent}}} = N_{\text{enzymes}}^* \quad (13)$$

$$\frac{N_{\text{exp}}^*}{N_{\text{enzymes}}^*} * 100 = EE_v (\%) \quad (14)$$

Where, in equation 11, c is the enzyme concentration [$gmol^{-1}$] used for encapsulation and N_A the Avogadro number. The reciprocal value of equation 11 gives the apparent volume per particle V_{apparent} (equation 12). The number of particles N_{enzymes}^* is derived by dividing the volume of the polymer vesicles V_{vesicle} by the volume of apparent volume V_{apparent} , representing the theoretical encapsulation of enzymes by one polymer vesicle (equation 13). To calculate the encapsulation efficiency, EE_v (%), the number of particles determined by FCS brightness measurements, N_{exp}^* , is divided by the theoretical value (equation 14).

Coordinates of the used models for DFT and spin density distributions:

Model A: $[\text{Cu}(\text{N}(\text{CH}_2\text{COO})_2(\text{CH}_2\text{COOH}))(\text{H}_2\text{O})_2]$

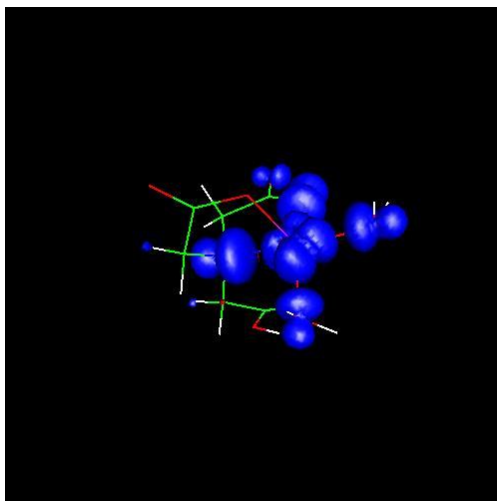


Fig. 54 Calculated spin density of model A. The contour levels are set at 0.0017 and -0.0017, respectively. Blue represents positive spin density, while red represents negative spin density.

Model A: Coordinates (in Å)

H	1.986319	-3.766505	-0.002538
H	1.048407	-5.276164	-0.082316
C	0.954631	-4.173606	0.006035
C	0.363875	-3.792742	1.372461
O	-0.360862	-2.715521	1.387576
H	1.911532	-3.810738	-2.437720
H	0.545170	-2.868100	-3.101400
H	-1.136889	-4.164111	-2.675405
H	-0.208779	-5.532695	-1.986454
N	0.206808	-3.604295	-1.148356
Cu	-0.780084	-1.904933	-0.339569
O	-1.742134	-1.379114	-2.071862
O	-1.564094	-0.255161	0.566701
C	-0.729385	-4.584561	-1.732349
C	1.130284	-3.063877	-2.179103
C	1.798449	-1.725157	-1.756243
O	2.872735	-1.424390	-2.313065
O	1.144457	-1.027523	-0.904697

C	-1.943043	-4.877461	-0.858495
H	-3.145692	-6.276150	-0.421447
O	-2.310240	-6.163282	-0.933767
O	-2.542502	-4.026354	-0.216120
O	0.638868	-4.455462	2.380576
H	-2.597000	-0.945433	-1.865298
H	-1.557722	-0.397582	1.537494
H	-1.227656	-0.678462	-2.526009
H	-0.959451	0.506383	0.438370

Model B: $[\text{Cu}(\text{N}(\text{CH}_2\text{COO})_2(\text{CH}_2\text{COOH}))(\text{C}_{11}\text{H}_{15}\text{N}_5\text{O})]$

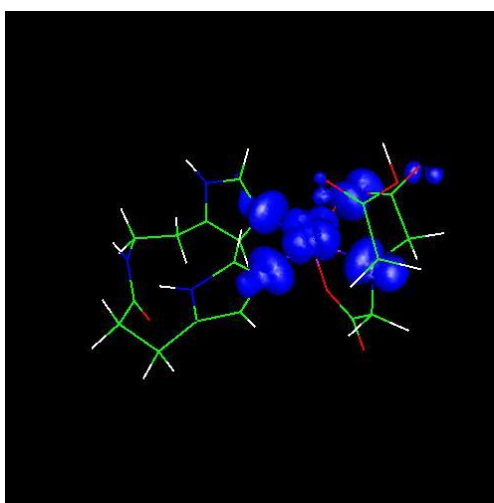


Fig. 55 Calculated spin density of model B. The contour levels are set at 0.0017 and -0.0017, respectively. Blue represents positive spin density, while red represents negative spin density.

Model B: Coordinates (in Å)

O	0.602432	-4.366001	2.366477
C	0.350746	-3.697671	1.351770
O	1.322347	-1.035162	-1.016393
C	1.913262	-1.808572	-1.848316
H	-4.370836	2.857339	-1.736942
H	-4.326905	2.165665	-3.798643
O	-0.303207	-2.579311	1.353159
H	-1.394634	1.904801	-4.778039
H	-2.787056	1.154668	-5.602032
C	-2.401450	1.473803	-4.610637
H	-0.173716	0.207722	-2.900534

H	-0.104274	1.294144	-0.635806
C	-0.986255	1.165798	-0.000845
C	-2.900475	-1.442676	-2.439612
Cu	-0.678248	-1.780782	-0.419280
N	-1.608280	-1.242648	-2.165215
N	-1.393501	-0.085058	0.424616
C	-1.199137	-0.172971	-2.944475
C	-2.264897	0.291787	-3.699694
N	-3.324982	-0.540675	-3.361746
H	-4.270859	-0.505503	-3.752520
H	-3.546140	-2.202240	-1.985470
C	-2.478165	0.098388	1.179757
N	-2.777760	1.424239	1.244256
C	-1.846837	2.132198	0.494726
H	-3.062747	-0.681864	1.679489
H	-3.558600	1.821479	1.774000
C	-3.328439	2.578944	-4.049666
C	-2.718276	3.329173	-2.860547
N	-3.476061	3.350105	-1.727732
C	-3.131937	4.107925	-0.528749
C	-1.882071	3.605736	0.240401
H	-4.022616	4.086288	0.128643
H	-2.954803	5.170926	-0.800015
H	-3.490140	3.335766	-4.846359
O	-1.618273	3.897314	-2.942389
H	-1.825320	4.179835	1.190601
H	-0.979793	3.857812	-0.348261
C	1.154341	-3.114166	-2.228934
N	0.202492	-3.572055	-1.184932
O	3.001551	-1.603611	-2.426269
H	0.575332	-2.895652	-3.149794
C	-0.782080	-4.516595	-1.745364
H	-1.160684	-4.103560	-2.703868
H	-0.316056	-5.500125	-1.970811
C	0.912737	-4.150743	-0.010429
H	1.886217	-3.913216	-2.477798
C	-2.013151	-4.720475	-0.869047
O	-2.579433	-3.831286	-0.248680
O	-2.442060	-5.990694	-0.915201
H	-3.283128	-6.049242	-0.403119
H	0.940642	-5.259686	-0.063526
H	1.967184	-3.806616	-0.030207

Model C: $[\text{Cu}(\text{N}(\text{CH}_2\text{COO})_3)(\text{C}_{11}\text{H}_{15}\text{N}_5\text{O})]^-$

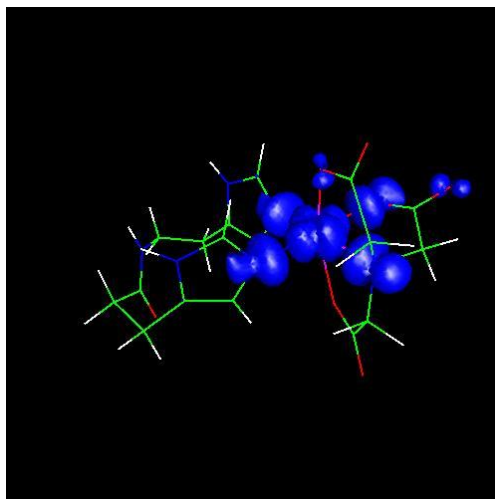


Fig. 56. Calculated spin density of model C. The contour levels are set at 0.0017 and -0.0017, respectively. Blue represents positive spin density, while red represents negative spin density.

Model C: Coordinates (in Å)

O	0.926091	-4.315926	2.321426
C	0.558879	-3.679574	1.316592
O	1.263008	-1.006906	-1.041422
C	1.838176	-1.749821	-1.904118
H	-4.327253	2.837797	-1.746011
H	-4.291118	2.170098	-3.818731
O	-0.125606	-2.583357	1.359648
H	-1.350400	1.875660	-4.758340
H	-2.737551	1.131332	-5.595999
C	-2.363172	1.454281	-4.601453
H	-0.202956	0.239622	-2.765101
H	-0.072479	1.178235	-0.422051
C	-1.014227	1.088705	0.129711
C	-2.912779	-1.466237	-2.445785
Cu	-0.802761	-1.886316	-0.363633
N	-1.643377	-1.235327	-2.106224
N	-1.492393	-0.146972	0.523713
C	-1.216786	-0.160207	-2.865571
C	-2.250859	0.278299	-3.679181
N	-3.310202	-0.575318	-3.392913
H	-4.236075	-0.557271	-3.829340

H	-3.551224	-2.241888	-2.009024
C	-2.641561	0.075919	1.161082
N	-2.914065	1.411203	1.184595
C	-1.894395	2.085042	0.524156
H	-3.298664	-0.682647	1.601380
H	-3.733103	1.834538	1.629047
C	-3.287239	2.573842	-4.063300
C	-2.682454	3.326981	-2.873982
N	-3.439690	3.343427	-1.740875
C	-3.090379	4.095822	-0.540404
C	-1.872386	3.556720	0.253649
H	-3.992548	4.110910	0.101781
H	-2.873153	5.149525	-0.817587
H	-3.431829	3.325748	-4.867958
O	-1.586170	3.902764	-2.954894
H	-1.812098	4.140558	1.198383
H	-0.950427	3.771309	-0.319655
C	1.117492	-3.082877	-2.274411
N	0.238591	-3.607442	-1.212457
O	2.897574	-1.501980	-2.529977
H	0.490583	-2.869658	-3.165252
C	-0.796413	-4.541126	-1.689452
H	-1.120777	-4.206244	-2.697008
H	-0.393004	-5.573851	-1.796641
C	1.010544	-4.159346	-0.076019
H	1.883745	-3.830852	-2.582332
C	-2.091358	-4.602167	-0.821057
O	-2.434265	-3.524442	-0.230012
O	-2.724058	-5.685285	-0.838941
H	1.015169	-5.271075	-0.095836
H	2.070530	-3.841981	-0.169094

8. References

- (1) Borisov, S. M.; Wolfbeis, O. S.: Optical Biosensors. *Chem. Rev.* (Washington, DC, U. S.) 2008, 108, 423-461.
- (2) Tanner, P.; Egli, S.; Balasubramanian, V.; Onaca, O.; Palivan, C. G.; Meier, W.: Can polymeric vesicles that confine enzymatic reactions act as simplified organelles? *FEBS Lett.* 2011, 585, 1699-1706.
- (3) Immordino, M. L.; Dosio, F.; Cattel, L.: Stealth liposomes: review of the basic science, rationale, and clinical applications, existing and potential. *Int. J. Nanomed.* 2006, 1, 297-315.
- (4) Baumann, P.; Tanner, P.; Onaca, O.; Palivan, C. G.: Bio-Decorated Polymer Membranes: A New Approach in Diagnostics and Therapeutics. *Polymers* 2011, 3, 173-192.
- (5) Fu, Z.; Ochsner, M. A.; de Hoog, H.-P. M.; Tomczak, N.; Nallani, M.: Multicompartmentalized polymersomes for selective encapsulation of biomacromolecules. *Chem. Commun.* 2011, 47, 2862-2864.
- (6) Palivan, C. G.; Vebert, C.; Axthelm, F.; Meier, W.: Responsive self-assembled nanostructures. *CRC Press LLC*, 2007, 32/1-32/26.
- (7) Dziubla, T. D.; Karim, A.; Muzykantov, V. R.: Polymer nanocarriers protecting active enzyme cargo against proteolysis. *J. Control. Release* 2005, 102, 427-439.
- (8) Wu, J.; Eisenberg, A.: Proton Diffusion across Membranes of Vesicles of Poly(styrene-*b*-acrylic Acid) Diblock Copolymers. *J. Am. Chem. Soc.* 2006, 128, 2880-2884.
- (9) de Hoog, H. M.; Nallani, M.; Cornelissen, J. J. L. M.; Rowan, A. E.; Nolte, R. J. M.; Arends, I. W. C. E.: Biocatalytic oxidation by chloroperoxidase from *Caldariomyces fumago* in polymersome nanoreactors. *Org. Biomol. Chem.* 2009, 7, 4604-4610.
- (10) Palivan, C. G.; Fischer-Onaca, O.; Delcea, M.; Ite, F.; Meier, W.: Protein-polymer nanoreactors for medical applications. *Chem. Soc. Rev.* 2011, 41, 2800-2823.
- (11) Tanner, P.; Baumann, P.; Enea, R.; Onaca, O.; Palivan, C.; Meier, W.: Polymeric Vesicles: From Drug Carriers to Nanoreactors and Artificial Organelles. *ACR* 2011, 44, 1039-1049.
- (12) Bolinger, P.-Y.; Stamou, D.; Vogel, H.: An Integrated Self-Assembled Nanofluidic System for Controlled Biological Chemistries. *Angew. Chem. Int. Edit.* 2008, 47, 5544-5549.

- (13) Graff, A.; Winterhalter, M.; Meier, W.: Nanoreactors from Polymer-Stabilized Liposomes. *Langmuir* 2001, 17, 919-923.
- (14) Karlsson, M.; Davidson, M.; Karlsson, R.; Karlsson, A.; Bergenholtz, J.; Konkoli, Z.; Jesorka, A.; Lobovkina, T.; Hurtig, J.; Voinova, M.; Orwar, O.: BIOMIMETIC NANOSCALE REACTORS AND NETWORKS. *Annu. Rev. Phys. Chem.* 2004, 55, 613-649.
- (15) Vriezema, D. M.; Aragones, M. C.; Elemans, J. A. A. W.; Cornelissen, J. J. L. M.; Rowan, A. E.; Nolte, R. J. M.: Self-Assembled Nanoreactors. *Chem. Rev. (Washington, DC, U. S.)* 2005, 105, 1445-1489.
- (16) Ma, Y.; Li, C.; Cai, T.; Li, J.; Hu, W.: Role of block junctions in the interplay of phase transitions of two-component polymeric systems. *J. Phys. Chem. B* 2011, 115, 8853-7.
- (17) Richard Di, G.; Joel, M., Reactive Oxygen Species and Oxidative Stress. In *The Toxicology of Fishes*, CRC Press: 2008, 273-324.
- (18) Hoogenboom, R.: Poly(2-oxazoline)s: A Polymer Class with Numerous Potential Applications. *Angew. Chem. Int. Edit.* 2009, 48, 7978-7994.
- (19) Batich, C.; DePalma, D.: Materials used in breast implants: silicones and polyurethanes. *J. Long-Term Eff. Med. Implants* 1992, 1, 255-68.
- (20) Satomi, T.; Nagasaki, Y.; Kobayashi, H.; Tateishi, T.; Kataoka, K.; Otsuka, H.: Physicochemical characterization of densely packed poly(ethylene glycol) layer for minimizing nonspecific protein adsorption. *J. Nanosci. Nanotechnol.* 2007, 7, 2394-2399.
- (21) Nehring, R.; Palivan, C. G.; Casse, O.; Tanner, P.; Tuxen, J.; Meier, W.: Amphiphilic Diblock Copolymers for Molecular Recognition: Metal-Nitrilotriacetic Acid Functionalized Vesicles. *Langmuir* 2008, 25, 1122-1130.
- (22) Kidane, A.; McPherson, T.; Shim, H. S.; Park, K.: Surface modification of polyethylene terephthalate using PEO-polybutadiene-PEO triblock copolymers. *Colloid Surface B* 2000, 18, 347-353.
- (23) Nehring, R.; Palivan, C. G.; Moreno-Flores, S.; Manton, A.; Tanner, P.; Toca-Herrera, J. L.; Thuenemann, A.; Meier, W.: Protein decorated membranes by specific molecular interactions. *Soft Matter* 2010, 6, 2815-2824.

- (24) Kita-Tokarczyk, K.; Grumelard, J.; Haefele, T.; Meier, W.: Block copolymer vesicles-using concepts from polymer chemistry to mimic biomembranes. *Polymer* 2005, 46, 3540-3563.
- (25) Balasubramanian, V.; Onaca, O.; Enea, R.; Hughes, D. W.; Palivan, C. G.: Protein delivery: From conventional drug delivery carriers to polymeric nanoreactors. *Expert Opin. Drug Del.* 2010, 7, 63-78.
- (26) Discher, D. E.; Eisenberg, A.: Polymer vesicles. *Science* 2002, 297, 967-73.
- (27) Caruso, F.: *Modification, Organization and Utilization of Colloid Particles: Colloids and Colloid Assemblies*; Wiley-VCH Verlag GmbH & Co. KGaA, 2004.
- (28) Smart, T.; Lomas, H.; Massignani, M.; Flores-Merino, M. V.; Perez, L. R.; Battaglia, G.: Block copolymer nanostructures. *Nano Today* 2008, 3, 38-46.
- (29) Förster, S.; Plantenberg, T., *From Self-Organizing Polymers to Nanohybrid and Biomaterials*. *Angew. Chem. Int. Edit.* 2002, 41 (5), 688-714.
- (30) Lazzari, M.; Liu, G.; Lecommandoux, S.; Editors: *Block Copolymers in Nanoscience*; Wiley-VCH Verlag GmbH & Co. KGaA, 2006.
- (31) Discher, B. M.; Won, Y.-Y.; Ege, D. S.; Lee, J. C. M.; Bates, F. S.; Discher, D. E.; Hammer, D. A.: Polymersomes: Tough vesicles made from diblock copolymers. *Science (Washington, D. C.)* 1999, 284, 1143-1146.
- (32) Korobko, A. V.; Backendorf, C.; van, d. M. J. R. C.: Plasmid DNA Encapsulation within Cationic Diblock Copolymer Vesicles for Gene Delivery. *J. Phys. Chem. B* 2006, 110, 14550-14556.
- (33) Schillen, K.; Bryskhe, K.; Mel'nikova, Y. S.: Vesicles Formed from a Poly(ethylene oxide)-Poly(propylene oxide)-Poly(ethylene oxide) Triblock Copolymer in Dilute Aqueous Solution. *Macromolecules* 1999, 32, 6885-6888.
- (34) Antonietti, M.; Foerster, S.: Vesicles and liposomes: A self-assembly principle beyond lipids. *Adv. Mater.* 2003, 15, 1323-1333.
- (35) Egli, S.; Schlaad, H.; Bruns, N.; Meier, W.: Functionalization of Block Copolymer Vesicle Surfaces. *Polymers* 2011, 3, 252-280.

- (36) Onaca, O.; Enea, R.; Hughes, D. W.; Meier, W.: Stimuli-Responsive Polymersomes as Nanocarriers for Drug and Gene Delivery. *Macromol. Biosci.* 2009, 9, 129-139.
- (37) Dimova, R.; Seifert, U.; Pouligny, B.; Forster, S.; Dobereiner, H. G.: Hyperviscous diblock copolymer vesicles. *Eur. Phys. J. E.* 2002, 7, 241-250.
- (38) Battaglia, G.; Ryan, A. J.: Bilayers and Interdigitation in Block Copolymer Vesicles. *J. Am. Chem. Soc.* 2005, 127, 8757-8764.
- (39) Evans, E.; Needham, D.: Physical properties of surfactant bilayer membranes: thermal transitions, elasticity, rigidity, cohesion and colloidal interactions. *J. Phys. Chem.* 1987, 91, 4219-28.
- (40) Malinova, V.; Belegriou, S.; Bruyn Ouboter, D. d.; Meier, W.: Biomimetic Block Copolymer Membranes. In *Polymer Membranes / Biomembranes*; Springer Berlin / Heidelberg, 2009; pp 113-166.
- (41) Nardin, C.; Hirt, T.; Leukel, J.; Meier, W.: Polymerized ABA Triblock Copolymer Vesicles. *Langmuir* 2000, 16, 1035-1041.
- (42) Burchard, W.: Static and dynamic light scattering from branched polymers and biopolymers. *Adv. Polym Sci.* 1983, 48, 1-124.
- (43) Pata, V.; Ahmed, F.; Discher, D. E.; Dan, N.: Membrane Solubilization by Detergent: Resistance Conferred by Thickness. *Langmuir* 2004, 20, 3888-3893.
- (44) Sauer, M.; Haefele, T.; Graff, A.; Nardin, C.; Meier, W.: Ion-carrier controlled precipitation of calcium phosphate in giant ABA triblock copolymer vesicles. *Chem. Commun.* 2001, 2452-2453.
- (45) Schermelleh, L.; Heintzmann, R.; Leonhardt, H.: A guide to super-resolution fluorescence microscopy. *J. Cell. Biol.* 2010, 190, 165-175.
- (46) Onaca, O.; Hughes, D. W.; Balasubramanian, V.; Grzelakowski, M.; Meier, W.; Palivan, C. G.: SOD Antioxidant Nanoreactors: Influence of Block Copolymer Composition on the Nanoreactor Efficiency. *Macromol. Biosci.* 2010, 10, 531-538.
- (47) van Dongen, S. F. M.; Verdurmen, W. P. R.; Peters, R. J. R. W.; Nolte, R. J. M.; Brock, R.; van Hest, J. C. M.: Cellular Integration of an Enzyme-Loaded Polymersome Nanoreactor. *Angew. Chem. Int. Edit.* 2010, 49, 7213-7216.
- (48) Zhang, X.; Tanner, P.; Graff, A.; Palivan, C. G.; Meier, W.: Mimicking the cell membrane with block copolymer membranes. *J. Polym. Sci. A1* 2012, 50, 2293-2318.

- (49) Sleytr, U. B.; Robards, A. W.: Freeze-fracturing: a review of methods and results. *J. Microsc-Oxford* 1977, 111, 77-100.
- (50) Ahmed, F.; Pakunlu, R. I.; Brannan, A.; Bates, F.; Minko, T.; Discher, D. E.: Biodegradable polymersomes loaded with both paclitaxel and doxorubicin permeate and shrink tumors, inducing apoptosis in proportion to accumulated drug. *J. Control. Release* 2006, 116, 150-158.
- (51) Axthelm, F.; Casse, O.; Koppenol Willem, H.; Nauser, T.; Meier, W.; Palivan Cornelia, G.: Antioxidant nanoreactor based on superoxide dismutase encapsulated in superoxide-permeable vesicles. *J. Phys. Chem. B* 2008, 112, 8211-7.
- (52) Egli, S.; Nussbaumer, M. G.; Balasubramanian, V.; Chami, M.; Bruns, N.; Palivan, C.; Meier, W.: Biocompatible Functionalization of Polymersome Surfaces: A New Approach to Surface Immobilization and Cell Targeting Using Polymersomes. *JACS* 2011, 133, 4476-4483.
- (53) Grzelakowski, M.; Onaca, O.; Rigler, P.; Kumar, M.; Meier, W.: Immobilized Protein-Polymer Nanoreactors. *Small* 2009, 5, 2545-2548.
- (54) Rigler, P.; Meier, W.: Encapsulation of fluorescent molecules by functionalized polymeric nanocontainers: investigation by confocal fluorescence imaging and fluorescence correlation spectroscopy. *J Am. Chem. Soc.* 2006, 128, 367-373.
- (55) Tanner, P.; Ezhevskaya, M.; Nehring, R.; Van Doorslaer, S.; Meier, W. P.; Palivan, C. G.: Specific His6-tag Attachment to Metal-Functionalized Polymersomes Relies on Molecular Recognition. *J. Phys. Chem. B* 2012.
- (56) Tanner, P.; Onaca, O.; Balasubramanian, V.; Meier, W.; Palivan, C. G.: Enzymatic Cascade Reactions inside Polymeric Nanocontainers: A Means to Combat Oxidative Stress. *Chem-Eur. J.* 2011, 4552-4560.
- (57) De Vocht, C.; Ranquin, A.; Van Ginderachter, J.; Vanhaecke, T.; Rogiers, V.; Van Gelder, P.; Versées, W.; Steyaert, J.: Polymeric nanoreactors for enzyme replacement therapy of MNGIE. *J. Control. Release* 2010, 148, e19-e20.
- (58) Broz, P.; Benito, S. M.; Saw, C.; Burger, P.; Heider, H.; Pfisterer, M.; Marsch, S.; Meier, W.; Hunziker, P.: Cell targeting by a generic receptor-targeted polymer nanocontainer platform. *J. Control. Release* 2005, 102, 475-488.

- (59) Torchilin, V. P.: Recent advances with liposomes as pharmaceutical carriers. *Nat. Rev. Drug Discov.* 2005, 4, 145-160.
- (60) Baumann, P.; Balasubramanian, V.; Onaca-Fischer, O.; Sienkiewicz, A.; Palivan, C. G.: Light-responsive polymer nanoreactors: a source of reactive oxygen species on demand. *Nanoscale* 2013, 5, 217-224.
- (61) Ben-Haim, N.; Broz, P.; Marsch, S.; Meier, W.; Hunziker, P.: Cell-Specific Integration of Artificial Organelles Based on Functionalized Polymer Vesicles. *Nano Lett.* 2008, 8, 1368-1373.
- (62) Balasubramanian, V.; Onaca, O.; Ezhevskaya, M.; Van Doorslaer, S.; Sivasankaran, B.; Palivan, C. G.: A surprising system: polymeric nanoreactors containing a mimic with dual-enzyme activity. *Soft Matter* 2011, 7, 5595-5603.
- (63) Dobrunz, D.; Toma, A. C.; Tanner, P.; Pfohl, T.; Palivan, C. G.: Polymer nanoreactors with dual functionality: simultaneous detoxification of peroxynitrite and oxygen transport. *Langmuir* 2012.
- (64) Geibel, B.; Merschky, M.; Rether, C.; Schmuck, C.: Artificial Enzyme Mimics. In *Supramolecular Chemistry*; John Wiley & Sons, Ltd, 2012.
- (65) Ahmed, F.; Discher, D. E.: Self-porating polymersomes of PEG-PLA and PEG-PCL: hydrolysis-triggered controlled release vesicles. *J. Control. Release* 2004, 96, 37-53.
- (66) Graff, A.; Sauer, M.; Van Gelder, P.; Meier, W.: Virus-assisted loading of polymer nanocontainer. *Proc. Natl. Acad. Sci. USA* 2002, 99, 5064-5068.
- (67) Kumar, M.; Grzelakowski, M.; Zilles, J.; Clark, M.; Meier, W.: Highly permeable polymeric membranes based on the incorporation of the functional water channel protein Aquaporin Z. *Proc. Natl. Acad. Sci. USA* 2007, 1-6.
- (68) Nardin, C.; Thoeni, S.; Widmer, J.; Winterhalter, M.; Meier, W.: Nanoreactors based on (polymerized) ABA-triblock copolymer vesicles. *Chem. Commun.* 2000, 1433-1434.
- (69) Graff, A.; Fraysse-Ailhas, C.; Palivan, C. G.; Grzelakowski, M.; Friedrich, T.; Vebert, C.; Gescheidt, G.; Meier, W.: Amphiphilic copolymer membranes promote NADH:ubiquinone oxidoreductase activity: Towards an electron-transfer nanodevice. *Macromol. Chem. Physic.* 2010, 211, 229-238.

- (70) Ranquin, A.; Versees, W.; Meier, W.; Steyaert, J.; Van Gelder, P.: Therapeutic Nanoreactors: Combining Chemistry and Biology in a Novel Triblock Copolymer Drug Delivery System. *Nano Lett.* 2005, 5, 2220-2224.
- (71) Nallani, M.; Benito, S.; Onaca, O.; Graff, A.; Lindemann, M.; Winterhalter, M.; Meier, W.; Schwaneberg, U.: A nanocompartment system (Synthosome) designed for biotechnological applications. *J. Biotechnol.* 2006, 123, 50-59.
- (72) Prilipov, A.; Phale, P. S.; Van Gelder, P.; Rosenbusch, J. P.; Koebnik, R.: Coupling site-directed mutagenesis with high-level expression: large scale production of mutant porins from *E. coli*. *FEMS Microbiol. Lett.* 1998, 163, 65-72.
- (73) Phale, P. S.; Philippsen, A.; Kiefhaber, T.; Koebnik, R.; Phale, V. P.; Schirmer, T.; Rosenbusch, J. P.: Stability of Trimeric OmpF Porin: The Contributions of the Latching Loop L2†. *Biochemistry* 1998, 37, 15663-15670.
- (74) Koebnik, R.; Locher, K. P.; Van Gelder, P.: Structure and function of bacterial outer membrane proteins: barrels in a nutshell. *Mol. Microbiol.* 2000, 37, 239-253.
- (75) Meier, W.; Nardin, C.; Winterhalter, M.: Reconstitution of channel proteins in (polymerized) ABA triblock copolymer membranes. *Angew. Chem. Int. Edit.* 2000, 39, 4599-4602.
- (76) Cowan, S. W.; Schirmer, T.; Rummel, G.; Steiert, M.; Ghosh, R.; Pauptit, R. A.; Jansonius, J. N.; Rosenbusch, J. P.: Crystal structures explain functional properties of two *E. coli* porins. *Nature (London)* 1992, 358, 727-33.
- (77) Wallace, B. A.: Gramicidin Channels and Pores. *Annu. Rev. Biophys. Bio.* 1990, 19, 127-157.
- (78) Tanner, P.; Balasubramanian, V.; Palivan, C. G.: Aiding Nature's Organelles: Artificial Peroxisomes Play Their Role. *Nano Lett.* 2013.
- (79) Ahmed, F.; Pakunlu, R. I.; Srinivas, G.; Brannan, A.; Bates, F.; Klein, M. L.; Minko, T.; Discher, D. E.: Shrinkage of a rapidly growing tumor by drug-loaded polymersomes: pH-triggered release through copolymer degradation. *Mol. Pharmaceut.* 2006, 3, 340-350.
- (80) Uchegbu, I. F.: Pharmaceutical nanotechnology: polymeric vesicles for drug and gene delivery. *Expert Opin. Drug Del.* 2006, 3, 629-640.

- (81) Lomas, H.; Canton, I.; MacNeil, S.; Du, J.; Armes, S. P.; Ryan, A. J.; Lewis, A. L.; Battaglia, G.: Biomimetic pH sensitive polymersomes for efficient DNA encapsulation and delivery. *Adv. Mater. (Weinheim, Ger.)* 2007, 19, 4238-4243.
- (82) Arifin, D. R.; Palmer, A. F.: Polymersome encapsulated hemoglobin: a novel type of oxygen carrier. *Biomacromolecules* 2005, 6, 2172-2181.
- (83) Wittemann, A.; Azzam, T.; Eisenberg, A.: Biocompatible Polymer Vesicles from Biamphiphilic Triblock Copolymers and Their Interaction with Bovine Serum Albumin. *Langmuir* 2007, 23, 2224-2230.
- (84) Christian, D. A.; Cai, S.; Bowen, D. M.; Kim, Y.; Pajerowski, J. D.; Discher, D. E.: Polymersome carriers: From self-assembly to siRNA and protein therapeutics. *Eur. J. Pharm. Biopharm.* 2009, 71, 463-474.
- (85) Lomas, H.; Du, J. Z.; Canton, I.; Madsen, J.; Warren, N.; Armes, S. P.; Lewis, A. L.; Battaglia, G.: Efficient Encapsulation of Plasmid DNA in pH-Sensitive PMPC-PDPA Polymersomes: Study of the Effect of PDPA Block Length on Copolymer-DNA Binding Affinity. *Macromol. Biosci.* 2010, 10, 513-530.
- (86) Cosentino-Gomes, D.; Rocco-Machado, N.; Meyer-Fernandes, J. R.: Cell signaling through protein kinase C oxidation and activation. *Int. J. Mol. Sci.* 2012, 13, 10697-10722.
- (87) Hileman, E. A.; Achanta, G.; Huang, P.: Superoxide dismutase: An emerging target for cancer therapeutics. *Expert Opin. Ther. Targets* 2001, 5, 697-710.
- (88) Sampayo, J. N.; Gill, M. S.; Lithgow, G. J.: Oxidative stress and aging - the use of superoxide dismutase/catalase mimetics to extend lifespan. *Biochem. Soc. Trans.* 2003, 31, 1305-1307.
- (89) Droege, W.: Oxidative stress in HIV infection. *Oxid. Stress, Dis. Cancer* 2006, 885-895.
- (90) Lomri, A.: Role of reactive oxygen species and superoxide dismutase in cartilage aging and pathology. *Future Rheumatol.* 2008, 3, 381-392.
- (91) Onaca-Fischer, O.; Liu, J.; Inglin, M.; Palivan, C. G.: Polymeric nanocarriers and nanoreactors: a survey of possible therapeutic applications. *Curr. Pharm. Des.* 2012, 18, 2622-2643.

- (92) Waris, G.; Ahsan, H.: Reactive oxygen species: Role in the development of cancer and various chronic conditions. *J. Carcinog.* 2006, 5, 14-14.
- (93) Grivennikova, V. G.; Vinogradov, A. D.: Generation of superoxide by the mitochondrial complex I. *Biochim. Biophys. Acta, Bioenerg.* 2006, 1757, 553-561.
- (94) Bonekamp, N. A.; Völkl, A.; Fahimi, H. D.; Schrader, M.: Reactive oxygen species and peroxisomes: Struggling for balance. *BioFactors* 2009, 35, 346-355.
- (95) Horiguchi, H.; Yurimoto, H.; Kato, N.; Sakai, Y.: Antioxidant System within Yeast Peroxisome: Biochemical and physiological characterisation of CbPmp20 in the methylotrophic yeast *Candida boidinii*. *J. Biol. Chem.* 2001, 276, 14279-14288.
- (96) Silva, J. P.; Coutinho, O. P.: Free radicals in the regulation of damage and cell death - basic mechanisms and prevention. *Drug Discoveries Ther.* 2010, 4, 144-167.
- (97) Heukamp, I.; Kilian, M.; Gregor, J. I.; Neumann, A.; Jacobi, C. A.; Guski, H.; Schimke, I.; Walz, M. K.; Wenger, F. A.: Effects of the antioxidative vitamins A, C and E on liver metastasis and intrametastatic lipid peroxidation in BOP-induced pancreatic cancer in syrian hamsters. *Pancreatology* 2005, 5, 403-409.
- (98) Jadot, G.; Vaille, A.; Maldonado, J.; Vanelle, P.: Clinical pharmacokinetics and delivery of bovine superoxide dismutase. *Clin. Pharmacokinet.* 1995, 28, 17-25.
- (99) Muzykantov, V. R.: Delivery of antioxidant enzyme proteins to the lung. *Antioxid. Redox Signaling* 2001, 3, 39-62.
- (100) Petelin, M.; Pavlica, Z.; Ivanuša, T.; Šentjurc, M.; Skalerič, U.: Local delivery of liposome-encapsulated superoxide dismutase and catalase suppress periodontal inflammation in beagles. *J. Clin. Periodontol.* 2000, 27, 918-925.
- (101) Kling, J.: PEGylation of Biologics. *BioProcess International* 2013, 11, 9.
- (102) Hochuli, E.; Döbeli, H.; Schacher, A.: New metal chelate adsorbent selective for proteins and peptides containing neighbouring histidine residues. *J. Chromatogr. A* 1987, 411, 177-184.
- (103) Terpe, K.: Overview of tag protein fusions: from molecular and biochemical fundamentals to commercial systems. *Appl. Microbiol. Biot.* 2003, 60, 523-533-533.

- (104) Dietrich, C.; Schmitt, L.; Tampe, R.: Molecular organization of histidine-tagged biomolecules at self-assembled lipid interfaces using a novel class of chelator lipids. *Proc. Natl. Acad. Sci.* 1995, 92, 9014-18.
- (105) Gamsjaeger, R.; Wimmer, B.; Kahr, H.; Tinazli, A.; Picuric, S.; Lata, S.; Tampe, R.; Maulet, Y.; Gruber, H. J.; Hinterdorfer, P.; Romanin, C.: Oriented Binding of the His6-Tagged Carboxyl-Tail of the L-type Ca²⁺ Channel alpha 1-Subunit to a New NTA-Functionalized Self-Assembled Monolayer. *Langmuir* 2004, 20, 5885-5890.
- (106) Hoffmann, C.; Gaietta, G.; Zurn, A.; Adams, S. R.; Terrillon, S.; Ellisman, M. H.; Tsien, R. Y.; Lohse, M. J.: Fluorescent labeling of tetracysteine-tagged proteins in intact cells. *Nat. Protocols* 2010, 5, 1666-1677.
- (107) Soh, N.: Selective Chemical Labeling of Proteins with Small Fluorescent Molecules Based on Metal-Chelation Methodology. *Sensors* 2008, 8, 1004-1024.
- (108) Wilchek, M.; Bayer, E. A.: Avidin-biotin immobilization systems. *Immobilized Biomolecules in Analysis* 1998, 15-34.
- (109) Buckland, R. M.: Strong signals from streptavidin-biotin. *Nature (London)* 1986, 320, 557-8.
- (110) Conroy, P. J.; Hearty, S.; Leonard, P.; O'Kennedy, R. J.: Antibody production, design and use for biosensor-based applications. *Developmental Biology* 2009, 20, 10-26.
- (111) Sine, S. M.: The nicotinic receptor ligand binding domain. *J. Neurobiol.* 2002, 53, 431-446.
- (112) Jamieson, A. C.; Wang, H.; Kim, S.-H.: A zinc finger directory for high-affinity DNA recognition. *Proc. Natl. Acad. Sci.* 1996, 93, 12834-12839.
- (113) Stadlbauer, S.; Riechers, A.; Späth, A.; König, B., Utilizing Reversible Copper(II) Peptide Coordination in a Sequence-Selective Luminescent Receptor. *Chem-Eur. J.* 2008, 14 (8), 2536-2541.
- (114) Kruppa, M.; König, B.: Reversible Coordinative Bonds in Molecular Recognition. *Chem. Rev.* 2006, 106, 3520-3560.
- (115) Knecht, S.; Ricklin, D.; Eberle, A. N.; Ernst, B.: Oligohis-tags: mechanisms of binding to Ni²⁺-NTA surfaces. *J. Mol. Recognit.* 2009, 22, 270-279.

- (116) Vomasta, D.; Högner, C.; Branda, N. R.; König, B.: Regulation of Human Carbonic Anhydrase I (hCAI) Activity by Using a Photochromic Inhibitor. *Angw. Chem. Int. Edit.* 2008, 47, 7644-7647.
- (117) Block, H.; Maertens, B.; Priestersbach, A.; Brinker, N.; Kubicek, J.; Fabis, R.; Labahn, J.; Schaefer, F., Immobilized-metal affinity chromatography (IMAC): a review. *Methods Enzymol.* 2009, 463, 439-473.
- (118) Huang, Z.; Hwang, P.; Watson, D. S.; Cao, L.; Szoka, F. C.: Tris-Nitrilotriacetic Acids of Subnanomolar Affinity Toward Hexahistidine Tagged Molecules. *Bioconjugate Chem.* 2009, 20, 1667-1672.
- (119) Lata, S.; Gavutis, M.; Tampé, R.; Piehler, J.: Specific and Stable Fluorescence Labeling of Histidine-Tagged Proteins for Dissecting Multi-Protein Complex Formation. *J. Am. Chem. Soc.* 2006, 128, 2365-2372.
- (120) 陳錦文; 劉宣良; 林進中; 何意: Molecular Dynamics Simulations of Metal Ion Binding to the His-tag Motif. *J. Chin. Chem. Soc-Taip.* 2005, 52, 1281-1290.
- (121) Rajesh; Bisht, V.; Takashima, W.; Kaneto, K., Development of a potentiometric urea biosensor based on copolymer poly(N-3-aminopropyl pyrrole-co-pyrrole) film. *React. Funct. Polym.* 2005, 62 (1), 51-59.
- (122) Chen, Q.; Schoenherr, H.; Vancso, G. J.: Block-copolymer vesicles as nanoreactors for enzymatic reactions. *Small* 2009, 5, 1436-1445.
- (123) Henderson, J. R.; Swalwell, H.; Boulton, S.; Manning, P.; McNeil, C. J.; Birch-Machin, M. A.: Direct, real-time monitoring of superoxide generation in isolated mitochondria. *Free Radical Res.* 2009, 43, 796-802.
- (124) Chen, D.; Xi, T.; Bai, J.: Biological effects induced by nanosilver particles: in vivo study. *Biomed. Mater.* 2007, 2, S126-8.
- (125) Slemmer, J. E.; Shacka, J. J.; Sweeney, M. I.; Weber, J. T.: Antioxidants and free radical scavengers for the treatment of stroke, traumatic brain injury and aging. *Curr. Med. Chem.* 2008, 15, 404-414.
- (126) Igarashi, R.; Hoshino, J.; Ochiai, A.; Morizawa, Y.; Mizushima, Y.: Lecithinized superoxide dismutase enhances its pharmacology

- potency by increasing its cell membrane affinity. *J. Pharmacol. Exp. Ther.* 1994, 271, 1672-7.
- (127) Gaspar, M. M.; Boerman, O. C.; Laverman, P.; Corvo, M. L.; Storm, G.; Cruz, M. E. M.: Enzymosomes with surface-exposed superoxide dismutase: In vivo behaviour and therapeutic activity in a model of adjuvant arthritis. *J. Control. Release* 2007, 117, 186-195.
- (128) Jubeh, T. T.; Antler, S.; Haupt, S.; Barenholz, Y.; Rubinstein, A.: Local Prevention of Oxidative Stress in the Intestinal Epithelium of the Rat by Adhesive Liposomes of Superoxide Dismutase and Tempamine. *Mol. Pharm.* 2005, 2, 2-11.
- (129) Lee, S.; Yang, S. C.; Heffernan, M. J.; Taylor, W. R.; Murthy, N.: Polyketal Microparticles: A New Delivery Vehicle for Superoxide Dismutase. *Bioconjugate Chem.* 2007, 18, 4-7.
- (130) Coyle, C. H.; Kader, K. N.: Mechanisms of H₂O₂-induced oxidative stress in endothelial cells exposed to physiologic shear stress. *ASAIO J.* 2007, 53, 17-22.
- (131) Michel, E.; Nauser, T.; Sutter, B.; Bounds, P. L.; Koppenol, W. H.: Kinetics properties of Cu,Zn-superoxide dismutase as a function of metal content. *Arch. Biochem. Biophys.* 2005, 439, 234-240.
- (132) Kussendrager, K. D.; Van Hooijdonk, A. C. M.: Lactoperoxidase: physico-chemical properties, occurrence, mechanism of action and applications. *Br. J. Nutr.* 2000, 84, S19-S25.
- (133) Nardin, C.; Winterhalter, M.; Meier, W.: Giant Free-Standing ABA Triblock Copolymer Membranes. *Langmuir* 2000, 16, 7708-7712.
- (134) Deisseroth, A.; Dounce, A. L.: Catalase: Physical and chemical properties, mechanism of catalysis, and physiological role. *Physiol Rev.* 1970, 50, 319-75.
- (135) Adrian, G.; Huang, L.: Entrapment of proteins in phosphatidylcholine vesicles. *Biochemistry* 1979, 18, 5610-4.
- (136) Cornish-Bowden, A.: *Fundamentals of Enzyme Kinetics*, Third Edition, 2004.
- (137) Zámocký, M.; Koller, F.: Understanding the structure and function of catalases: clues from molecular evolution and in vitro mutagenesis. *Prog. Biophys. Mol. Bio.* 1999, 72, 19-66.
- (138) Zhu, Z.; Momeu, C.; Zakhartsev, M.; Schwaneberg, U.: Making glucose oxidase fit for biofuel cell applications by directed protein evolution. *Biosens. Bioelectron.* 2006, 21, 2046-2051.

- (139) English, B. P.; Min, W.; van Oijen, A. M.; Lee, K. T.; Luo, G.; Sun, H.; Cherayil, B. J.; Kou, S. C.; Xie, X. S.: Ever-fluctuating single enzyme molecules: Michaelis-Menten equation revisited. *Nat. Chem. Biol.* 2006, 2, 87-94.
- (140) Kita-Tokarczyk, K.; Itel, F.; Grzelakowski, M.; Egli, S.; Rossbach, P.; Meier, W.: Monolayer Interactions between Lipids and Amphiphilic Block Copolymers. *Langmuir* 2009, 25, 9847-9856.
- (141) Lazarow, P. B.; Fujiki, Y.: Biogenesis of Peroxisomes. *Annu. Rev. Cell Biol.* 1985, 1, 489-530.
- (142) van Dongen, S. F. M.; Nallani, M.; Cornelissen, J. J. L. M.; Nolte, R. J. M.; van Hest, J. C. M.: A three-enzyme cascade reaction through positional assembly of enzymes in a polymersome nanoreactor. *Chem-Eur. J.* 2009, 15, 1107-1114.
- (143) Cho, E. C.; Zhang, Q.; Xia, Y.: The effect of sedimentation and diffusion on cellular uptake of gold nanoparticles. *Nat. Nano.* 2011, 6, 385-391.
- (144) Chithrani, B. D.; Ghazani, A. A.; Chan, W. C. W.: Determining the Size and Shape Dependence of Gold Nanoparticle Uptake into Mammalian Cells. *Nano Lett.* 2006, 6, 662-668.
- (145) Kim, J. A.; Åberg, C.; Salvati, A.; Dawson, K. A.: Role of cell cycle on the cellular uptake and dilution of nanoparticles in a cell population. *Nat. Nanotechnol.* 2012, 7, 62-68.
- (146) Nel, A. E.; Madler, L.; Velegol, D.; Xia, T.; Hoek, E. M. V.; Somasundaran, P.; Klaessig, F.; Castranova, V.; Thompson, M.: Understanding biophysicochemical interactions at the nano-bio interface. *Nat. Mater.* 2009, 8, 543-557.
- (147) Nam, H. Y.; Kwon, S. M.; Chung, H.; Lee, S.-Y.; Kwon, S.-H.; Jeon, H.; Kim, Y.; Park, J. H.; Kim, J.; Her, S.; Oh, Y.-K.; Kwon, I. C.; Kim, K.; Jeong, S. Y.: Cellular uptake mechanism and intracellular fate of hydrophobically modified glycol chitosan nanoparticles. *J. Control. Release* 2009, 135, 259-267.
- (148) Kim, H.; Lee, S. W.; Baek, K. M.; Park, J. S.; Min, J. H.: Continuous hypoxia attenuates paraquat-induced cytotoxicity in the human A549 lung carcinoma cell line. *Exp. Mol. Med.* 2011, 43, 494-500.
- (149) Jyothi, G.; Surolia, A.; Easwaran, K. R. K.: A23187 -- channel behavior: fluorescence study. *J. Biosci.* 1994, 19, 277-82.

- (150) Cukierman, S.; Quigley, E. P.; Crumrine, D. S.: Proton conduction in gramicidin A and in its dioxolane-linked dimer in different lipid bilayers. *Biophys. J.* 1997, 73, 2489-2502.
- (151) Killian, J. A.; Prasad, K. U.; Hains, D.; Urry, D. W.: The membrane as an environment of minimal interconversion. A circular dichroism study on the solvent dependence of the conformational behavior of gramicidin in diacylphosphatidylcholine model membranes. *Biochemistry* 1988, 27, 4848-4855.
- (152) He, H.; Uray, G.; Wolfbeis, O. S.: A thiamine-selective optical sensor based on molecular recognition. *Anal. Lett.* 1992, 25, 405-14.
- (153) Perinoto, A. C.; Maki, R. M.; Colhone, M. C.; Santos, F. R.; Migliaccio, V.; Daghasanli, K. R.; Stabeli, R. G.; Ciancaglini, P.; Paulovich, F. V.; de, O. M. C. F.: Biosensors for Efficient Diagnosis of Leishmaniasis: Innovations in Bioanalytics for a Neglected Disease. *Anal. Chem.* 2010, 82, 9763-9768.
- (154) Murphy, B.; Hathaway, B.: The stereochemistry of the copper(II) ion in the solid-state—some recent perspectives linking the Jahn–Teller effect, vibronic coupling, structure correlation analysis, structural pathways and comparative X-ray crystallography. *Coord. Chem. Rev.* 2003, 243, 237-262.
- (155) Stauch, O.; Schubert, R.; Savin, G.; Burchard, W.: Structure of artificial cytoskeleton containing liposomes in aqueous solution studied by static and dynamic light scattering. *Biomacromolecules* 2002, 3, 565-78.
- (156) Gruenwald, D.; Cardoso, M. C.; Leonhardt, H.; Buschmann, V.: Diffusion and binding properties investigated by Fluorescence Correlation Spectroscopy (FCS). *Curr. Pharm. Biotechnol.* 2005, 6, 381-386.
- (157) Dorn, I. T.; Neumaier, K. R.; Tampe, R.: Molecular Recognition of Histidine-Tagged Molecules by Metal-Chelating Lipids Monitored by Fluorescence Energy Transfer and Correlation Spectroscopy. *JACS* 1998, 120, 2753-2763.
- (158) Peisach, J.; Blumberg, W. E.: Structural implications derived from the analysis of electron paramagnetic resonance spectra of natural and artificial copper proteins. *Arch. Biochem. Biophys.* 1974, 165, 691-708.

- (159) Baute, D.; Arieli, D.; Neese, F.; Zimmermann, H.; Weckhuysen, B. M.; Goldfarb, D.: Carboxylate Binding in Copper Histidine Complexes in Solution and in Zeolite Y: X- and W-band Pulsed EPR/ENDOR Combined with DFT Calculations. *J. Am. Chem. Soc.* 2004, 126, 11733-11745.
- (160) Drew, S. C.; Noble, C. J.; Masters, C. L.; Hanson, G. R.; Barnham, K. J.: Pleomorphic Copper Coordination by Alzheimer's Disease Amyloid- β Peptide. *JACS* 2009, 131, 1195-1207.
- (161) Grommen, R.; Manikandan, P.; Gao, Y.; Shane, T.; Shane, J. J.; Schoonheydt, R. A.; Weckhuysen, B. M.; Goldfarb, D.: Geometry and Framework Interactions of Zeolite-Encapsulated Copper(II)-Histidine Complexes. *J. Am. Chem. Soc.* 2000, 122, 11488-11496.
- (162) Manikandan, P.; Epel, B.; Goldfarb, D.: Structure of Copper(II)-Histidine Based Complexes in Frozen Aqueous Solutions As Determined from High-Field Pulsed Electron Nuclear Double Resonance. *Inorg. Chem.* 2001, 40, 781-787.
- (163) Valko, M.; Morris, H.; Mazúr, M.; Telser, J.; McInnes, E. J. L.; Mabbs, F. E.: High-Affinity Binding Site for Copper(II) in Human and Dog Serum Albumins (an EPR Study). *J. Phys. Chem. B* 1999, 103, 5591-5597.
- (164) Schosseler, P. M.; Wehrli, B.; Schweiger, A.: Complexation of Copper(II) with Carbonate Ligands in Aqueous Solution: A CW and Pulse EPR Study. *Inorganic Chemistry* 1997, 36, 4490-4499.
- (165) Atherton, N. M.; Horsewill, A. J.: Proton ENDOR of $\text{Cu}(\text{H}_2\text{O})_6^{2+}$ in $\text{Mg}(\text{NH}_4)_2(\text{SO}_4)_4 \cdot 6\text{H}_2\text{O}$. *Mol. Phys.* 1979, 37, 1349-1361.
- (166) Hunt, M. J.; Mackay, A. L.; Edmonds, D. T.: Nuclear quadrupole resonance of ^{14}N in imidazole and related compounds. *Chem. Phys. Lett.* 1975, 34, 473-475.
- (167) Van Doorslaer, S.; Cereghetti, G. M.; Glockshuber, R.; Schweiger, A.: Unraveling the Cu^{2+} Binding Sites in the C-Terminal Domain of the Murine Prion Protein: A Pulse EPR and ENDOR Study†. *J. Phys. Chem. B* 2001, 105, 1631-1639.
- (168) van Gastel, M.; Coremans, J. W. A.; Jeuken, L. J. C.; Canters, G. W.; Groenen, E. J. J.: Electron Spin-Echo Envelope Modulation Spectrum of Azurin at X-Band. *J. Phys. Chem. A* 1998, 102, 4462-4470.

- (169) Burns, C. J.; Field, L. D.; Hambley, T. W.; Lin, T.; Ridley, D. D.; Turner, P.; Wilkinson, M., P.: X-Ray crystal structural determination of copper(II)-nitrilotriacetic acid-bis(N-methylimidazol-2-yl)ketone ternary complex. *ARKIVOC* 2001, vii, 157-165.
- (170) Neese, F.: Prediction of molecular properties and molecular spectroscopy with density functional theory : From fundamental theory to exchange-coupling. *Anglais* 2009, 253, 38.
- (171) Nguyen, T.; Swift, J.; Cramb, D.: Fluorescence Correlation Spectroscopy: The Measurement of Molecular Binding. In *Reviews in Fluorescence 2010*; Geddes, C. D., Ed.; Springer New York, 2012; Vol. 2010; pp 45-66.
- (172) Stoll, S.; Schweiger, A., EasySpin, a comprehensive software package for spectral simulation and analysis in EPR. *J. Mag. Res.* 2006, 178 (1), 42-55.
- (173) Madi, Z. L.; Van, D. S.; Schweiger, A., Numerical Simulation of One- and Two-Dimensional ESEEM Experiments. *J. Magn. Reson.* 2002, 154, 181-191.
- (174) Neese, F., Prediction of electron paramagnetic resonance g values using coupled perturbed Hartree-Fock and Kohn-Sham theory. *J. Chem. Phys.* 2001, 115, 11080-11096.
- (175) Neese, F., Theoretical Study of Ligand Superhyperfine Structure. Application to Cu(II) Complexes. *J. Phys. Chem. A* 2001, 105, 4290-4299.
- (176) Neese, F., Metal and ligand hyperfine couplings in transition metal complexes: the effect of spin-orbit coupling as studied by coupled perturbed Kohn-Sham theory. *J. Chem. Phys.* 2003, 118, 3939-3948.
- (177) Neese, F., Efficient and accurate approximations to the molecular spin-orbit coupling operator and their use in molecular g-tensor calculations. *J. Chem. Phys.* 2005, 122, 34107.

9. Acknowledgements

I cordially thank Prof. Dr. Cornelia Palivan for giving me all the important support and the necessary possibilities to intensively work this thesis out. I also thank Prof. Wolfgang Meier giving me the possibility to work on the projects in his group.

I thank Dr. Vimalkumar Balasubramanian for all his efforts during our collaboration in the group and beyond that. Especially, I appreciate his power in performing all the important cell experiments and giving me advice. I also owe Prof. Sabine Van Doorslaer and Dr. Maria Ezhevskaya a debt of gratitude for successful collaboration on EPR experiments. In addition, I thank Dr. Ozana Fischer, Patric Baumann, Dr. Karolina Langowska, and Adrian Nayer for fruitful discussion and suggestions during all the time of my research at the University of Basel.

Many thanks go to Gaby Persy and Vesna Olivieri for TEM measurements and to Dr. Mariusz Grzelakowski and Dalin Wu for providing polymers. I want to thank Dr. Dirk de Bruyn for helping me to synthesise the peptides.

Furthermore, I want to thank all the group members for a very friendly atmosphere in and outside the Lab. This work is based on the financial support provided by the Swiss National Science Foundation, and the National Centre of Competence in Nanoscale Science. This is gratefully acknowledged. The financial support for a Short Term Scientific Mission at the University of Antwerp is also honoured.

10. Abbreviations

• %	Percent
• °C	Degree celsius
• Å	Angstrom
• A ₂	Second virial coefficient
• AIDS	Acquired immunodeficiency syndrome
• ALS	Amyotrophic lateral sclerosis
• AP	Artificial peroxisome
• AqpZ	Aquaporin Z
• Ar	Argon
• ATP	Adenosine triphosphate
• BPA	Bis(2-pyridylmethyl)amine
• CAT	Catalase
• CLSM	Confocal laser-scanning microscopy
• Co	Cobalt
• cpm	Counts per molecule
• CR	Count rate
• Cu	Copper
• Cu/ZnSOD	Copper-zinc superoxide dismutase
• CW	Continuous wave
• D	Diffusion coefficient
• Da	Dalton
• DFT	Discrete Fourier transform
• DIEN	Diethylenetriamine
• DLS	Dynamic light scattering
• DMSO	Dimethyl sulphoxide
• DNA	Deoxyribonucleic acid
• EE _v	Encapsulation efficiency based on vesicles
• EGFP	Enhanced green fluorescent protein
• EMA	European medicines agency
• ENDOR	Electron nuclear double resonance
• EPR	Electron paramagnetic resonance
• EtOH	Ethanol
• FCS	Fluorescence correlation spectroscopy
• FCCS	Fluorescence cross correlation spectroscopy
• FDA	U.S food and drug administration
• Fe	Iron
• G	Autocorrelation amplitude

• GSH	Glutathione
• GSSG	Glutathione disulphide
• HCL	Hydrochloric acid
• He-Ne	Helium-Neon
• HPLC	High-performance liquid chromatography
• HRP	Horseradish peroxidase
• HYSCORE	Hyperfine sub-level correlation
• IDA	Iminodiacetato
• K ⁺	Potassium
• K	Binding constant
• k _b	Boltzmann constant
• kDa	kilo Dalton
• kHz	kilo Hertz
• K _M	Michaelis Menten constant
• LPO	Lactoperoxidase
• M	Weight-average molar mass
• MBP-FITC	Maltose binding protein- fluorescein isothiocyanate
• MHz	mega Hertz
• min	Minute
• ms	Millisecond
• mW	milli Watt
• Ni	Nickel
• nm	Nanometre
• NTA	Nitrilotriacetic acid
• OmpF	Outer membrane protein F
• OPOE	N-Octyl-oligo-oxyethylene
• OTf	Triflate
• P	Packing parameter
• PBS	Phosphate buffered saline
• PDI	Polydispersity
• PEG	Polyethylene glycol
• pH	Potential hydrogen
• PL	Laser power
• PB- <i>b</i> -PEO	Poly(butadiene)- <i>b</i> -poly(ethylene oxide)
• PMOXA-PDMS-PMOXA	poly-(2-methyloxazoline)-poly-(dimethylsiloxane)-poly-(2-methyloxazoline)
• PRX	Peroxiredoxin
• RFP	Red fluorescent protein
• R _g	Radius of gyration

• R_H	Hydrodynamic radius
• RNA	Ribonucleic acid
• RNS	Reactive nitrogen species
• ROS	Reactive oxygen species
• s	Second
• SA	Succinic anhydride
• SEM	Scanning electron microscopy
• SLS	Static light scattering
• SOD	Superoxide dismutase
• STED	Stimulated emission depletion
• STORM	Stochastic optical reconstruction microscopy
• T	Temperature
• TEM	Transmission electron microscopy
• TFE	Trifluoroethanol
• TPA	Tris(2-pyridylmethyl)amine
• TREN	Tri(2-aminoethyl)amine
• TRX	Thioredoxin
• V_{max}	Maximal reaction rate
• XA	Xanthine
• XO	Xanthine oxidase
• Zn	Zinc
• λ	Wavelength
• λ_{em}	Emission wavelength
• λ_{ex}	Excitation wavelength
• μg	micro gram
• μs	micro second
• τ_d	Diffusion time

11. Curriculum vitae

Name	Pascal Tanner
E-mail	pascal.tanner@unibas.ch
Telephone	+41 (0) 62 534 14 99
Date of birth	22.05.1984
Nationality	Switzerland
Civil status	married
Hometown	Werthenstein (LU)

Education

2009 – 2013	PhD in the group of Prof. Dr. C. Palivan Department of Physical-Chemistry, University of Basel Title: Design and development of protein-polymer assemblies to engineer artificial organelles
2008 – 2009	Master of Science in Nanosciences in the group of Prof. W. Meier, Department of Physical-Chemistry, University of Basel (grade 5.9) Title: Metal-functionalized polymer vesicles for molecular recognition
2004 – 2007	Bachelor of Science in Nanosciences University of Basel (grade 4.7)
1996 – 2003	Matura Kantonsschule Olten

Work experience

06/2009 – 2013	PhD project (Physical Chemistry Department of the University of Basel): - Development and characterisation of synthetic/biological nanosystems (nanoreactors and nanocontainers) - Writing scientific publications (articles, reviews and book chapter) - Presentation of results/products at international conferences and fairs
09/2008 – 04/2009	Master`s thesis (Physical Chemistry Department of the University of Basel):

- Development and characterisation of nanosystems for molecular recognition
- Short-term scientific foreign missions
- 01/2008 – 03/2008 **Project work** (Biocentre of the University of Basel):
 - Structural research of subunits in F_1F_0 ATP- synthase
 - Protein cloning and expression in *E. coli*.
- 03/2004 – 09/2007 **Project works** (Biocentre of the University of Basel and at PSI):
 - AFM study of damaged cartilage for early diagnosis
 - AFM study of effects on fracture and erosion of Si/SiO₂-Nanotowers
- 09/2003 – 02/2004 **Employee** (SBB in Olten) 100%:
 - logistics
 - inventory taking.

Language skills

English	fluent
German	first language
French	basic

Social competences

My very efficient way of working, reliability and my open communication skills allowed me to represent our group at international conferences and fairs.

Technical skills

- Development and characterisation of nanosystems (nanoreactors or nanocontainers) for antioxidant therapy or drug delivery:
 - Production/Engineering of biological/synthetic formulations
 - Microscopy and molecular imaging techniques (AFM, STM, optical microscopy, CLSM, TEM)
 - Spectroscopy techniques (UV/VIS, IR, EPR, NMR, FCS, FCCS, DLS, SLS)
 - Protein/enzyme labelling and characterisation
 - basic handling of cell cultures
 - Purification techniques (dialysis, size-exclusion and fast protein liquid chromatography)
- Presentation and writing skills:

- Presentation of results/concepts at international conferences and fairs
- Writing scientific publications
- Broadcasting of knowledge (introduction of practicum experiments/devices to students)

- EDV:

- Microsoft Word, Excel, PowerPoint, EndNote, Origin, Corel

Leisure time activities

- Successful participation at national and international MTB Cross-Country and Marathon events
- Team competitions: Stage race Craft Bike Transalp and 24h Race Davos

Oral presentations

- Nanoevent NextNanoStar, Basel, Switzerland, 21.03.2013
- 243rd ACS National Meeting, San Diego, CA, USA, 25.3.2012 - 29.3.2012
- Swiss Soft Days 3. WORKSHOP, Department of Chemistry, University of Fribourg, Switzerland, 20.10.2010

Poster presentations

- 1.) Swiss Soft Days 8. WORKSHOP, Geneva, Switzerland, 1.6.2012, **Title:** Specific His₆-tag attachment to metal-functionalized polymersomes relies on molecular recognition, **Pascal Tanner**, Maria Ezhevskaya, Rainer Nehring, Sabine Van Doorslaer, Wolfgang Meier, Cornelia Palivan.
- 2.) Hannover Messe, Hannover, Deutschland, 23.4.2012 - 27.4.2012, **Title:** Multifunctional nanoscale containers for enzymes: A simple tool to detect and defeat harmful radicals, **Pascal Tanner**, Cornelia G. Palivan, Wolfgang Meier.
- 3.) 243rd ACS National Meeting, San Diego, CA, USA, 25.3.2012-29.3.2012, **Title:** Enzyme cascade reactions inside polymer vesicles to fight oxidative stress, **Pascal Tanner**, Vimalkumar Balasubramanian, Ozana Onaca, Wolfgang Meier, Cornelia G. Palivan.
- 4.) NanoBioEurope, WORKSHOP, Cork, Ireland, 21.6.2011-23.6.2011, **Title:** How to fight oxidative stress with enzymes acting in tandem inside polymer vesicles? **Pascal Tanner**, Vimal Balasubramanian, Ozana Onaca, Cornelia G. Palivan.

- 5.) Swiss Soft Days 4. WORKSHOP, Nestlé Research Center, Lausanne, Switzerland, 3.2.2011, **Title:** Efficient antioxidant therapeutics: nanoreactors containing enzymes/ mimics at cellular level, **Pascal Tanner**, Ozana Onaca, Vimalkumar Balasubramanian, Cornelia G. Palivan.
- 6.) Fall Meeting of the Swiss Chemical Society 2010, ETH Zürich, Zürich, Switzerland, 16.9.2010, **Title:** Metal-NTA-functionalized vesicles for molecular recognition, **Pascal Tanner**, Rainer Nehring, Cornelia G. Palivan, Wolfgang Meier.
- 7.) Swiss Soft Days 2. WORKSHOP, Ecole Polytechnique de Lausanne, Lausanne, Switzerland, 23.6.2010, **Title:** How membrane proteins act as gates for POLYMERC nanocontainers, **Pascal Tanner**, Ozana Onaca, Patric Baumann, Cornelia G. Palivan.
- 8.) FUNctional Multiscale ARCHitectures Workshop, National Research Council, Bologna, Italy, 5.5.2010 - 7.5.2010, **Title:** Metal-NTA-functionalized vesicles for molecular recognition, **Pascal Tanner**, Rainer Nehring, Cornelia G. Palivan, Wolfgang Meier.
- 9.) Fall Meeting of the Swiss Chemical Society 2009, Ecole Polytechnique Fédérale de Lausanne, Switzerland, 4.9.2009, **Title:** Optimisation of Ni-NTA-functionalized vesicles for molecular recognition in solution, **Pascal Tanner**, Rainer Nehring, Cornelia G. Palivan, Wolfgang Meier.
- 10.) NCCR SNI Swiss Nano Basel, University of Basel, Switzerland, 11.6.2009, **Title:** Nickel-NTA-functionalized vesicles for molecular recognition, **Pascal Tanner**, Rainer Nehring, Cornelia G. Palivan, Wolfgang Meier.

Summer school

Summer School Essen, Germany, 22.09.2009-25.09.2009, Computational Chemistry and Spectroscopy

Awards

- STSM grant from COST P15 action
- SCNAT/SCS Swiss Travel Award

Publications

- 1.) Tanner, P.; Balasubramanian, V.; Palivan, C. G. Aiding Nature's Organelles: Artificial Peroxisomes Play Their Role. *Nano Letters*, **2013**, DOI: 10.1021/nl401215n
- 2.) Ite, F.; Dinu, A.; Tanner, P.; Fischer, O.; Palivan, G. C. Nanoreactors for biomedical applications, submitted.
- 3.) Heinisch, T.; Langowska, K.; Tanner, P.; Reymond, J.L. ; Palivan, C.; Meier, W.; Ward, T. Fluorescence-based assay for the optimization of artificial transfer hydrogenase activity within a biocompatible compartment *ChemCatChem.*, 2013, DOI: 10.1002/cctc.201200834
- 4.) Dobrunz, D.; Toma, A.; Tanner, P.; Pfohl, T.; Palivan C. Polymer nanoreactors with a dual-functionality: simultaneous detoxification of peroxynitrites and transport of oxygen *Langmuir*, 2012, DOI: 10.1021/la302724m
- 5.) Tanner, P.; Ezhevskaya, M.; Nehring, R.; Van Doorslaer, S.; Meier, W. P.; Palivan, C. G., Specific His₆-tag Attachment to Metal-Functionalized Polymersomes Relies on Molecular Recognition. *The Journal of Physical Chemistry B* **2012**, 116, 10113-24.
- 6.) Zhang, X.; Tanner, P.; Graff, A.; Palivan, C.; Meier, W., Mimicking the Cell Membrane with Block Copolymer Membranes. *Journal of Polymer Science, Part A: Polymer Chemistry* **2012**, 50, 2293-2318.
- 7.) Tanner, P.; Egli, S.; Balasubramanian, V.; Onaca, O.; Palivan, C. G.; Meier, W., Can Polymeric Vesicles that Confine Enzymatic Reactions act as Simplified Organelles? *FEBS Letters* **2011**, 585, 1699-1706.
- 8.) Tanner, P.; Onaca, O.; Balasubramanian, V.; Meier, W.; Palivan, C. G.: Enzymatic Cascade Reactions inside Polymeric Nanocontainers: A Means to Combat Oxidative Stress. *Chemistry – A European Journal* **2011**, 17, 4552-4560.
- 9.) Tanner, P.; Baumann, P.; Enea, R.; Onaca, O.; Palivan, C. G.; Meier, W.: Polymeric Vesicles: from Drug Carriers to Nanoreactors and Artificial Organelles *Accounts of Chemical Research* **2011**, 44, 1039-1049.
- 10.) Baumann, P.; Tanner, P.; Onaca, O.; Palivan, C.G. Bio-Decorated Polymer Membranes: A New Approach in Diagnostics and Therapeutics. *Polymers* **2011**, 3, 173-192.
- 11.) Nehring, R.; Palivan, C. G.; Moreno-Flores, S.; Manton, A.; Tanner, P.; Toca-Herrera, J. L.; Thuenemann, A.; Meier, W.: Protein Decorated Membranes by Specific Molecular Interactions. *Soft Matter* **2010**, 6, 2815-2824.
- 12.) Nehring, R.; Palivan, C. G.; Casse, O.; Tanner, P.; Tuxen, J.; Meier, W.: Amphiphilic Diblock Copolymers for Molecular Recognition: Metal-Nitrilotriacetic Acid Functionalized Vesicles. *Langmuir* **2008**, 25, 1122-1130.

References

1. Prof. Dr. Cornelia G. Palivan
Department of Chemistry, University of Basel, Switzerland
Email: cornelia.palivan@unibas.ch
Phone: 061 267 38 39
2. Prof. Dr. Wolfgang Meier
Department of Chemistry, University of Basel, Switzerland
Email: wolfgang.meier@unibas.ch
Phone: 061 267 38 02